RICE UNIVERSITY

Understanding the Nature of Blazars High Energy Emission with Time Dependent Multi-zone Modeling

by

Xuhui Chen

A THESIS SUBMITTED
IN PARTIAL FULFILLMENT OF THE
REQUIREMENTS FOR THE DEGREE

Doctor of Philosophy

APPROVED, THESIS COMMITTEE:

Giovanni Fossati, Chair
Assistant Professor of Physics and Astronomy

Edison Liang
Andrew Hayes Buchanan Professor of Physics and Astronomy

Robert M. Raphael
Associate Professor of Bioengineering

HOUSTON, TEXAS
May, 2012

ABSTRACT

Understanding the Nature of Blazars High Energy Emission with Time Dependent Multi-zone Modeling

by

Xuhui Chen

In this thesis we present a time-dependent multi-zone radiative transfer code and its applications to study the multiwavelength emission of blazars. The multiwavelength variability of blazars is widely believed to be a direct manifestation of the formation and propagation of relativistic jets, and hence the related physics of the black hole - accretion disk - jet system. However, the understanding of these variability demands highly sophisticated theoretical analysis and numerical simulations. Especially, the inclusion of the light travel time effects(LTTEs) in these calculations has long been realized important, but very difficult. The code we use couples Fokker-Planck and Monte Carlo methods, in a 2 dimensional (cylindrical) geometry. For the first time all the LTTEs are fully considered, along with a proper, full, self-consistent treatment of Compton cooling, which depends on the LTTEs.

Using this code, we studied a set of physical processes that are relevant to the variability of blazars, including electron injection and escape, radiative cooling, and stochastic particle acceleration. Our comparison of the observational data and the simulation results revealed that a combination of all those processes is needed to reproduce the observed behaviors of the emission of blue blazars. The simulation favors that the high energy emission at quiet and flare stages comes from the same

location.

We have further modeled red blazars PKS 1510-089. External radiation, which comes from the broad line region (BLR) or infrared torus, is included in the model. The results confirm that external Compton model can adequately describe the emission from red blazars. The emission from BLR is favored as the source of Inverse Compton seed photons, compared to synchrotron and IR torus radiation.

Acknowledgments

This work is made possible by the help and support from many people. I would like to express my gratefulness to all of them. First of all I would like to thank my advisor Dr. Giovanni Fossati. Many of the ideas in this work came from the several-hours-long discussions we frequently had. He has been supportive not only to my research project, but also to my approach to science and career in general. I also want to thank Dr. Edison Liang, who gave me many advices since the very beginning of my life at Rice. Another person that is really essential in the completion of this work is Dr. Markus Böttcher at Ohio University. I am very grateful for his guidance on my work and the warm hospitality he provided during my visit to Ohio University. I also benefited from Dr. Matthew Baring a lot by taking many of the excellent courses he taught and talking with him about my work. Additionally, I would like to acknowledge the helpful discussions I had with fellow graduate student Guy Hilburn about the Monte Carlo code.

I would like to take this chance to express my deepest thanks to my mother Yongli Wang and father Huaming Chen. Their unconditional love and support have been the source of my courage to overcome all the obstacles I have met these years. In addition, I want to give appreciation to all the friends I have met at Rice. They made my PhD life at Rice one of my greatest memories. These friendships will be treasured and maintained for a lifetime.

Contents

Illustrations

Tables

Chapter 1

Introduction

The formation and evolution of relativistic jets in Active Galactic Nuclei (AGN) remains one of the unsolved fundamental problems in astrophysics. Understanding these jets and their connection to the black holes (BHs) would advance our view of the universe. The highly variable nature of blazars is a primary way to probe the relativistic jets and black hole physics, because it gives us information about how the physical conditions in these extreme environments evolve violently. In the introduction I will cover the background of AGN and blazars, and discuss several physical processes that are essential in understanding the multiwavelength variability of blazars.

1.1 AGN paradigm

Most galaxies harbor supermassive blackholes (SMBH) in their centers (Urry & Padovani, 1995; Antonucci, 1993). When these SMBH accrete large amounts of mass towards them, this mass releases large amount of gravitational energy and becomes involved in high energy processes. In these circumstances, the centers of these galaxies become the so called Active Galactic Nucleus (AGN). AGN are extremely luminous, but are confined in a relatively compact region. Beside the central BH, the standard picture of AGN include an accretion disc, broad line regions (BLR), narrow line regions (NLR), an infrared torus, and a pair of jets in some cases (see Fig. 1.1).

The obscuration from the torus and the relativistic effects from the jets casue the anisotropy of the emission of AGN. They appear very differently when our lines of sight are oriented in different directions with respect to the AGN.

Observationally AGN include quasars, radio galaxies, Seyfert galaxies, and BL Lac objects. BL Lac objects and Flat Spectrum Radio Quasars (FSRQ) are collectively known as blazars, which is the main type of objects to be studied in this thesis. Blazars represent the AGN that have their bipolar relativistic jets pointing towards us, while radio galaxies represent the other extreme – we are looking at the system with the accretion discs edge on.

The gravitational potential of the SMBH is the source of energy in AGN. The mass attracted by the SMBH falls towards it with angular momentum. These angular momentum forces the mass to rotate around the black hole, forming the accretion disc, where it gradually loses angular momentum. The process through which it loses angular momentum is not entirely clear. The maxium effective temperature of radiation of the disc can reach up to $10^8 K$, making the disc bright from optical through X-ray (Shakura & Sunyaev, 1973). Further away there is cooler but still warm dust surrounding the black hole and accretion disc (Krolik & Begelman, 1988). This dusty torus is optical thick, and absorbs much of the radiation from the central region in some directions. The obscuration from this torus results in some of the anisotropy in our observation of AGN (Urry & Padovani, 1995). There are also clouds of gas surrounding the black holes. The region close to the black hole are called broad-line region (BLR). The clouds move with typical velocities in the range of $10^{3-4} kms^{-1}$. Their emission lines are observed to be broadened because of the bulk motion of the emitting gas. However, because of the small size of the broad line regions, it is unlikely that we will be able to spatially resolve them at optical wavelength in the near future

(Blandford & McKee, 1982; Blumenthal & Mathews, 1975). At larger distance, the clouds move less fast and the region is called narrow-line region (NLR). Because the NLR are much more extended than the BLR, their sizes can be determined through the use of spatially resolved spectroscopy (e.g. Robinson et al., 1994; Bennert et al., 2006).

At even larger scales, spatially extended double-sided jets are clearly seen in radio galaxies. In the case of blazars, becasue the jets are pointing towards us, these radio jets are not that extended. But high resolution radio images still reveal the existence of radio jets (e.g. Savolainen et al., 2010). However, not all AGN have radio jets. Based on this difference AGNs are classified into two types: radio louds and radio quiets The origin of these jets is still a mystery. It is possible that they are powered by the accretion disc as hydromagnetic flows (Blandford & Payne, 1982), or directly by rotating black holes through a purely electromagnetic mechanism (Blandford & Znajek, 1977). The result is a pair of relativistic jets which produce strong radio emission. Some of these jets (e.g. those in Fanaroff Riley Class I, FRI radio galaxies) decelerate and dissipate as they travel, while others (e.g. those in Fanaroff Riley Class II, FRII radio galaxies) transport most of their content to hundreds of kpc without decelerating or dissipating much (Fanaroff & Riley, 1974).

1.2 What are blazars?

Observationally, blazars are persistent extragalactic sources that share some common features, which include:

- Fast and large flux variability.
- Strong and variable polarization measured in radio and optical bands.

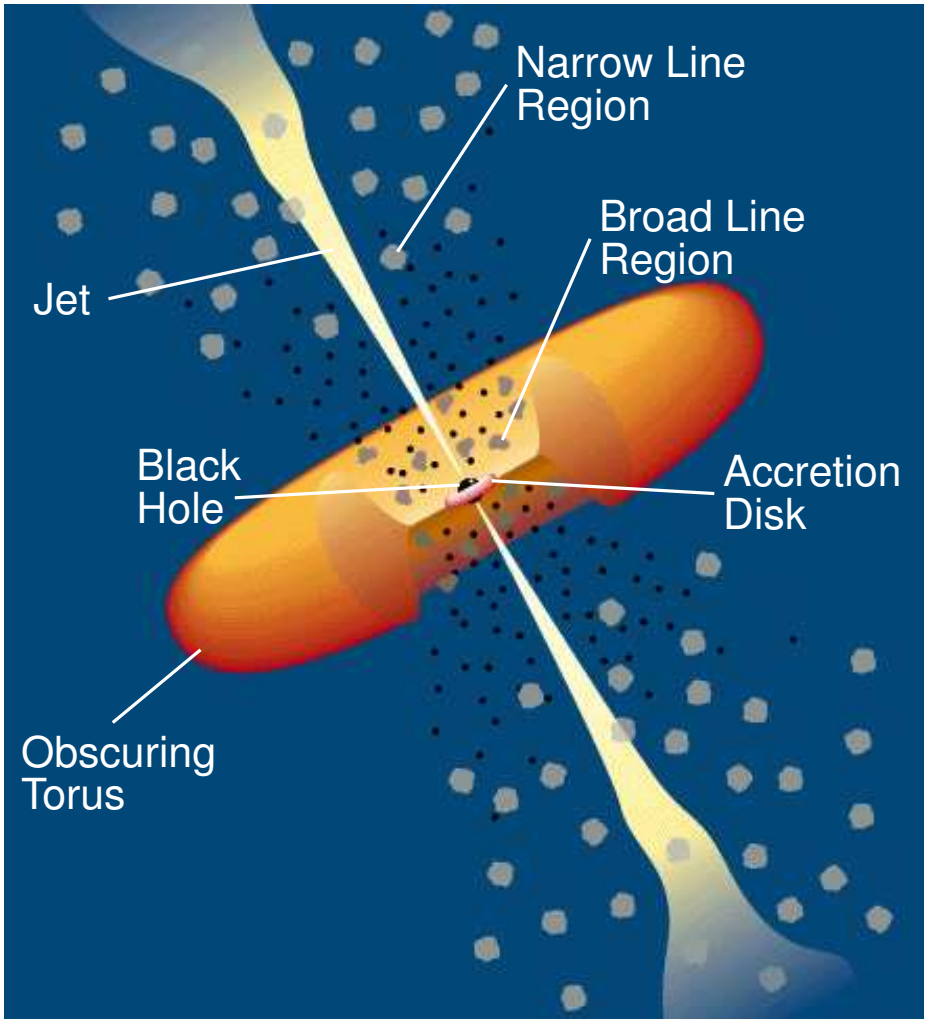

Figure 1.1 : A schematic diagram of current paradigm of radio loud AGN (Urry & Padovani, 1995).

- Non-thermal spectrum extending from radio to γ-ray bands.

The spectral energy distribution (SED) of blazars consist of two non-thermal components. One extends from radio to IR-X-ray frequency, the other continues from X-ray all the way to γ-ray frequencies (see Fig. 1.2). The first component comes from synchrotron radiation, as confirmed by the observed polarization; the second component is frequently explained as inverse Compton radiation from the same synchrotron emitting electrons. But the exact origin of this radiation is still under debate (see §1.5).

Traditionally blazars are seperated into BL Lac objects and FSRQs based on the distinction in their optical spectra. BL Lacs usually show featureless non-thermal spectrum, while FSRQs have luminous broad emission lines component observable on top of the flat spectrum. BL Lacs can be further divided into high-energy peaked BL Lacs (HBL) and low-energy peaked BL Lacs (LBL), based on the peaks of their spectral energy distributions (SED). HBL and LBL emit most their synchrotron power at UV/X-ray and radio/infrared frequencies respectively (Giommi & Padovani, 1994; Padovani & Giommi, 1995). If we blend FSRQ into this classification based on SEDs, FSRQs and LBL have similar continua and can be put into the same category and called red blazars, while HBL form the other category of blue blazars. As shown in Fig. 1.2, for red blazars, the luminosity of the second component in the SED is larger than the one of the synchrotron component, sometimes by more than one order of magnitude; but for blue blazars, the two bumps in the SED have similar luminosities. Fossati et al. (1998) pointed out that red blazars are more luminous powerful blazars, while blue blazars are less luminous sources, showing a correlation between SED and

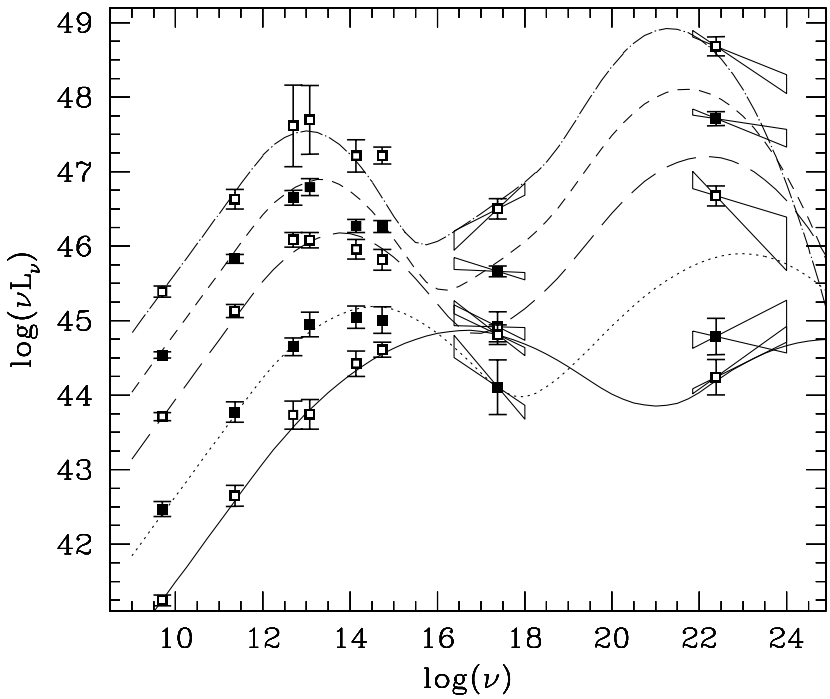

Figure 1.2 : Average SEDs of blazars binned according to radio luminosity (Fossati et al., 1998). The SED of blazars with high radio luminosity generally peak at lower frequency. Also, the second components of these powerful blazars are more dominant than their low luminosity counterparts.

luminosity* that has been refered to as the 'blazar sequence'. This distinction in luminosity, as well those in spectra and mophologies, also hints that red blazars and FR II radio galaxies belong to the same population, while blue blazars and FR I radio galaxies have the same kind of decelerating jets (Meyer et al., 2011. See more discussion about FR I/FR II and BL Lac/FSRQ unification in Urry & Padovani, 1995) .

From the theoretical point of view, what we observe and call blazars are the relativistic jets of AGN. Blazars are those jets that come towards us. Because of relativistic beaming, the flux we observe is greatly amplified. The spectrum is blue-shifted, and the variability time scale is shortened (see more details in §1.4).

1.3 Variability of blazars

Blazars are variable at almost all wavelength, over very broad range of time scales. Fast variability with a doubling time of a few minutes at TeV γ-ray has been seen (Aharonian et al., 2007). But variability on time scale of years is also observed (Fig. 1.3). The amplitude of variation is dependent on both the wavelength and the object that are under study, with a general trend of larger amplitude and shorter timescales at the high frequency end of the two SED components. It can be as small as a few percent in radio, up to more than a factor of ten in X-ray or γ-ray (Ulrich et al., 1997).

Several blazars are bright enough that we can study their variability on short timescales, minutes in case of the strongest flares, even in γ-ray, where the number

*The luminosity referred to here is calculated based on the assumption that the emission from the source is isotropic. However, in most cases this assumption is unlikely to be true for AGNs, especially for blazar jets. See §1.4.

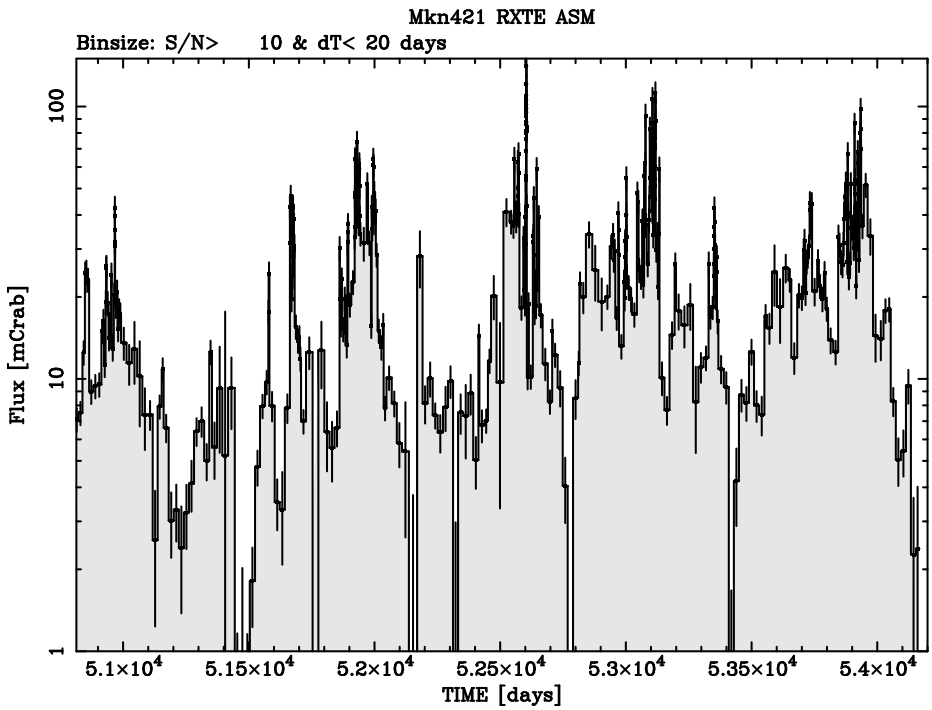

Figure 1.3 : Historical X-ray light curve of Mrk 421 by ASM/RXTE on a time period of almost 10 years. There is smaller, shorter timescale variability on top of larger longer timescale variability, while the existence of variability is detected on almost all the accessible timescales.

of photons received is smallest. Some examples of these blazars include Mrk 421, Mrk 501, PKS 2155-304, OJ 287, BL Lacertae, 3C 454.3, PKS 1510-089, 3C 273 and 3C 279. We can therefore study their broadband variability by means of full SED and inter-band cross-correlations. The simultaneous multiwavelength data sets on the time axis provide us an extra dimension to study the physics of blazar jets.

The correlation of the multiwavelength variability of blazars is of particular importance and has been analyzed extensively. The correlated variability of the two components of the SED may indicate that they originate from the same population of emitting particles. This kind of correlation has been established for several sources (Fossati et al., 2008; Acciari et al., 2011; Abdo et al., 2010a). But there are also occasions of uncorrelated flares observed (Krawczynski et al., 2004). There are also other variability features that awaits explanation, such as the time-lags between different frequencies within the synchrotron or high energy component (Ravasio et al., 2004; Tramacere et al., 2009); the symmetry of light curves at raising and decaying phase of a flare (Fossati et al., 2000a); the flux-flux amplitude correlations, e.g. the γ-ray/X-ray quadratic correlation in HBLs (Fossati et al., 2008; Aharonian et al., 2009).

1.4 Relativistic jets

Jets seem to be a universal phenomenon in the universe. There are jets existing at all scales, relativistic or non-relativistic. For relativistic jets, there are AGN jets (Kellermann et al., 1998) and galactic jet in microquasars (Mirabel & Rodríguez, 1999), while for non-relativistic jets, there are bipolar jets associated with young stars known as Herbig-Haro objects (Reipurth & Bally, 2001), and jet-like bipolar outflows in protoplanetary nebula (Bujarrabal et al., 2001). However, the physics of

jets, especially their formation and evolution, is still largely unclear.

The high energy radiation that we observe in blazars comes from the innermost regions of the relativistic jets from AGN, likely within a few parsecs from the SMBH. Because the jets are relativistic, their appearance from the observer's point of view is altered by an effect called relativistic beaming. This effect causes the emission from the jet to be anisotropic in the observer's frame. That is the reason that these radiation from the innermost regions is not observable in other types of radio loud AGN.

The effect of relativistic beaming can be described using the Doppler factor:

$$\delta = \frac{1}{\Gamma(1 - \beta cos\theta)} \tag{1.1}$$

Here $\Gamma \equiv \frac{1}{\sqrt{1-\beta^2}}$ is the Lorentz factor of the bulk motion of the flow, β is the velocity of the flow in units of c (speed of light). θ is the angle between the line of sight and the direction of the jet movement. Compared to the emission in the frame of the jet, the photon energy is altered (if $\delta > 1$) by δ, and variability time scales by $1/\delta$. The total flux we observe is enhanced by δ^4, but the flux at a specific frequency is enhanced by $\delta^{3+\alpha}$, with α being the spectral index of the power law spectrum around that frequency in the jet frame $F_\nu(\nu) \propto \nu^{-\alpha}$. However, if the bright feature we observe is a stationary emission pattern in a continuous flow instead of a moving blob as we will discuss in this thesis, the enhancement should be $\delta^{2+\alpha}$ (Lind & Blandford, 1985).

The anisotropic nature of the relativistic beaming means that, in the observer's frame, most radiation is emitted in the direction of the jet movement. An photon emitted with an inclination angle θ' in the jet frame is observed in the observer's frame at the inclination angle

$$cos\theta = \frac{cos\theta' + \beta}{1 + \beta cos\theta'} \tag{1.2}$$

This means that for $\Gamma \gg 1$, the photons emitted within the $\theta' = \pi/2$ in the jet frame will all be seen within $\theta \simeq 1/\Gamma$ in the observer's frame.

Another exotic phenomenon that can be expected in relativistic jets is superluminal motion. If the observer is looking at an angle θ with respect to the direction of jet motion, the observed apparent transverse velocity in units of c is:

$$\beta_{\rm t} = \frac{\beta sin\theta}{1 - \beta cos\theta} \tag{1.3}$$

This velocity reaches the maximum of $\beta_{\rm t} = \gamma\beta$ when $cos\theta = \beta$. When γ is much larger than 1, which also means β is close to 1, $\beta_{\rm t}$ can easily exceed 1.

Very Long Baseline Interferometry (VLBI) observations of the jet kinematics in blazars have revealed many examples of superluminal motion with apparent speed up to over 40c (e.g. Jorstad et al., 2005; Kellermann et al., 2004). These observation of superluminal motion in blazars is one of the main clues that the these jets are moving close to our line of sight, with highly relativistic velocity.

1.5 Radiation mechanisms

Most information we obtain in astronomy comes from electromagnetic radiation. Blazar is not an exception. In fact, they are such strong emitters that they radiate in almost every wavelength. As we mentioned in §1.2 their SEDs always show two major components. The low energy one is known for sure to be synchrotron radiation due to the detected linear polarization in radio and optical band.

Synchrotron emission is the result of high energy charged particles gyrating around magnetic field. It is the relativistic counterpart of cyclotron radiation. It is generated by the acceleration of particles perpendicular to the line of movement. The synchrotron emission by any reasonable distribution of particles is partially linearly

polarized in the direction perpendicular to the projection of the magnetic field onto the plane of the sky (Rybicki & Lightman, 1979). So the observation of the polarization also indicates that the magnetic field in blazars is somehow ordered, rather than completely chaotic. A process that accompany synchrotron emission is synchrotron self-absorption. It is the process of a photon being absorbed, and giving its energy to the charged particle. For typically inferred conditions, this process becomes important at radio frequency and cut off the spectrum at low frequency with a spectral index of $-5/2$.

The synchrotron spectrum by mono-energetic particles is relatively narrow. So the broad flat spectrum observed in blazars must come from particles with flat non-thermal distribution such as power-law distribution.

The power of synchrotron radiation emitted by a single electron of energy $\gamma m_e c^2$ is:

$$P = \frac{4}{3}\sigma_{\rm T} c \beta_{\rm e}^2 \gamma^2 U_{\rm B}, \tag{1.4}$$

while the critical frequency of synchrotron radiation is (Rybicki & Lightman, 1979):

$$\omega_{\rm c} = \frac{3\gamma^2 q B sin\alpha}{2 m_e c}. \tag{1.5}$$

Here σ_T is the Thomson cross section, $\beta_{\rm e}$ is the velocity of the electrons in units of c, $\gamma = 1/\sqrt{1-\beta^2}$ is the Lorentz factor of the electrons, $U_{\rm B} = \frac{B^2}{8\pi}$ is the magnetic energy density, B is the magnetic field strength, q is the charge of particle, α is the pitch angle, i.e. the angle between field and velocity, m is the mass of the particle.

In practice, the synchrotron spectrum we observe is rarely produced by a single particle. A frequently assumed non-thermal particle distribution is a power-law distribution, where the number density $N(\gamma) \propto \gamma^{-p}$. The photon spectrum emitted

by particles with power-law distribution is also power-law ($P(\omega) \propto \omega^{-s}$) with index $s = (p-1)/2$.

The origin of the high energy component of the blazar SED still remains an issue under debate. One major candidate is inverse Compton scattering of low energy photons by the same synchrotron emitting electrons. Different models use different sources of the low energy photons. This gives rise to the difference between the synchrotron self-Compton (SSC) model and the external Compton (EC) model. In the SSC model, the same synchrotron emission observed at lower energy provides the seed photons for inverse Compton scattering; in the EC model, the seed photons come from somewhere external to the jet. There are several possible sources of these photons, such as accretion disc, broad line region (BLR), IR torus, X-ray corona, or cosmic background radiation.

Compton scattering is the high energy counterpart of Thomson scattering, in which low energy photons are scattered elastically by electrons. At high energy ($h\nu \ll mc^2$ no longer stands in the rest frame of the electrons), quantum effects begin to appear. The scattering is no longer elastic. The photon and electron exchange energy even in the rest frame of the electrons. The scattering cross section also begins to decrease dramatically when $\frac{h\nu}{mc^2}\gamma \sim 1$. So Compton scattering becomes not very efficient at high energies. This is called the Klein-Nishina (KN) effect.

Inverse Compton (IC) scattering is when the electron is more energetic than the interacting photon, so energy is transferred from the electrons to the photons. It is the same as Compton scattering if we look in the rest frame of the electrons. The average power emitted by the electron in single IC scatterings is (Rybicki & Lightman, 1979):

$$P_{\rm compt} = \frac{4}{3}\sigma_{\rm T} c \gamma^2 \beta^2 U_{\rm rad}. \tag{1.6}$$

$U_{\rm rad}$ is the energy density of isotropic seed photons. This is very similar to (1.4),

except $U_{\rm B}$ is replaced by $U_{\rm rad}$. However, this only holds for scattering in the Thomson regime, where $\frac{h\nu}{mc^2}\gamma \ll 1$.

Alternatively, the high energy SED component could originate from emission by hadrons instead of leptons. These models are referred to as 'hadronic' models. In these models, protons play important roles, by producing the high energy emission through proton synchrotron radiation and also by producing subsequent cascades. The pion photoproduction, and the synchrotron radiation of muons and mesons then contribute to the high energy emissions in blazars (Böttcher, 2007; Mücke & Protheroe, 2001; Mannheim & Biermann, 1992). However,strong correlation between the light curves in the high energy and low energy component of blazars, as shown in the data sets we consider in this thesis, is more naturaly explained by leptonic models, while it requires fine tuning in the case of hadronic models. It also appears that the radiative cooling time scales of protons makes it difficult to explain the very rapid high energy variability. On a more practical level, the current methods used for hadronic models is computationally time-consuming. This prohibits these models from being investigated in a time-dependent way. Based on these considerations, the hadronic models will not be the focus of this thesis.

1.6 Particle acceleration

How the particles in blazar jets, as well as in other high energy astrophysical sources, are accelerated to relativistic energies, has been a puzzle for astrophysicists for a long time (Fermi, 1949; Parker, 1958). Proposed mechanisms for particle acceleration include first order Fermi acceleration (Blandford & Eichler, 1987), second order Fermi acceleration (Borovsky & Eilek, 1986), magnetic reconnection (Ambrosiano et al., 1988), and shear layer acceleration (Rieger & Duffy, 2006).

- The first order Fermi acceleration, sometimes also referred to as diffusive shock acceleration, is a process that involves particles being energized as they cross the shock front Because of the magnetic inhomogeneity, the particles may cross the shock multiple times, each gaining certain amount of energy. Only a few particles can be accelerated to extreme high energy before they escapes, thus creating a power-law distribution of particles.

- The second order Fermi acceleration is caused by the turbulence downstream of shocks. Particles gain or lose energy through the scattering with turbulence. Because the chance of gaining energy by head-on scattering is larger than the chance of losing energy by rear-on scattering, the energy of particles will statistically increase in the end. This process can be treated as the diffusion of particle energy in the particle kinetic equation.

- Magnetic reconnection is the re-arrangement of magnetic field configuration in highly conducting plasma. In that process strong current may appear and accelerate particles to high energy.

- Shear layer acceleration is the result of particle bouncing back and forth between plasma flows with different bulk velocities, and gain energy by scattering with local magnetic inhomogeneities. These shear flows can be expected in the environment of relativistic jets as the jets interact with the interstellar medium. So this process also appear to be relevant to the particle acceleration in AGN jets.

The observed multiwavelength variability of blazars provided us a chance to follow the evolution of the SEDs, therefore possibly the evolution of the underlying emitting particles. The spectral index and spectral breaks of the SED are also related to

the balance among particle acceleration, cooling and escape. So the observation and modeling of blazar jets can be an important avenue of investigation in improving our understanding of particle acceleration.

Currently the theoretical study of particle acceleration is approached with one of the three methods: test particle Monte Carlo simulation, semi-analytic solutions of the diffusion-convection equation, or particle-in-cell simulation (e.g. Baring et al., 1994; Kirk et al., 2000; Spitkovsky, 2008). However, since what we observe in blazars and many other high energy astrophysical phenomena is the emission spectrum, we need direct combination of these theories with radiation theory to calculate the expected spectrum and variability. Because of the complexity of both kinds of theories, this kind of work still remains relatively basic with significant simplification in both the acceleration and radiation (Kirk et al., 1998; Katarzyński et al., 2006; Tramacere et al., 2011). We will discuss the treatment of particle acceleration in our blazar model in §4.

1.7 Open Questions

Our observation capability is growing rapidly with the lauch of space telescopes like Fermi and Chandra, as well as ground based observations such as VLBA, MAGIC and HESS. However, there are still a lot of basic knowledge about blazars that is still lacking. For example,

- what is the radiation mechanism responsible for the high energy emission;
- what is the process that accelerate particles;
- what is the site of the high energy emission;

- are we observing the switch up and down of the same plasma, or are we observing newly energized plasma being ejected intermittently.

A potential route that may lead to the answers of these questions is exploring the multiwavelength variability of blazars. The observational aspect of this route is already being paved (see §1.3). However, the understanding of the rich phenomena observed requires signigicant effort in building an accurate time-dependent radiative transfer model.

The good news is the multiwavelength variability of blazars can contain information on many aspects of the relativistic jets; the bad news is that the effects of these different aspects of the jets are tangled, and including them in a self-consistent model is a demanding task. The complex situation of how the amplitude and time scale of variability at each wavelength differ, and how the light curves at different wavelength lag or lead each other, is tied to the geometry and inhomogeneity of the jets, as well as the dynamics of the emitting particles. The problem is further complicated by the light travel time effect (LTTE), i.e. the finite time the photons need to travel across the jet is comparable to the variability time scale we are looking at, hence we have to consider its effect on the evolution and observation of the jet. When the LTTE dominates over the fast electron evolution, which is likely the case for blazar jets based on the observed fast variability, the light curves become direct manifestations of the geometry and inhomogeneity of the jet. In order to take advantage of the light curves and multi-epoch SEDs we obtained through multiwavelength campaigns and seek answers to the open questions, it is necessary to build a time-dependent model that has multizone capability to account for the source inhomogeneity, and at the same time handle the LTTE and other particle processes correctly, and in the end reproduce what we observe. There have been some efforts in the past, with significant progress.

But despite the importance of LTTE being widely recognized, it has never been fully considered. We will discuss the LTTE in more detail in §3.1.2. The numerical model we built to calculate the LTTE in a multizone 2D geometry is introduced in §2.

1.8 Structure of the thesis

We will first discuss the radiative transfer numerical code we have adopted and developed in §2. Then we will discuss three topics that all involve using this code. In §3 we apply this code to model the multiwavelength variability of Mrk421, and compare the result of the simulation with the result of a simplified geometrical toy-model, in order to understand the importance of the geometrical effects. In §4 we focus on the X-ray time lags in TeV blazars. In particular, stochastic particle acceleration and particle escape are used to explain these lags. We also discuss the X-ray/γ-ray quadratic relation produced in these cases. In §5 the focus of our study switch from HBL to FSRQ. At the same time, the model we use switch from pure SSC model to the one that includes external radiation field. We make our general conclusion in §6.

In order to keep the notation light, we will use primes for blob-frame values sparingly, mostly to distinguish photon energies, luminosity and times (E, L, t, τ). We do not prime quantities that are usually not ambiguous because they are only referred to in the blob-frame, such as magnetic field strength (B), source size (R, Z), electron Lorentz factor (γ), density ($n_{\rm e}$). Similarly, we do not use primes when the context is clear (for instance in the discussion of the Fokker–Planck equation).

Chapter 2

Monte Carlo/Fokker-Planck Code

Our code couples Fokker–Planck (F-P) and Monte Carlo (MC) methods in a 2 dimensional (cylindrical) geometry. It is built on the MC radiative transfer code developed by Liang, Böttcher and collaborators (Canfield et al., 1987; Böttcher & Liang, 2001; Böttcher et al., 2003), parallelized by Finke (2007). Account of earlier development of this MC/FP code can also be found in Finke (2007). The Monte Carlo method is ideal for multi-zone 2D/3D radiative transfer problems. Due to its tracking of the trajectory of every photon, LTTE are automatically accounted for, regardless of the geometry.

We modified the parent code significantly in several aspects, to make it more generally applicable, in particular to the physical conditions of the active region in a blazar jet. Some technical information of this code is presented in Appendix A.

2.1 Code Structure

The code separates the handling of photon and electron evolution. The electron evolution is governed by the Fokker–Planck equation, as commonly done (e.g. Fabian et al., 1986; Coppi, 1992; Coppi et al., 1993; Kirk et al., 1998; Makino, 1999; Kataoka et al., 2000; Chiaberge & Ghisellini, 1999). Photons are dealt with by the MC part of the code, which tracks photon production and evolution by different mechanisms, including IC scattering with the current electron population, *and* propagation. The

code's basic structure and work flow is illustrated in Fig. 2.1.

There are two main nested loop structures. Since the evolution of the electron distribution is faster than that of the photons, each MC cycle contains several F-P (electron) cycles. Therefore the code has two main time-steps: a longer MC time-step ($\Delta t'_{\rm MC}$), within which the F-P equation routine performs the evolution of the electron spectrum on shorter, variable length, time-steps ($\Delta t'_{\rm F-P}$). We describe them in more details in the next Sections.

2.2 Geometry

As illustrated in Fig. 2.2, the code is built with 2D cylindrical geometry, with symmetry in the azimuthal direction. The volume has radius R and length Z, and it is divided evenly into zones in the radial and vertical directions (r and z coordinates, $n_{\rm r}$, $n_{\rm z}$). In all runs presented in this thesis $n_{\rm r} = 9$ and $n_{\rm z} = 30$. The number of zones sets the resolution of the simulation for what concerns spatial inhomogeneities in the physical properties, either as directly set up or because of their different evolution (e.g. radiation energy density will always develop a radial profile, in turn inducing a radial profile in the electron spectra). In the scheme adopted for this thesis the number of zones is also related to the duration of the Monte Carlo time-step (see § 2.3). For scenarios where the variability is produced by a perturbation crossing the simulation volume moving along the z axis, spatial/temporal resolution in the z direction is more important, hence we select a larger $n_{\rm z}$.

This geometrical setup is adequate for the cases we want to study since the assumption is that the active region is a portion of a collimated jet. In principle, the code setup is flexible enough that slightly different geometries could be simulated via the parameter settings in each zone (e.g. some zones can be setup as empty).

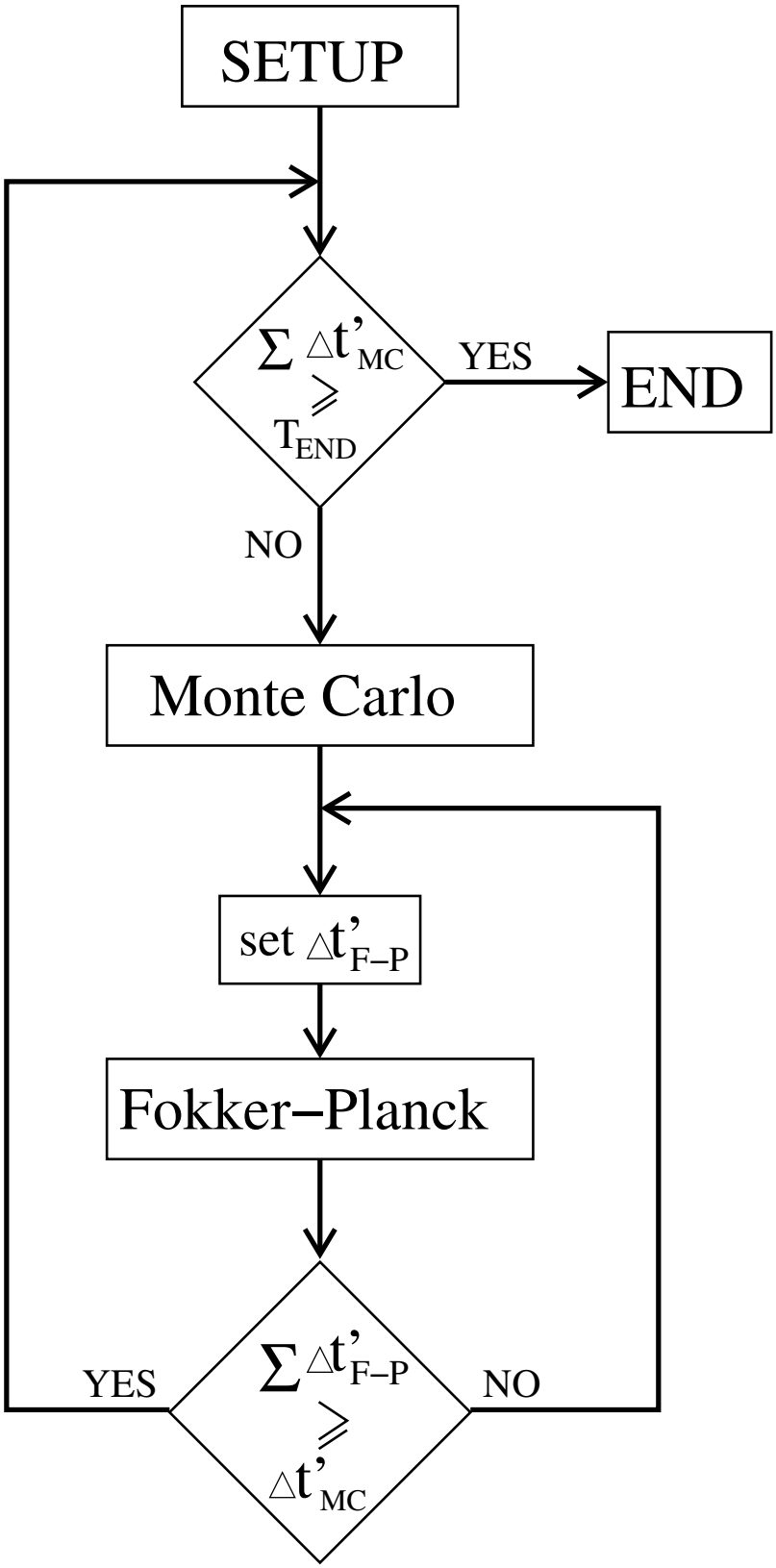

Figure 2.1 : Basic structure and work flow of the code. The Monte Carlo block handles photon emission/absorption processes (e.g., synchrotron, IC, pair annihilation, self-absorption, escape). The MC time-step is determined at setup and it does not change. The Fokker-Planck block handles electron processes (e.g., injection, cooling, pair production, escape). The F-P time-step is adjusted at each iteration according to the current physical conditions.

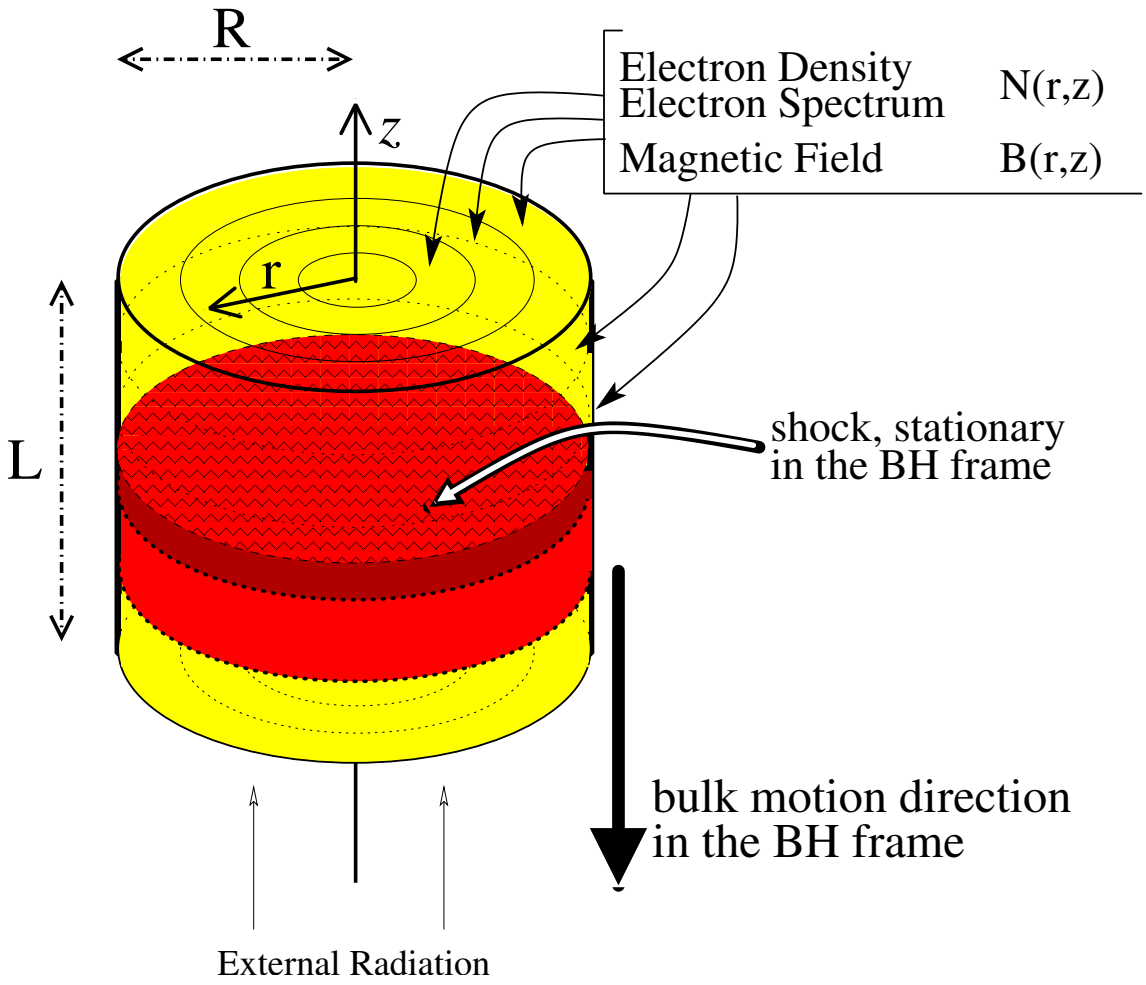

Figure 2.2 : The geometry of the blob model. The volume is divided into different zones in r and z directions, each zone with its own electron distribution and magnetic field. We also schematically show the setup for the variability of the simulations presented here. The hatched layer represents the stationary shock (§2.6.2). The blob, simulation volume, is moving downward and crossing the shock front. Zones that crossed the shock at earlier times have had some time to radiate the newly injected energy and are plotted in lighter color shades. Because of relativistic beaming, illumination by external photons can be approximated as coming only from the bottom of blob, in the upward direction.

Each zone has its own electron population (spectrum, density) and magnetic field. They can be setup individually and their time evolution is independent from each other, except for the effect of mutual illumination. The code assumes that electrons stay in their given zone and do not travel across zones*, but photons move freely among different zones. The radiation emitted by the blob is registered in the form of a pseudo-photon list (see §2.3.1), with time, direction and energy (see also Stern et al., 1995).

All the calculations are done in the blob rest frame. The transformation of all the quantities into the observer's frame is performed afterwards. The output is analyzed using a separate post processing code to produce SEDs and light curves. Since the product of the code is effectively a photon list, we have significant freedom in the choices of bin sizes for time, energy, and angle, mostly limited by statistics, much in the same way as for actual observations. Hence, we can tailor the simulation results to the characteristic of the observations that we want to reproduce (e.g. time binning, energy bands).

In all cases presented in this thesis, the observed spectrum is obtained by integrating the beamed photons over a small solid angle centered around the angle θ between jet axis and observer, assumed as customarily to be $\theta = 1/\Gamma$, for which also $\delta = \Gamma$. The typical width of the integration solid angle is $\Delta\cos(\theta) \sim$ few $\times\, 10^{-4}$.

---

*The electron Larmor radius is very small for the energies and magnetic field strengths typical for the active region of a blazar jet, at least those studied here. For instance, for $\gamma = 10^6$ and $B = 0.03\,\mathrm{G}$, $r_\mathrm{L} = \frac{m_e c^2}{eB}(\gamma^2 - 1)^{1/2} = 5.7 \times 10^{10}\,\mathrm{cm}$, to be compared with source size of the order of $10^{16}\,\mathrm{cm}$. However, if oriented magnetic field is considered, electrons can travel along the field lines. In that case we are making a simplification to the model here.

2.3 The Monte Carlo section

The MC part of the code uses the current electron distribution, as updated in the F-P section of the code. It handles all processes that involves changes in the radiation field, such as Compton scattering and the production of new photons by various radiative processes, the most important of which for our case is synchrotron emission. Other notable processes are pair production and annihilation, and synchrotron self-absorption.

The MC time-step is currently a user-set parameter, part of a run input setup. We adjust it depending on the geometry of the problem, e.g. shorter than the light crossing time of the smallest zone, and requirements of physical accuracy, for instance with respect to the fact that during each MC time-step the code does not change the electron distribution, which is evolved only during the F-P section of the code (i.e. ensuring that $\Delta t'_{\rm MC} < \tau'_{\rm cool}(\gamma)$ for the highest energy electrons.)

2.3.1 Monte Carlo particles

Since it is impossible to follow every individual photon a common technique used in radiative transfer problems is to group them into packets, pseudo-photons (e.g. Abbott & Lucy, 1985; Stern et al., 1995), to which we will refer as Monte Carlo particles. Every MC particle k represents $n_{\rm k}$ photons with the same energy, the same velocity vector, at the same position and time, carrying a total energy of $E_{\rm k} = n_{\rm k}(\nu_{\rm k})\, h\nu_{\rm k}$. $E_{\rm k}$ and $n_{\rm k}$ are also referred to as energy weight and statistical weight of the MC particle, respectively.

The MC particles are born in the volume through emission processes, primarily synchrotron radiation in our case. The luminosity of the newly radiated synchrotron contribution is computed and converted into MC particles at random frequencies with

probabilities given by the energy distribution of the synchrotron emission.

The position within a given zone, time within the current time-step, and travel direction of the MC particle when it is generated are drawn randomly from the appropriate probability distributions.

At every time-step, each MC particle moves independently, with some probability of being IC scattered. Absorption is handled as a decrease of the statistical weight of the MC particles.

When a MC particle reaches the volume boundary, it is recorded with the full information of the escape time, position, direction, and energy, forming a list of emitted photons.

2.4 The Fokker–Planck equation

In each zone, the temporal evolution of the local electron population is obtained by solving the Fokker–Planck equation:

$$\begin{aligned}\frac{\partial N(\gamma,t)}{\partial t} = &-\frac{\partial}{\partial\gamma}\left[N(\gamma,t)\dot{\gamma}(\gamma,t)\right] + \frac{1}{2}\frac{\partial^2}{\partial\gamma^2}\left[N(\gamma,t)D(\gamma,t)\right] \\ &+ Q(\gamma,t) - \frac{N(\gamma,t)}{t_{\rm esc}}\end{aligned} \tag{2.1}$$

$N(\gamma,t)$ is the electron spectrum, γ is the random Lorentz factor of electrons, $\dot{\gamma}$ is the total heating/cooling rate. The IC cooling uses the time dependent local radiation field calculated in the Monte Carlo part of the code, with LTTEs accounted for, which is considered constant for the duration of the F-P section of the code. The full Klein–Nishina (K-N) scattering cross section is used (see §2.6.4). $D(\gamma,t)$ is the dispersion coefficient. $Q(\gamma,t)$ is the electron injection term. t_{esc} is the energy independent particle escape time scale.

The time-step of the F-P loop is adjusted automatically within the code depending

on the rate of change (gain or loss) of energy of the particles to ensure a physically meaningful solution. It is constrained to be shorter than one fourth of the MC time-step.

The energy grid used for the electrons is logarithmic in kinetic energy $x_j = \gamma_j - 1$, with 200 mesh points from $x_{\min} = 0.18$ to $x_{\max} = 3.1 \times 10^7$, i.e. $x_j = 1.1\, x_{j-1}$.

After rewriting (2.1) as

$$\begin{aligned}\frac{\partial N(\gamma,t)}{\partial t} = \frac{\partial}{\partial \gamma}\left[\left(-\dot{\gamma}(\gamma,t) + \frac{1}{2}\frac{\partial D(\gamma,t)}{\partial \gamma}\right) N(\gamma,t) + \frac{1}{2} D(\gamma,t)\frac{\partial N(\gamma,t)}{\partial \gamma}\right] \\ + Q(\gamma,t) - \frac{N(\gamma,t)}{t_{\text{esc}}}\end{aligned} \tag{2.2}$$

It is possible to discretize it as:

$$\begin{aligned}\frac{N_j^{n+1} - N_j^n}{\Delta t} = \\ \frac{1}{\Delta x_j}\Bigg[\frac{1}{\Delta x_{j+1/2}} C_{j+1/2}\; w_{j+1/2} \frac{1}{1 - e^{-w_{j+1/2}}} N_{j+1}^{n+1} \\ - \Bigg(\frac{1}{\Delta x_{j+1/2}}\; C_{j+1/2}\; W_{j+1/2} \\ + \frac{1}{\Delta x_{j-1/2}}\; C_{j-1/2}\; w_{j-1/2}\; \frac{1}{1 - e^{1-w_{j-1/2}}}\Bigg) N_j^{n+1} \\ + \frac{1}{\Delta x_{j-1/2}}\; C_{j-1/2}\; W_{j-1/2}\; N_{j-1}^{n+1}\Bigg] \\ + Q_j^{n+1} - \frac{1}{t_{\text{esc}}} N_j^{n+1}\end{aligned} \tag{2.3}$$

with

$$B_{j+1/2} = -\frac{1}{2}\left[\dot{\gamma}_j + \dot{\gamma}_{j+1}\right] + \frac{D_{j+1} - D_j}{2\Delta x_{j+1/2}},$$

$$C_{j+1/2} = \frac{1}{4}(D_j + D_{j+1}),$$

$$w_{j+1/2} = \Delta x_{j+1/2} B_{j+1/2}/C_{j+1/2},$$

$$W_{j+1/2} = w_{j+1/2}/(\exp(w_{j+1/2}) - 1).$$

Here the $j \pm 1/2$ subscripts refer to quantities computed as the average values of the two adjacent grid points, such as

$$C_{j+1/2} = \frac{1}{2}(C_j + C_{j+1})$$

An exception is that of

$$\Delta x_j = \sqrt{\Delta x_{j+1/2} \Delta x_{j-1/2}}$$

with

$$\Delta x_{j+1/2} = x_{j+1} - x_j$$

$$\Delta x_{j-1/2} = x_j - x_{j-1}.$$

In order to avoid infinity in our calculation, we set the minimum value of D to be $10^{-40} s^{-1}$.

The tridiagonal matrix formed by equation (2.3) can be solved using the standard algorithm in Press et al. (1992).

2.5 Synchrotron and inverse Compton Emissivity

The synchrotron spectrum is calculated adopting the single particle emissivity averaged over an isotropic distribution of pitch angles (Crusius & Schlickeiser, 1986; Ghisellini et al., 1988):

$$P(\nu,\gamma) = \frac{3\sqrt{3}}{\pi}\,\frac{\sigma_{\rm T}\,c\,U_{\rm B}}{\nu_{\rm B}}\,y^2\left\{K_{\frac{4}{3}}(y)K_{\frac{1}{3}}(y) - \frac{3}{5}\,y\left[K^2_{\frac{4}{3}}(y) - K^2_{\frac{1}{3}}(y)\right]\right\} \tag{2.4}$$

where $\sigma_{\rm T}$ is the Thomson cross section and

$$\gamma = \frac{E}{m_{\rm e}c^2}, \qquad \nu_{\rm B} = \frac{eB}{2\pi m_{\rm e}c}, \qquad y = \frac{\nu}{3\gamma^2\nu_{\rm B}}, \qquad U_B = \frac{B^2}{8\pi},$$

with E the total electron energy, and $K_x(y)$ is the modified Bessel function of order x.

The total emitted synchrotron power and self-absorption coefficients are calculated according to the formulæ in Rybicki & Lightman (1979).

$$\alpha_\nu = \frac{c^2}{8\pi h\nu^3}\int dE\,P(\nu,E)\,E^2\,\left[\frac{N(E-h\nu)}{(E-h\nu)^2} - \frac{N(E)}{E^2}\right] \tag{2.5}$$

where $P(\nu,E)$ is the synchrotron spectrum given above (equation 2.4).

For the total Compton cross section, we used the pitch-angle-averaged cross section given in Coppi & Blandford (1990):

$$\sigma(\omega,\gamma) = \frac{3\sigma_{\rm T}}{32\gamma^2\beta\omega^2}\Bigg[-\frac{x}{2} + \frac{1}{2(1+x)} + \left(9 + x + \frac{8}{x}\right)\ln(1+x) + 4Li_2(-x)\Bigg]\Bigg|_{x=2\gamma(1-\beta)\omega}^{x=2\gamma(1+\beta)\omega} \tag{2.6}$$

Where $Li_2(z)$ is the dilogarithm, which is evaluated numerically. To get the total cross section for a photon in an electron medium we need to integrate over γ, weighted by the electron energy distribution.

2.6 Major Code Improvements

In order to make this code suitable for the study of blazar jets, we have made several major changes.

2.6.1 Numerical scheme for FP equation

Rather than using the discretization scheme proposed by Nayakshin & Melia (1998), as done in Böttcher et al. (2003), we choose to adopt the implicit difference scheme proposed by Chang & Cooper (1970) to solve the FP equation in §2.4. This scheme guarantees non-negative solutions, which in runs with the original scheme resulted in wild oscillations of the electron distribution at the high energy end (for a discussion of this issue please refer to the appendix of Chang & Cooper, 1970).

2.6.2 Injection of electrons

The model of the electron injection process, as implemented currently, involves a stationary shock perpendicular to the axis of the cylinder (jet) (Fig. 2.2). Hence, in the frame of the blob the shock is traveling across the blob with a speed equal to the bulk velocity of the blob $v_{\rm bulk} \sim c$. This scenario is similar to the one discussed by Chiaberge & Ghisellini (1999). The thickness of the shock is treated as negligible[†]. The total duration of injection is thus $t'_{\rm inj} = Z/v_{\rm bulk}$, and each slice of the simulation

[†]It is negligible in the sense that it is considered active only in one zone at any given time, i.e. it never splits across a zone boundary. However, during the time it takes to travel along a Z-zone, $\Delta z/c$, particles are injected in the entire zone volume. From this point of view the 'shock' thickness is not negligible. Provided that the Δz of each zone is small this approximation is reasonable. For the cases presented here, $\Delta z/c/\delta \leq 500\,{\rm s}$.

volume along the z axis will eventually have an injected energy of $L'_{\rm inj}\Delta z/v_{\rm bulk}$, where $\Delta z = Z/n_{\rm z}$ is the thickness of one slice.

Electron injection is included in the Fokker–Planck equation through the term $Q(\gamma, t)$. The shock moves at the speed of $v_{\rm bulk}$ every F-P time-step. When the shock front is located in a given zone, electron injection is active ($Q_{\rm shock} \neq 0$), otherwise $Q_{\rm shock} = 0$. In the simulations presented here the injected electrons have a power law distribution with a high energy exponential cutoff

$$Q_{\rm shock}(\gamma) = Q_0 \left(\frac{\gamma}{\gamma_0}\right)^{-p} {\rm e}^{-\gamma/\gamma_{\rm max}} \qquad {\rm cm}^{-3}\,{\rm s}^{-1} \qquad \gamma \geq \gamma_{\rm min},$$

The value of the normalization Q_0 is controlled by the parameter $L'_{\rm inj}$.

The injection and shock acceleration time-scales and durations are in principle independent from other parameters and could be set directly on the basis of a hypothesis on the details of physical processes underlying them. In this work we are treating injection, and in turn the implied process for accelerating the newly injected particles, phenomenologically, affording ourselves the freedom to assume their spectrum and time-scales.

The underlying physical mechanism for the injection process is assumed to be the first order Fermi acceleration at a shock front. The acceleration process is fast so the accelerated relativistic electrons are directly injected into the blob with a power-law distribution (e.g. Drury, 1983; Blandford & Eichler, 1987; Gaisser, 1991; Protheroe, 1996; Kirk et al., 1998).

When particle escape is included, we also consider a process we call 'pick up' of the electrons. The implementation of this process is similar to the injection process, except that it is independent of the shock. It happens constantly and homogeneously

throughout the volume. The electrons have a Gaussian distribution:

$$Q_{\rm pick}(\gamma) = \frac{Q_{\rm pick}}{\sqrt{2\pi\sigma^2}} e^{-\frac{(\gamma-\gamma_g)^2}{2\sigma^2}}$$

instead of a power-law distribution. Here $Q_{\rm pick}$ is the pick up rate, which is a free parameter. γ_g is the mean Lorentz factor of the picked up electrons, and σ^2 is the variance of the Lorentz factor. The aim is to mimic a mono-energetic particle distribution. The physical process responsible for this pre-accelerated population of electrons is unclear (see a discussion of pre-acceleration mechanisms in Kirk et al., 1994). But it can possibly be related to the fact the the bolb is running into the background medium along the jet where there might be particles escaped from and left by previous blobs. If these background particles are stationary or moving slowly in the frame of the black hole, in the blob frame they are relativistic with Lorentz factor equals the bulk Lorenzt factor of the blob. These particles can be 'captured' by the magnetic field in the blob, and become the 'picked up' pre-accelerated particles. For a pick up rate of $10^{-3} cm^{-3} s^{-1}$, and a blob length of $10^{16} cm$, the minimum background particle density required is $n = 300 cm^{-3}$. Given that we know little about the density of the cold particles in blazar jets (see Begelman & Sikora, 1987, for a way to probe the cold particles), this number is acceptable. Bases on this scenario, the energy of these electrons is assumed to come from Lorentz transformation rather than thermal energy. So the mono-energetic distribution is a better representation of the electrons compared to Maxwellian distribution.

2.6.3 Splitting of MC particles

A major difficulty of using the Monte Carlo method to model broadband emission, in the physical conditions typical of blazar jets, is the low pseudo-photon statistics at high frequencies. Observations are affected by a very similar problem.

Blazar SEDs are approximately flat in νF_ν over wide range of energies. In blue blazars, typical energies for the electrons responsible for the νF_ν emission peaks, occurring in UV-X-ray and TeV bands, are $\gamma \sim 10^4 - 10^5$. When a photon (for us a MC particle) is scattered from UV/X-ray to the TeV range, the energy of that MC particle will increase by about 9–11 orders of magnitude depending on whether it was an X-ray or UV photon, and its 'flux' will decrease by the same factor, making the statistics of the high energy IC component very poor. For constant statistical weight, the discretized spectrum would have $N_i \sim N(\nu_i)(\Delta\nu)_i$ MC particles in each bin. Our grid of photon energies is equally spaced logarithmically, so we can rewrite it as $N_i \sim N(\nu_i)\,\nu_i\,(\Delta \ln \nu)_i$, where $(\Delta \ln \nu)_i = \Delta \ln \nu$ is a constant. Hence for a photon spectrum $N(\nu) \propto \nu^{-\Gamma}$, the relative statistics of our discrete photon spectrum goes like $\nu_i^{-\Gamma+1}$. For an approximately flat SED, i.e. $\Gamma \simeq 2$, this goes like ν_i^{-1}.

An additional challenge that we face is that the IC scattering probability is very small. Under most reasonable conditions the active blob is very optically thin.

In order to mitigate these problems, we introduced a method involving the splitting of MC particles. The basic idea is that since every MC particle represents a packet of real photons treated together, it is always possible to divide them into smaller packets. If this splitting is applied in appropriate conditions, it is possible to achieve a reasonable statistics on MC particles at high frequencies with reasonable computer resources.

We have implemented MC particle splitting in three different instances within the context of the computation of IC scattering.

1. The first splitting is applied to every MC particle when it is considered for IC scattering. It is split into a large number of identical subparticles (e.g. $\sim 10^3$). The choice of this number depends on the trade off between improving the

statistics of the high energy photon spectrum and cost in terms of computing resources (time and memory), and it was based on empirical testing. Whether a particle is scattered or not is determined by comparing the distance it would travel with a distance to the next scattering stochastically determined from its mean free path. Every MC subparticle draws a separate random number, and in turn has its own chance of being scattered. All non-scattered MC subparticles are recombined into a MC particle, and travel to a new position. The subparticles that do scatter (usually a small number) will be scattered separately, to independent energies and directions (but see below). This first splitting does not necessarily save a computational time, but it decreases dramatically the memory allocation requirement to achieve the desired statistics at the highest SED energies.

2. The second instance of splitting is applied to MC (sub)particles that are being scattered. They are divided into another large number (e.g. $\sim 10^3$), and each of these MC sub-subparticles will be scattered separately, with different electrons, to a frequency and direction uncorrelated with those of the other particles. This splitting allows us to concentrate computation cycles on the rare events of actual scatterings.

3. Even with this second splitting, at highest energies the statistics of the IC photon spectrum remains very poor. To alleviate this problem, we implemented a third instance of MC particle splitting. It is triggered when one of the already twice-split MC particles is scattered to very high frequency, above a threshold that is set a priori and constant for each run, tailored to the characteristics of the studied SED. This MC particle is split again, and each of its subparticles

is re-scattered from the original frequency. That scattering is accepted only when the scattered frequency is higher than the preset threshold, otherwise it goes back and draws another random number. This third splitting offers the benefit of avoiding the use of a much larger number of subparticles in the second instance of splitting, and subsequently avoiding the production of a very large number of MC particles to be recorded in the computer memory.

Splitting causes the number of MC particles to grow during the simulation. Nevertheless, the advantage over directly setting up the simulation with more MC particles is significant both in terms of number of MC particles and more importantly because the new MC particles are created where they are most needed, thus increasing greatly the efficiency of the code. In typical runs the increase in the number of MC particles due to the splitting is modest, of the order of 10–20 per cent of the number of newly emitted synchrotron photons at each MC step.

2.6.4 Arbitrary electron energy distribution

Although the F-P equation can calculate the time dependent evolution of the electrons with arbitrary spectrum, earlier versions of the code forced the decomposition of the electron population into a low-energy thermal population plus a high-energy power law tail. The emissivity of cyclotron, non-thermal synchrotron and thermal bremsstrahlung radiation processes were calculated on the basis of this decomposition. The calculations of the synchrotron self-absorption coefficient and the total scattering cross section of a photon in the medium were dependent on this 'thermal plus power law' approximation as well. In order to make the code more general, and in particular more suitable for blazar simulations, in which there is usually a dominant non-thermal lepton population, we have entirely rewritten the relevant sections

of the code. The code now calculates all physical quantities using the actual electron spectrum, as updated by solving the F-P equation (see § 2.5)

2.6.5 Other improvements

Compared to the older version of the code, there are several side features added to increase the efficiency of the code.

- The MC part of the code assigns one zone to one computing node at a time, to create new MC particles through synchrotron radiation. When one node finishes the job, the new MC particles are stored in that node, and the code assigns another zone to it, until all zones are done. However, since each zone has its own parameters, including volume, the number of MC particles created and stored in each node will be different. The difference is worsened by the fact that the number of MC particles also increase by splitting during IC scattering, and the scattering is a random process. After all the new MC particles are born, the task of the nodes is to take care of the evolution of the MC particles stored in that node. These MC particles can come from or be in any zone, not related to which node it is stored in. Because this task is the most computational consuming part of the code, the node that has most MC particles becomes the bottle neck for the code efficiency – all the other nodes have to wait for it every time step.

  The new code now redistributes the newly emitted or scattered MC particles at the end of each MC time step, so that each computing node was assigned the same number of MC particles to handle. By doing this, the code can speed up almost linearly with the number of processors used. In the past, this increase

of code speed stalls when the number of processors becomes larger than about 10.

- The new code can also schedule the job to stop at the beginning of any MC time step, and save all the current information. Then later the simulation can begin from where it stopped last time and continue the job. This feature is extremely useful when there is an upper limit on the running time of a single job on certain computers.

2.6.6 Deactivated features

Some features of the code have been deactivated in this study. Among these are the cyclotron and bremsstrahlung emission and Coulomb scattering of electrons with protons, all considered not important in blazar jets.

2.7 Code testing

In order to test the robustness of the code, we compared the results of our code with those of other codes, for cases where some of their capabilities are comparable. We first compare the results with a non time-dependent code to test the MC radiative part of the code. Then we compare the electron evolution with a time dependent code, in a single-zone homogeneous case. Generally the results match very well.

2.7.1 Steady state SED of homogeneous models

To test how the code handles the radiative processes, we try to reproduce the theoretical SED shown in Fossati et al. (2008), for the non-extreme parameter choice (solid line in their fig. 10a). That SED was computed with a single-zone homogeneous SSC

model. The electrons are assumed to be continuously injected and reach a steady state (e.g. Ghisellini et al., 1998). For this test, we take the equilibrium electron distribution calculated in the homogeneous code as our input electron distribution, and turn off the F-P evolution of the electrons. We cut the volume into several identical zones just to make use of the parallel structure of the code. Since the single-zone model uses a spherical geometry, while our MC model uses a cylindrical geometry, we choose to use the same radius ($R = 10^{16}\,\mathrm{cm}$), but with the height of the cylinder $Z = 4/3R$, in order for the two models to have the same volume. The produced SED is shown in Fig. 2.3a in the top panel as black histogram, directly compared with that of Fossati et al. (2008). In general the two SEDs match well, except for a slight discrepancy around the peak of the IC component. This arises from the fact that the single zone model uses a step function to approximate the K-N cross section, while our code implements the full K-N cross section.

We then also tested our code with the step function approximation. The result in shown in Fig. 2.3a, middle panel. The overall shapes of the SEDs match better. The total luminosity seems a little higher in the MC model. However, it is worth noting that although we are matching the volume, the geometry is different in the two codes and this has a small effect on the IC component. Moreover, in order to achieve a reasonable statistics the emitted photons are integrated over a finite solid angle, i.e. a range of angles θ (photon direction angle with respect to the jet axis, in the observer frame). Hence for a given bulk Lorentz factor $\Gamma_{\mathrm{bulk}} = 26$, we are effectively integrating over a range of Doppler factors $\delta \simeq 23.5 \sim 28.7$, not exactly $\delta = 26$ as for the comparison model.

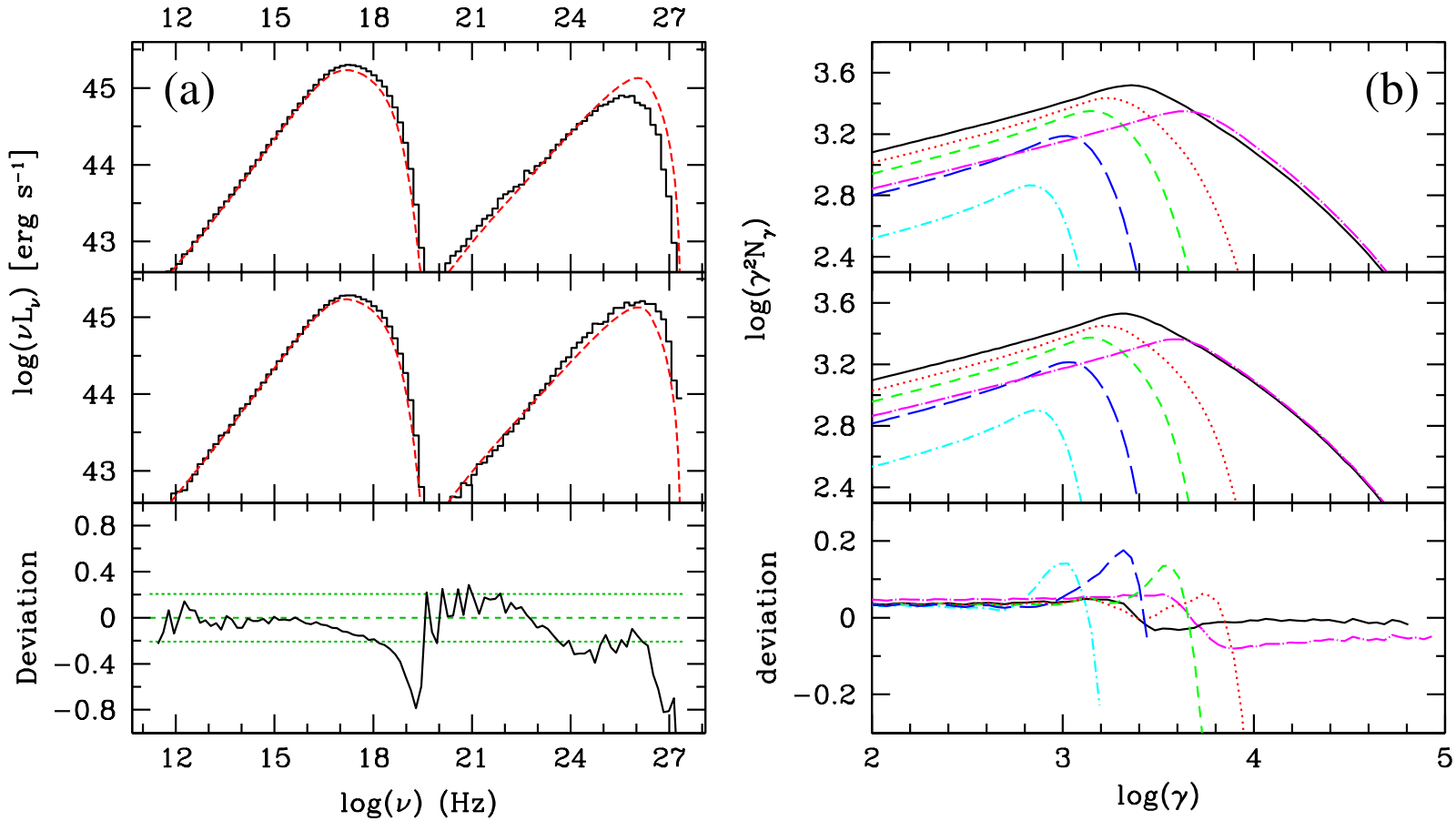

Figure 2.3 : (a) Results of the steady state homogeneous model simulation. The smooth red lines are the SEDs from Fossati et al. (2008). The black histogram is the SED produced by our MC/F-P model run with the closest possible source setup. In the top panel we used the full K-N cross section, while in the middle we used a step function approximation as done in Fossati et al. (2008). The bottom panel shows the fractional deviation, $\Delta y/\langle y\rangle$, between these two latter SEDs. Positive sign corresponds to the one-zone spectrum having a larger value. (b) Results of the time-dependent homogeneous model simulation. Electron distributions, as $\gamma^2 N(\gamma)$, for different times for our MC/F-P code (top), or the one-zone code of Chiaberge & Ghisellini (1999) (middle). In different colors and line types we plot the spectra at the following times (in units of R/c): 0.5 (magenta, long dash dot), 1 (black, solid), 1.25 (red, dotted), 1.5 (green, sort dash), 2 (blue, long dash), 3 (cyan, dot dash). In the bottom panel we show the fractional deviation, $\Delta y/\langle y\rangle$, between the spectra for the two codes. Lines are truncated at the energy where $\gamma^2 N_\gamma$ drops a factor of 30 below its peak value.

2.7.2 Temporal evolution (one zone model)

The other important aspect of our MC/F-P code, the Fokker–Planck evolution of the electrons, was tested by comparing the code with the one-zone time dependent homogeneous SSC code by Chiaberge & Ghisellini (1999). We set the number of zones to one, and used a power law injection with the same parameters they used ($B = 1\,\mathrm{G}$, $\gamma_{\rm min} = 1$, $\gamma_{\rm max} = 10^5$, $p = 1.7$, $L'_{\rm inj} = 3.69 \times 10^{41}\,\mathrm{erg/s}$, $t'_{\rm esc} = 1.5R/c$, $t'_{\rm inj} = R/c$), except that our geometry is a cylinder with $R = 1.1547 \times 10^{16}\,\mathrm{cm}$, $Z = 10^{16}\,\mathrm{cm}$, while they use a sphere with $R = 10^{16}\mathrm{cm}$.

The electron spectra at different times are shown in Fig. 2.3b; the upper panel shows the one produced by the MC code, the middle panel the one produced by the one-zone code, while the bottom panel shows the deviation. The two spectra match reasonably well, giving us confidence that our code handles the evolution of the electron distribution correctly.

Chapter 3

Modeling the multiwavelength variability of Mrk 421

3.1 Introduction

Blazars are the most extreme (known) class of AGN. They are core-dominated, *flat-radio-spectrum* radio-loud AGN. Their properties are interpreted in terms of radiation from relativistic jets pointing at us (Urry & Padovani, 1995). Because of relativistic beaming, jets greatly outshine their host galaxies thus making blazars unique laboratories for exploring jet structure, physics and origin.

Blazars emit strongly from radio through γ-ray energies. Their spectral energy distribution (SED) comprises two major continuum, non-thermal, components (Ulrich et al., 1997; Fossati et al., 1998): the first, peaking in the IR-optical-X-ray range, is unambiguously identified as synchrotron radiation of ultrarelativistic electrons. The nature of the second component, sometimes extending to TeV energies, is less clear and under debate. It is generally modeled as inverse Compton (IC) scattering by the same electrons that produce the synchrotron emission. The seed photons can be synchrotron photons (*synchrotron self-Compton*, *SSC* Maraschi et al., 1992; Marscher & Travis, 1996) or external radiation fields such as emission directly from the accretion disk, or the broad line region (BLR), or a putative torus present on a larger scale (*external Compton*, *EC*, e.g. Dermer et al., 1992; Sikora et al., 1994; Ghisellini & Madau, 1996; Błażejowski et al., 2000; Sikora et al., 2009). These models are generally

referred to as leptonic models because the particles and processes responsible for the emitted radiation are only electrons and positrons.

A second class of models, hadronic models, consider the role played by protons either by producing very high energy radiation directly via the synchrotron mechanism, or by initiating a particle cascade leading to a second leptonic population emitting a higher energy synchrotron component (Mannheim, 1998; Rachen, 2000; Sikora & Madejski, 2001; Arbeiter et al., 2005; Levinson, 2006; Böttcher, 2007; Böttcher et al., 2009).

The frequency of the synchrotron peak (νF_ν) has emerged as (one of) the most important observational distinction across the blazar family (e.g. Fossati et al., 1998), leading to the classification of blazars as 'red' or 'blue' according to their SED 'color', i.e. the location of the peak*. Fossati et al. (1998) showed that blazar SEDs seem to change systematically with luminosity; the most powerful objects are red, while blue SEDs are associated with relatively weak sources, a result supported by studies of high redshift blazars and of low power BL Lac objects (see Fabian et al., 2001a,b; Costamante et al., 2001; Ghisellini et al., 2010).

Another fundamental distinction among blazars concerns their 'thermal' spectral properties, where they encompass a wide range of phenomenology, ranging from objects with featureless optical spectra (BL Lac objects) to objects with quasar–like (broad) emission line spectra (Flat Spectrum Radio Quasars, FSRQ Urry & Padovani, 1995, for a review). This distinction is likely to have an impact on the mechanisms of production of the γ-ray component in different types of blazars, with BL Lacs being consistent with pure SSC, and FSRQ with EC. In fact in most FSRQs the prominence of the thermal components with respect to the synchrotron emission suggests that EC

*Blue and red SED objects are also called HBL and LBL, for High or Low peak.

must be dominant over SSC. The case for BL Lacs is more ambiguous. Since particles in the active region (blob) in the jet would see the external radiation greatly amplified by relativistic aberration with respect to what we measure, the fact that we do not directly detect any thermal component may not necessarily mean that in the jet rest frame its intensity is not competitive with the internally produced synchrotron radiation.

However, the broad band emission of TeV detected BL Lac objects, like Mrk 421, is well modeled with pure SSC and stringent upper limits can be set on the contribution of EC to their SEDs (Ghisellini et al., 1998, 2010).

3.1.1 Variability

Rapid and large-amplitude variability is a defining observational characteristic of blazars. It occurs over a wide range of time-scales and across the whole electromagnetic spectrum (Ulrich et al., 1997). Flux variability is often accompanied by spectral changes, typically more notable at energies around/above the peak of each SED component. Multiwavelength correlated variability studies have been a major component of investigation of blazars, but because of observational limitations so far it has been focused on blue blazars.

Blue blazars / HBLs indeed constitute a particularly interesting subclass, for their synchrotron emission peaks right in the X-ray band, and the high energy component reaches up to TeV γ-rays. The X-ray/TeV combination has been accessible observationally thanks to ground based Cherenkov telescopes and the availability of several X-ray observatories. Hence, the brightest HBLs have been studied extensively. Simultaneous X-ray/γ-ray observations showed that variations around the two peaks are well correlated, providing us with diagnostics on the physical conditions and processes

in the emission region for HBLs.

Different models have been shown to successfully reproduce time-averaged or snapshot spectral energy distributions of blazars. So far, however, there has been remarkably little work taking advantage of the information encoded in the observed time evolution of the SEDs by modeling it directly, despite the tremendous growth and improvements on the observational side, allowing in many cases to resolve SED on physically relevant time-scales, fueled by several successful multiwavelength campaigns (e.g., some of the most recent ones, for the brightest BL Lacs Sambruna et al., 2000; Ravasio et al., 2002; Takahashi et al., 2000; Fossati et al., 2000a,b; Krawczynski et al., 2004; Błażejowski et al., 2005; Rebillot et al., 2006; Giebels et al., 2007; Fossati et al., 2008; Aharonian et al., 2009).

The spectral time evolution has been studied and characterized by means of intra- and inter-band time lags, intensity correlation, and hysteresis patterns in brightness–spectral shape space. The main observed features unveiled by this type of analyses seem to be well accounted for by attributing the γ-ray emission to SSC (in a one-zone homogeneous blob model), and they emerge from the combination of acceleration and cooling and depend on the relative duration of the related time-scales (e.g. Takahashi et al., 1996; Ulrich et al., 1997; Kataoka, 2000). A less empirical, more directly theoretical interpretation of this wealth of data, requiring/exploiting the physical connection between series of spectra, has remained relatively basic despite the clear richness of the observed phenomenology (e.g., Mastichiadis & Kirk, 1997; Dermer, 1998; Li & Kusunose, 2000; Sikora et al., 2001; Krawczynski et al., 2002; Böttcher & Chiang, 2002).

3.1.2 Light Travel Time Effects

One of the biggest challenges and limitations of the current models comes from the dealing with light travel time effects (LTTE), usually treated in a simplified way, such as simply by introducing a photon escape parameter (e.g., Böttcher & Chiang, 2002).

The observed variability on time-scales of hours indicates that light travel time effects *within* the active region are very important and must be dealt with. There are two main aspects related to photon travel times that are important for an accurate study. The first, which we can call 'external' (following Katarzyński et al., 2008), is a purely geometric effect that pertains to the impact of the finite size of the active region on the observed variability, namely the delayed arrival time of the emission from different parts of the blob, and consequent smearing of the intrinsic variability characteristics (Protheroe, 2002). It is relatively simple to implement.

The second effect, internal, pertains to the impact of these same delayed times on the actual physical evolution of the variability (as opposed to just our 'perception' of it) due to the changing conditions inside the active region. This effect constitutes the real challenge for proper multi-zone modeling. In this respect the most important issue is that of the photon diffusion across the blob on the electrons' inverse Compton losses. Proper accounting of this effect is significantly more complex and computationally expensive, and traditionally neglected under the assumption that electron cooling is dominated by synchrotron losses. This is, however, a strong assumption, rarely valid, as suggested by the observation that the luminosity of the synchrotron components is at best of the same order as the IC component, more commonly lower.

It has long been realized that a simple one-zone homogeneous model is not adequate to describe the temporal evolution of the blazar jets, and that LTTE must be taken into account. McHardy et al. (2007) suggested that the observed delay between

X-ray and infrared variations in 3C 273 could be related to the time necessary for the soft (synchrotron) photon energy density to build up as the they travel across the active region.

3.1.3 Relevant Previous Work

Some progress has been made to develop multi-zone models, though with limited success because the traditional analytical approach requires significant assumptions, such as simple geometries or assumptions about the relevance of different physical processes. The inclusion of just the external LTTE is enough to yield new insights on SSC light curves, such as on the way the interplay between cooling/acceleration time-scales and source size affects the observed light curves as a function of energy and combination of the various time-scales (Chiaberge & Ghisellini, 1999; Kataoka et al., 2000; Katarzyński et al., 2008). In all the cited cases the size of the active region and the duration of the injection of fresh particles are related through $t'_{\rm inj} = R/c$, where R is the radius of a sphere or the length of a cubic region. The geometry is characterized by a single length-scale. This kind of models, not accounting for internal LTTE and non-locally-emitted radiation for IC emission, could yield correct results for the evolution of the electron distribution if synchrotron losses dominate, however even in this case their results for the evolution of the IC component are not realistic because they ignore the contribution of seed photons from other zones.

Sokolov et al. (2004) and Sokolov & Marscher (2005) were the first to include the internal LTTE to calculate the IC spectrum, for both SSC and external IC models. However, they did not properly account for it when calculating IC energy losses. Their model is thus accurate only when synchrotron losses are dominant. Observationally this corresponds (approximately) to cases where the peak of the lower energy

component of the SED (synchrotron) is significantly brighter than that of the second peak (IC).

Graff et al. (2008) developed a model taking into account all the LTTEs, but specialized to an elongated 'pipe' geometry. The geometry of the current implementation of their code is effectively one-dimensional. The lack of an actual transverse dimension represents a significant limitation when considering the LTTE, considering because of relativistic aberration we are effectively observing a jet (also) from its side.

In this thesis we have introduced a more general and flexible code to simulate blazar variability, addressing and overcoming most of the limitations affecting previous efforts.

In this chapter we will apply this code to study Mrk 421. Particle escape, stochastic acceleration, and external radiation are not included in this chapter. In §3.2 we present results of a few test cases based on the multiwavelength observations of Mrk 421 in March 2001. We summarize with a discussion of this first application and remarks about future applications and developments in §3.3.

3.2 Application to Mrk 421

Mrk 421 is the archetypical 'blue' blazar, the most luminous and best monitored object in the UV, X-ray and TeV bands. It was the first extragalactic source detected at TeV energies (Punch et al., 1992). As such it has been the target of multiple multiwavelength campaigns with excellent simultaneous coverage by X-ray and TeV telescopes. (Takahashi et al., 2000; Maraschi et al., 1999; Fossati et al., 2000a,b; Krawczynski et al., 2001; Błażejowski et al., 2005; Rebillot et al., 2006; Giebels et al., 2007; Fossati et al., 2008; Donnarumma et al., 2009).

For a first application of our code we focused on one of best flares ever observed,

occurred on 2001 March 19 (Fossati et al., 2008). It was a well defined, isolated, outburst that was observed both in the X-ray and γ-ray bands from its onset through its peak and decay. It uniquely comprised several rare favorable features, namely absence of data gaps (except *RossiXTE*'s short orbital gaps), excellent TeV coverage by the HEGRA and Whipple telescopes and large amplitude variation in both X-ray and γ-ray bands.

3.2.1 Observational constraints and goals

We aim to reproduce several observational features. Some of them can be regarded as constraints on the setup of a baseline model, as they provide guidance on the general properties and parameter values yielding an acceptable fit to the SEDs (e.g. Tavecchio et al., 1998, Bednarek & Protheroe, 1997, and Fossati et al., 2008 for an example specific for the observations studied here). In this respect, we have five fundamental observables we want to match:

- The peak frequencies of the synchrotron and IC components, $\nu_{\rm p,S}$, $\nu_{\rm p,IC}$, which for Mrk 421 are observed in the X-ray and γ-ray bands.

- The peak luminosity and the relative strengths of the two SED components, $\nu L_{\rm p,S}$, $\nu L_{\rm p,IC}$.

- The variability timescale ($t_{\rm var}$). Combined with an hypothesis on the Doppler factor it provides a constraint on the size of the blob. For Mrk 421 in X-ray and γ-ray it is typically of the order of tens of kiloseconds.

Besides giving an indication about the size of the active region, the latter can be different for different energy bands and in turn its energy dependence can provide additional constraints on the model parameters and source geometry.

There is then a set of observational features whose explanation remains to a large extent an open question. They represent the ultimate goal of our work and the driver for the development of a time dependent multi-zone model.

1. The quasi-symmetry of flare light curves, showing similar rising and falling time-scales, both in X-rays and γ-rays. The symmetry seems to be a quite common feature at several wavelengths. It would seem to support the interpretation that the flare evolution is governed by the geometry of the active region (Chiaberge & Ghisellini, 1999; Kataoka et al., 2000). However, this could be true only if all other (energy dependent) time-scales are shorter than the blob crossing time, or relevant geometric time-scale, or only for emission at energies for which this is true.

2. The characteristics of the multiwavelength correlated intensity variations. The flare amplitude is generally larger in γ-rays than in the X-ray band, and flux variations show a quadratic (or higher order) relationship that holds during both the rise and the decay phases of the flare. This behavior was observed in Mrk 421 on 2001 March 19, and also for other 'clean' flares, including for other blue blazars (e.g. Aharonian et al., 2009, reporting a cubic variation for PKS 2155−304).

3. The existence and length of inter-band (X-ray vs. γ-ray) and intra-band (soft X-ray vs. hard X-ray) time lags, often with changing sign from flare to flare (see references given above for Mrk 421). In the isolated flare of 2001 March 19, Fossati et al. (2008) report a possible lag of about 2 kilo-seconds of the TeV flux with respect to a soft X-ray band (2–4 keV), whereas TeV and harder X-rays (9–15 keV) were consistent with no lag. In turn an X-ray intraband lag was

detected.

4. The fact that even during large outbursts the optical flux changes little. This may constrain the characteristics of the particle injection, such as their spectrum (shape and density) and energy span. On the other hand, the time dependent spectral behavior of blazars has led people to speculate that there is more than one component contributing to the blazar emission (Fossati et al., 2000b; Krawczynski et al., 2004; Błażejowski et al., 2005; Ushio et al., 2009). It is not clear if this additional zone is co-spatial with the zone undergoing the flare or it is far enough elsewhere along the jet that the two do not interfere with each other and evolve independently.

5. SED shape, and its time variations, particularly around the two peaks. For Mrk 421 we mostly focus on the X-ray and TeV γ-ray spectra.

These features have been observed in several instances for Mrk 421, mostly cleanly in the case of the 2001 March 19 flare, and the other well studied TeV detected blue blazars. For the brightest blue blazars there is an extensive database of multiwavelength observations and studies of time resolved spectral variability. The phenomenology is richer and more complex than the few items just introduced, on which we focus. In this respect, one of the most interesting findings is the observation of a correlation between luminosity and position of the peak of the synchrotron component (e.g. Tavecchio et al., 2001; Fossati et al., 2000b; Tanihata et al., 2004; Tramacere et al., 2007).

In this work we are mostly aiming at illustrating the capabilities of our code with respect to investigating the above observational findings, by presenting the results of simulations of three simple scenarios.

Table 3.1 : Summary of model parameters in Chap. 3

Case	general source parameters				back-/fore-ground component				injected component		
	R	Z	Γ	B	$\gamma_{\rm min}$	$\gamma_{\rm b}$	$\gamma_{\rm max}$	$n_{\rm e}$	$\gamma_{\rm min}$	$\gamma_{\rm max}$	$L'_{\rm inj}$
	10^{16}	10^{16}									10^{40}
	cm	cm		G				$\rm cm^{-3}$			$\rm erg\ s^{-1}$
1: with 'background'	1.0	1.33	33	0.1	50	2×10^4	2×10^5	4.0	50	1.9×10^5	5.5
2: with 'foreground'	1.0	1.33	33	0.08	50	1×10^4	1×10^5	6.0	50	1.9×10^5	6.0
3: better TeV spectrum	1.5	2.0	46	0.035	50	2×10^4	2×10^5	1.56	50	1.9×10^5	3.2

All background or foreground components electron spectra are broken power laws (with exponential cutoff), with spectral indices $p_1 = 1.5$, $p_2 = 2.5$ $(= p_1 + 1)$. The injected power law has spectral index $p = 1.5$ in all cases.

3.2.2 On model parameters

Our homogeneous (at least initially) SSC model is defined by the following quantities (see also Table 3.1):

- source size/geometry (R, Z, or aspect ratio),
- Lorentz factor (Γ),
- magnetic field strength (B),
- various parameters describing the electron spectrum, e.g. four for an injected power law: $\gamma_{\rm min}$, $\gamma_{\rm max}$, p, $L'_{\rm inj}$. For a broken power they would be six because there would be a spectral break $\gamma_{\rm b}$ and two spectral indices (p_1, p_2) instead of one.

With simple considerations we can reduce the number of model parameters to constrain from 8 (or 10) to 5 (B, Γ, R, $\gamma_{\rm max}$, $L'_{\rm inj}$) and as illustrated in the previous section we have 5+ fundamental observables to do it.

The source aspect ratio can be at least qualitatively constrained by the profile of the flare light curve, for in first approximation extreme geometries would yield fairly distinctive flare shapes due to LTTE. For this work we adopted a conservative, stocky, volume aspect ratio $R/Z = 3/4$, i.e. width:length = 3:2.

Among the electron spectrum parameters, $\gamma_{\rm min}$ and p (or p_1) can be set with reasonable confidence based on considerations on the SED shape and variability (or lack thereof) at frequencies below the synchrotron peak. The precise value of $\gamma_{\rm min}$ is however not well constrained by observations. The emission by electrons at $\gamma \leq 10^3$ would be below the optical band, where there is not much simultaneous coverage, and emission by much lower energy electrons would fall in a band (i.e. $\nu \leq 10^{11}$ Hz) where

observations suggest that the SED is dominated by radiation from other regions of the jet (e.g. Kellermann & Pauliny-Toth, 1981). Moreover, cooling time-scales for electrons at those energies are long compared with the typical duration high-density multiwavelength campaigns (see eq. 3.2), making it difficult to set a constraint on $\gamma_{\rm min}$ based on variability. Higher values of $\gamma_{\rm min}$ affect the synchrotron emission in the optical band and in turn the IC component, mainly in the GeV band, and therefore we can assess their viability with current and future observations. Given that during the 2001 campaign (Fossati et al., 2008) there seemed to be a modest level of variability in the optical band, $\Delta m_{\rm V} \simeq 0.4$, though not directly from observations simultaneous with the March 19 flare, we simulated scenarios where the injected electron population has a relatively low $\gamma_{\rm min} = 50$ (Table 3.1). We choose to truncate the electron distribution at this value also because the number of low energy electrons grows rapidly, thus increasing significantly the computational time without adding much to the investigation presented here; as noted, emission from lower energy electrons would not be detectable, and they would not significantly alter the properties of the emission and its variability observed in blue blazars. This is of course an assumption that is valid for this work but that should be revisited, for instance for the study of red blazars.

The spectral indices of the injected electron distributions p or p_1 ($p_2 = p_1 + 1$ as expected for a cooling break) are mostly constrained by the shape of the synchrotron SED at energies below the optical range. The preferred value for $p, p_1 = 1.5$ constitutes a somewhat hard spectrum but it is consistent with values discussed by several particle acceleration studies. In particular, stochastic ($2^{\rm nd}$-order Fermi acceleration) and acceleration at relativistic shear layers have been suggested to produce very hard ($p < 2$) particle spectra (Virtanen & Vainio, 2005; Stawarz & Ostrowski, 2002; Rieger

& Duffy, 2004, 2006).

Next, we discuss some general arguments and estimates for values of the fundamental physical parameters. We then present and discuss the results obtained with the set of parameters that we deemed more successful, and in turn 'fit' the SEDs and light curves of the 2001 March 19 outburst testing several different parameter combinations, including the possible dilution by emission from a different region of the jet not involved in the flare, and the presence of a pre-existing electron population in the region that becomes active.

3.2.3 Estimates of active region parameters from observables

Key parameters in the modeling of blazars with the SSC model include the Lorentz factor, the magnetic field strength, the size of the volume, and the energy of the electrons that are responsible for the synchrotron peak of the SED, $\gamma_{\rm p}$. This latter is associated with a break in the electron distribution or its maximum, depending on the spectral index. We use the observational results of Fossati et al. (2008) as the benchmark of our analysis. There are several observed features that constrain the value of these parameters (see previous section). Additionally, independent estimates of the relativistic beaming parameters of blazars, from observed superluminal motion and population statistics, yield Lorentz factors of the order of tens (Urry & Padovani, 1995). As we mentioned before, we make the common assumption to be observing the source at the angle $\theta = 1/\Gamma$, hence $\delta = \Gamma$ (see Cohen et al., 2007, for a deeper statistical analysis, showing that the most likely combination is $\Gamma \sin\theta \simeq 0.7$).

The observed peak of the synchrotron component (at energy $E_{\rm p,S}$) results from the combination of electrons' γ, B and δ. Assuming mono-energetic emission the

relationship is $E_{\rm p,S} = \nu_{\rm B}\,\gamma_{\rm p}^2\,\delta$. For Mrk 421 $E_{\rm p,S} \simeq 1\,{\rm keV}$. Parameterized† on fiducial values for these three parameters the $\gamma_{\rm p}$ of the electrons emitting at the synchrotron peak is:

$$\gamma_{\rm p} \simeq 1.7\times10^{5}\,\left(\frac{B}{0.1\ {\rm G}}\right)^{-1/2}\left(\frac{\delta}{30}\right)^{-1/2}\left(\frac{E_{\rm p,S}}{1\ {\rm keV}}\right)^{1/2} \tag{3.1}$$

If the IC component peak resulted from scattering of photons of the synchrotron peak in Thomson regime we could directly infer the energy of the electrons emitting at both SED peaks as

$$\gamma_{\rm p} \simeq \left(\frac{3\,E_{\rm p,IC}}{4\,E_{\rm p,S}}\right)^{1/2} \simeq\ 2.7\times10^{4}\left(\frac{E_{\rm p,IC}}{1\ {\rm TeV}}\right)^{1/2}\left(\frac{E_{\rm p,S}}{1\ {\rm keV}}\right)^{-1/2}$$

with $E_{\rm p,IC}$ is the peak energy of the IC component. However, as discussed by Fossati et al. (2008, see Fig. 11 therein), the SED shape and variability time-scale observed in Mrk 421 in 2001 favor parameters such that the scattering between electrons at $\gamma_{\rm p}$ and synchrotron peak photons at $E_{\rm p,S}$ would happen in the K-N regime (see also Tavecchio et al., 1998; Bednarek & Protheroe, 1999). In this case the IC peak energy would be largely independent of $E_{\rm p,S}$ and the expression would instead be:

$$\gamma_{\rm p} \simeq \frac{E_{\rm p,IC}}{\delta\,m_{\rm e}c^2}\ \simeq\ 6.5\times10^{4}\left(\frac{E_{\rm p,IC}}{1\ {\rm TeV}}\right)\left(\frac{\delta}{30}\right)^{-1}.$$

Requiring that the condition for Thomson regime, $\gamma x' \leq 3/4$ (where $x' = E'_{\rm target}/(m_{\rm e}c^2)$), holds true for $E'_{\rm target} = E'_{\rm p,S}$ and $\gamma = \gamma_{\rm p}$, one can derive a rough estimate of what (B, δ) combination would be necessary to push into the Thomson regime the scattering between $\gamma_{\rm p}$ and its own synchrotron photons, emitted at $E_{\rm p,S}$, i.e. to make the IC peak the exact SSC match of the synchrotron one.

$$\left(\frac{B}{0.1\ {\rm G}}\right)\left(\frac{\delta}{30}\right)^{3} \geq 220\left(\frac{\mathbf{E}_{\rm p,S}}{\mathbf{1}\ {\rm keV}}\right)^{\mathbf{3}}$$

†Because the redshift of Mrk 421 is small, $z = 0.031$, for simplicity we left out factors $(1+z)$.

As shown by Fossati et al. (2008), it is indeed possible to achieve an acceptable SED fit with high B and δ. However, while this kind of model matches equally well a static SED, its smaller blob size and extreme Lorentz contraction make it implausible when compared with more dynamic observational findings, beginning with the variability time-scales.

The rest frame synchrotron cooling time can be expressed as function of electron energy and the magnetic field:

$$\tau'_{\rm cool,S} = \frac{7.7 \times 10^8}{\gamma B^2} \ \ {\rm s} \tag{3.2}$$

or, more directly related to observables, in terms of observed photon energies:

$$\tau'_{\rm cool,S} = 4.6 \times 10^5 \left(\frac{B}{0.1\ {\rm G}}\right)^{-3/2} \left(\frac{\delta}{30}\right)^{1/2} \left(\frac{E_{\rm S}}{1\ {\rm keV}}\right)^{-1/2} \ \ {\rm s} \tag{3.3}$$

or, in the observer's frame,

$$\tau_{\rm cool,S} = 15.1 \left(\frac{B}{0.1\ {\rm G}}\right)^{-3/2} \left(\frac{\delta}{30}\right)^{-1/2} \left(\frac{E_{\rm S}}{1\ {\rm keV}}\right)^{-1/2} \ \ {\rm ks} \tag{3.4}$$

showing its dependence on the inverse square root of the energy of the observed photons.

A general constraint among the observed variability time-scale and source size and time-scale of the acceleration, injection or cooling process is:

$$t_{\rm var} \geq \frac{1}{\delta} \max\left(\tau'_{\rm cool}, \tau'_{\rm acc}, t'_{\rm inj}, \frac{R}{c}, \frac{Z}{c}\right)$$

As noted in Section 2.6.2, in this work we take a simplified approach, whereby we do not specify the acceleration mechanisms underlying the particle injection, and we choose to link the injection time-scale to the geometry of the source, namely its dimension along the jet axis, Z. Hence we have a simplified relationship with the

observed variability, and considering that the 2001 March 19 flare has a flux doubling and halving time of the order of 10^4 s, we have approximately

$$\max\left(\tau'_{\rm cool}, \frac{R}{c}, \frac{Z}{c}\right) \simeq \max\left(\tau'_{\rm cool}, \frac{R}{c}\right) \simeq 10^4\,\delta \quad \text{s}$$

Please note that this constraint could actually vary with the observed band because some time-scales are likely to be energy dependent.

If the IC cooling rate is similar to the synchrotron cooling rate $\tau'_{\rm cool} \sim \tau'_{\rm cool,S}/2$. The condition $\tau'_{\rm cool} < R/c$ translates into

$$E_{\rm S} > 0.46 \left(\frac{R}{10^{16}\ {\rm cm}}\right)^{-2} \left(\frac{B}{0.1\ {\rm G}}\right)^{-3} \left(\frac{\delta}{30}\right) \quad \text{keV}$$

From the constraints and relationships illustrated above we infer that a good starting point to model the SED of Mrk 421 is a combination of $R \sim 10^{16}$ cm, $B \sim 0.1$ G, $\Gamma \simeq \delta \sim 30$, $\gamma_{\rm p} \sim 10^5$.

Because of computational limitations we did not perform an actual fit to identify the best set of parameters values reproducing the SED and the flare evolution properties. We explored a limited range of values for R, B, Γ around the values obtained from the above analysis, and focused on changes of the maximum electron energy $\gamma_{\rm max}$ and the injected power $L'_{\rm inj}$.

We ran a large number of short simulations aimed at sampling a reasonable range of values around our initial guesses and evaluated them mostly on the basis of their matching the X-ray spectra and variability. In a second stage we honed in on the best cases and adjusted the parameters by means of full length simulations[‡].

[‡]A typical run takes around 24 hours on eight Xeon 2.83 GHz CPU cores, using up to 16 GB of memory. As currently implemented the code does not scale well with the number of CPUs, only gaining a factor of three in speed by going to 96 CPUs. The bottleneck is mostly due to the longer computational time required by the zones with larger volume because it scales with the number of photons contained in each zone.

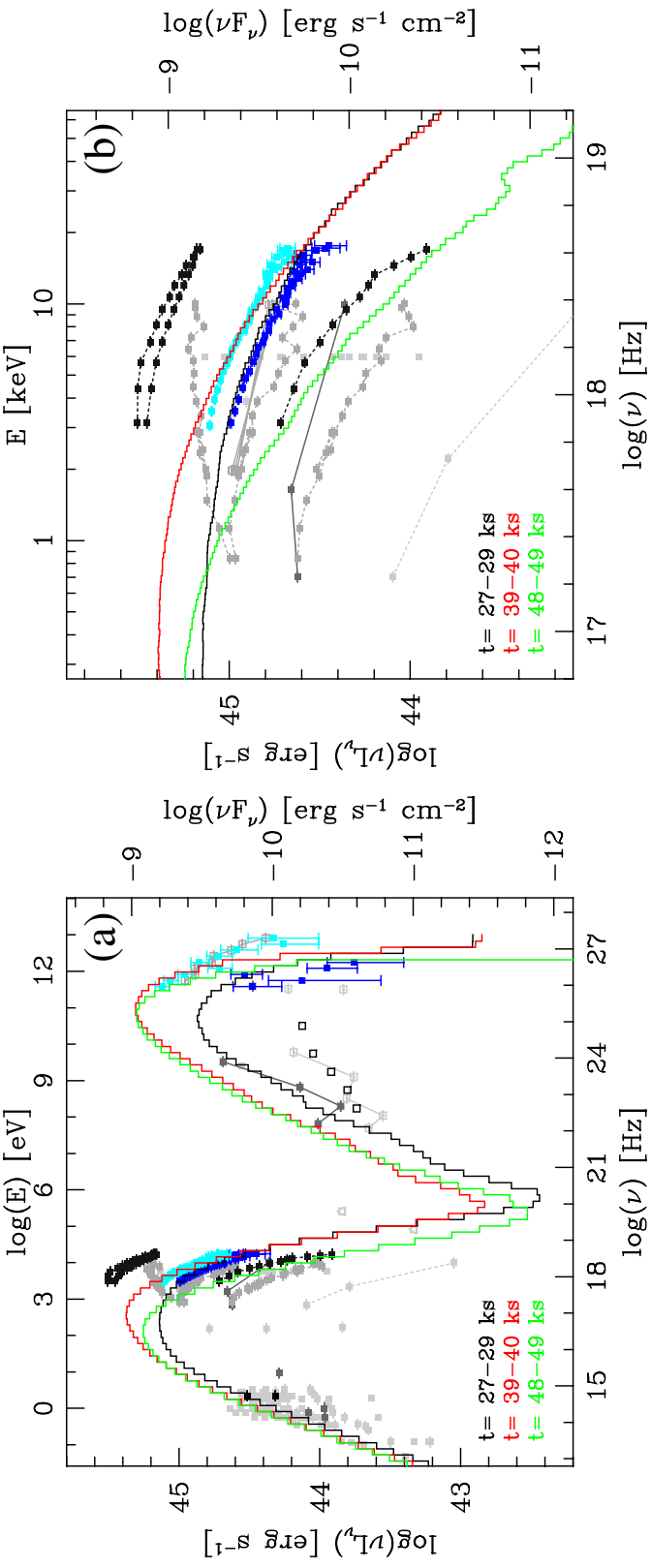

Figure 3.1 : SED of the first case, with pre-existing background electron population. (left) Broad band SEDs for three representative times (see labels) during the simulation of the flare. Observed spectra for high and low states during the 2001 March 19 flare in X-ray and TeV γ-rays are plotted in cyan and blue. Other historical data points in grey or black are the same as in Fossati et al. (2008). The black empty squares in the GeV γ-ray band are the *Fermi*/LAT 1-year averages in five bands. (right) Zoom centered on the X-ray band.

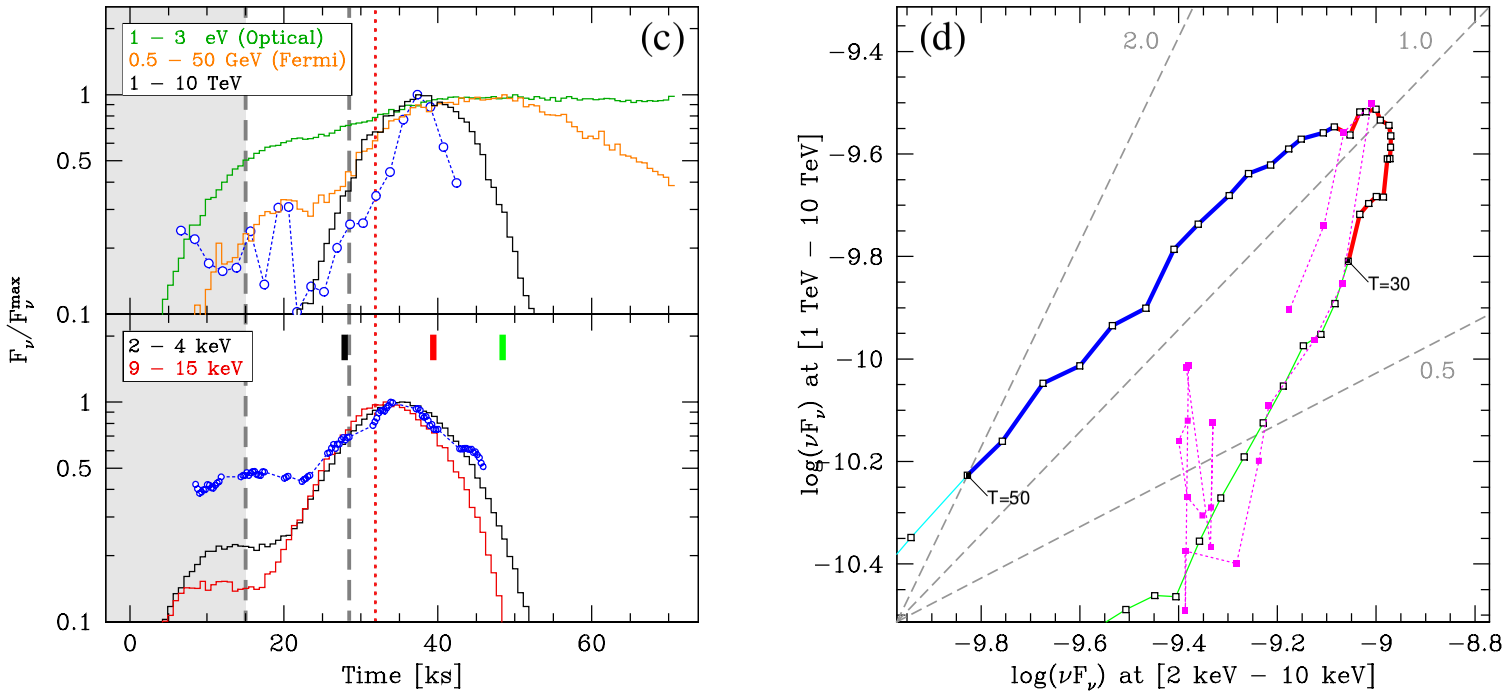

Figure 3.2 : Light curves and flux-flux correlation of the first case, with pre-existing background electron population. (left) Light curves at 5 different energy bands, on 700 seconds bins. Light curves are normalized to their peak values. In the bottom panel we show two X-ray energy bands, and in blue the *RossiXTE*/PCA 2–4 keV data. The top panel comprises the simulated TeV band light curve, to be compared with the blue data points, as well as light curves in optical and a band representative of the *Fermi*/LAT bandpass. The grey shaded area is intended to highlight the initial section of the light curve which is not meaningful because it corresponds to the interval during which the pre-existing electron population is being 'prepared'. The long dashed vertical grey lines mark the injection period. The dotted red line marks the time corresponding to the largest cross-section of the active region along planes of equal observed times (see text, § 3.2.7). The colored short thick segments mark the times corresponding to the SEDs plotted in Fig. 3.1. (right) The flux vs. flux plot for X-ray and γ-rays. Simulations data have been smoothed with a one-hour width boxcar filter. Colors highlight different 10 ks time intervals. As labeled, red starts at t=30 ks. For the red and blue lines we used a thicker trait to highlight the central time interval of the outburst. The magenta points connected by a dotted line show the observed correlation of TeV flux in Crab units vs. X-ray in count rate for the 2001 March 19 flare. Because of the different units they are plotted at an arbitrary position.

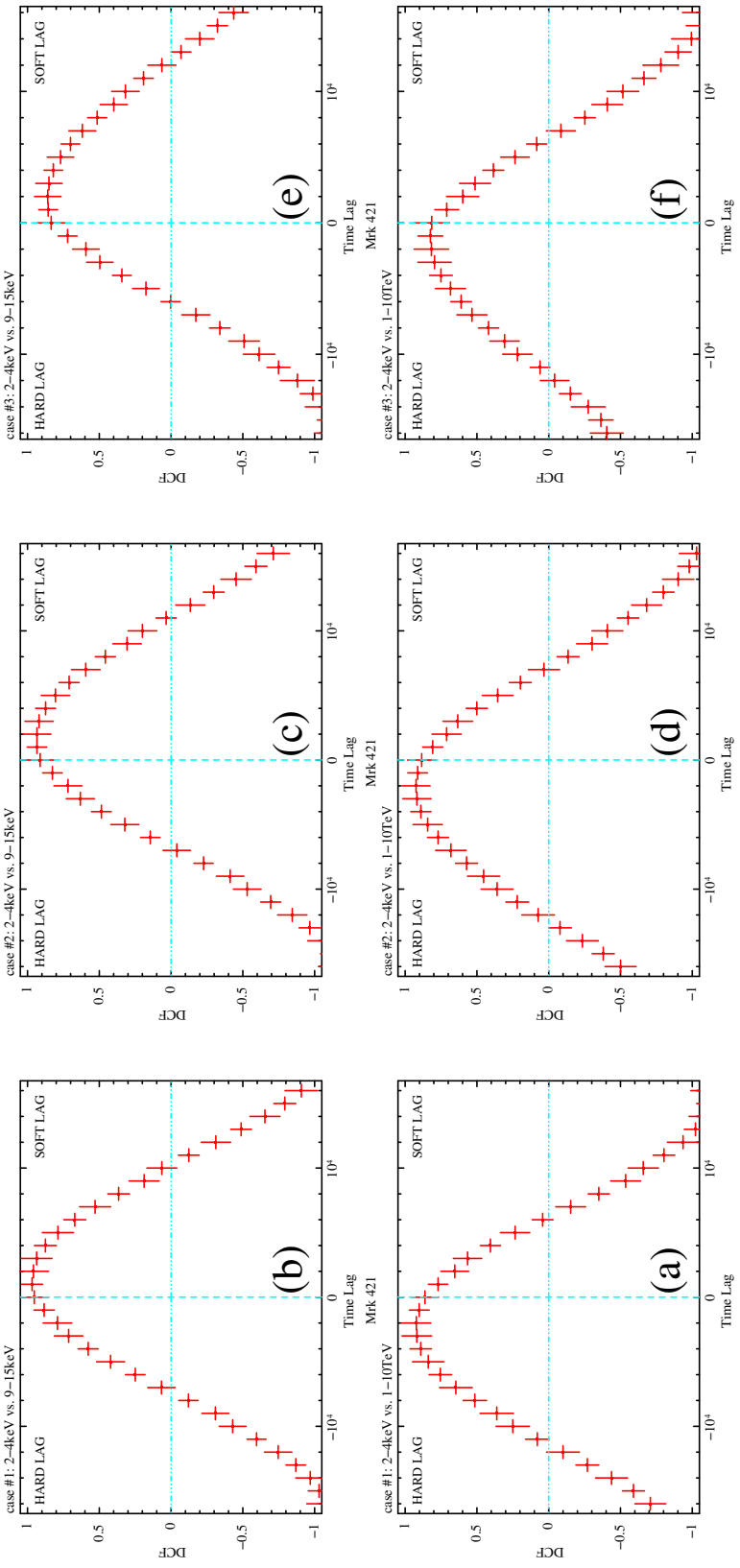

Figure 3.3 : Discrete cross correlations analysis. Our simulated cases run left to right, (a, b) for the 'background' case, (c, d) for the 'foreground' case, (e, f) for the 'better TeV spectrum' case. Top panels show the intra-band X-ray correlation between X-ray ($2-4$ keV) and X-ray ($9-15$ keV), and bottom panels the inter-band correlation between soft(er) X-ray ($2-4$ keV) and TeV γ-rays.

3.2.4 Case 1: injection in a blob with a pre-existing (background) electron population

In all cases presented in this chapter, the outburst is attributed to the injection into our active volume of a new population of higher energy electrons, with fixed injected spectrum (power law with exponential cutoff).

In this first scenario the blob is not empty, but it is filled with a 'background' population of electrons, homogeneous throughout the volume. These electrons serve as a slowly evolving component in the electron distribution and in turn the SED, which can be regarded as the remnants of a previous phase of activity. They participate fully in the time evolution of the blob, cooling and emitting radiation.

The overall best case has the following parameters: $R = 10^{16}\,\mathrm{cm}$, $Z = 4/3 \times 10^{16}\,\mathrm{cm}$, $B = 0.1\,\mathrm{G}$, $\Gamma = 33$. Parameters for this and all following cases are summarized in Table 3.1.

At $t = 0$ the electron spectrum for the 'background' population is a broken power law distribution:

$$N(\gamma) = N_{\mathrm{b}} \left(\frac{\gamma}{\gamma_{\mathrm{b}}}\right)^{-p_1} \qquad \mathrm{cm}^{-3} \qquad \gamma_{\mathrm{min}} < \gamma < \gamma_{\mathrm{b}}$$

$$N(\gamma) = N_{\mathrm{b}} \left(\frac{\gamma}{\gamma_{\mathrm{b}}}\right)^{-p_2} e^{-\gamma/\gamma_{\mathrm{max}}} \qquad \mathrm{cm}^{-3} \qquad \gamma_{\mathrm{b}} \leq \gamma$$

The spectral indices are $p_1 = 1.5$ and $p_2 = 2.5$. The break is at $\gamma_{\mathrm{b}} = 2 \times 10^4$, the high-energy cut-off at $\gamma_{\mathrm{max}} = 2 \times 10^5$. The number density of this 'background' population is $n_{\mathrm{e}} = 4\,\mathrm{cm}^{-3}$. Their total energy content is $2.2 \times 10^{46}\,\mathrm{ergs}$.

By the time when the new flare begins, i.e. the shock begins to cross the region and inject electrons, this pre-existing population has cooled to a γ_{max} of a few times 10^4, yielding a synchrotron peak at around 50 eV. In the observer's frame, the cooling time-scale for the peak of the 'background' component is of the order of 1 day and we

could think of it as due to the aging of the electron spectrum from a previous active phase occurred a few days earlier. In most recent long observing campaigns Mrk 421 exhibited flares on about this time-scale (e.g. Takahashi et al., 2000).

The injection of electrons begins at $t'_{\rm start,inj} = 5 \times 10^5\,{\rm s}$, with a power law distribution (§2.6.2). The parameters of the injected spectrum are: $p = 1.5$, $\gamma_{\rm min} = 50$, $\gamma_{\rm max} = 1.9 \times 10^5$, $L'_{\rm inj} = 5.5 \times 10^{40}\,{\rm erg/s}$.

The emitted –beamed– photons are integrated over the angle of $0.99944 < \cos(\theta) < 0.99964$, which corresponds to a Doppler factor of $27 < \delta < 42$.

Results

In Fig. 3.1 & 3.2 we show a summary of the main comparisons with observations, as SEDs, light curves and flux-flux correlation. The broadband SEDs at 3 different times are shown in Fig. 3.1(left), with X-ray and TeV γ-ray spectra for 2001 March 19 and historical multiwavelength (from radio to TeV) data points. Corresponding SEDs zoomed around the X-ray band are shown in Fig. 3.1(right). Light curves for 5 relevant energy bands are plotted in Fig. 3.2(left), while the fluxes in the X-ray and TeV γ-ray bands are plotted against each other in Fig. 3.2(right). About the light curves, it is important to note that the evolution during the first 15 kilo-seconds ($= t'_{\rm start,inj}/\delta$) of simulation (highlighted with grey shading) simply reflects the initial setup of the pre-existing background electron population, reaching its (approximately) steady radiative state as the blob fills with the radiation from all the zones, and radiation begins to escape.

In Figures 3.3a,b we show the Discrete Correlation Function (DCF Edelson & Krolik, 1988) computed between the light curves in two X-ray bands ($2-4$ and $9-15\,{\rm keV}$) and X-ray and TeV ($2-4\,{\rm keV}$ and $> 1\,{\rm TeV}$). They are shown for illustrative purposes,

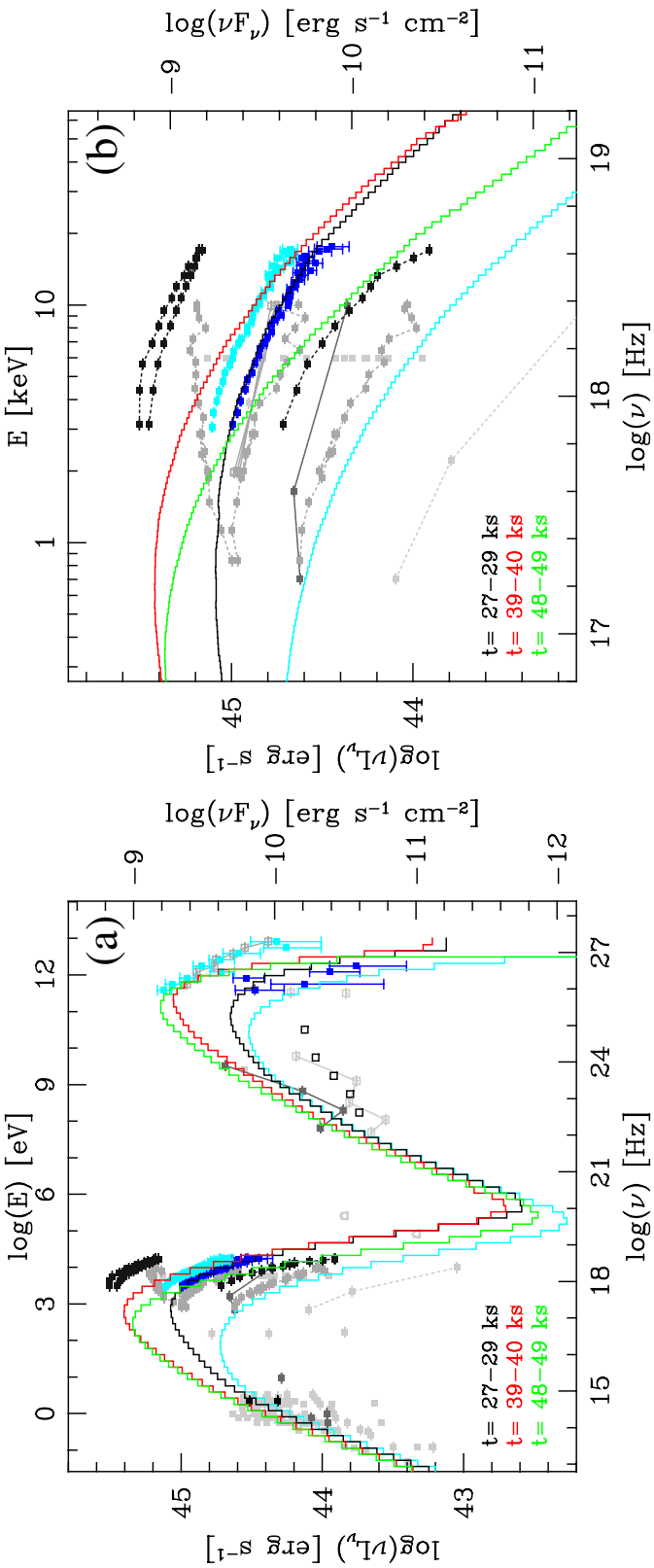

Figure 3.4 : SED of the second case (empty blob, with foreground emission). All panels, colors, symbols are the same as those used in Fig. 3.1, with the addition of a cyan SED representing the 'foreground' component.

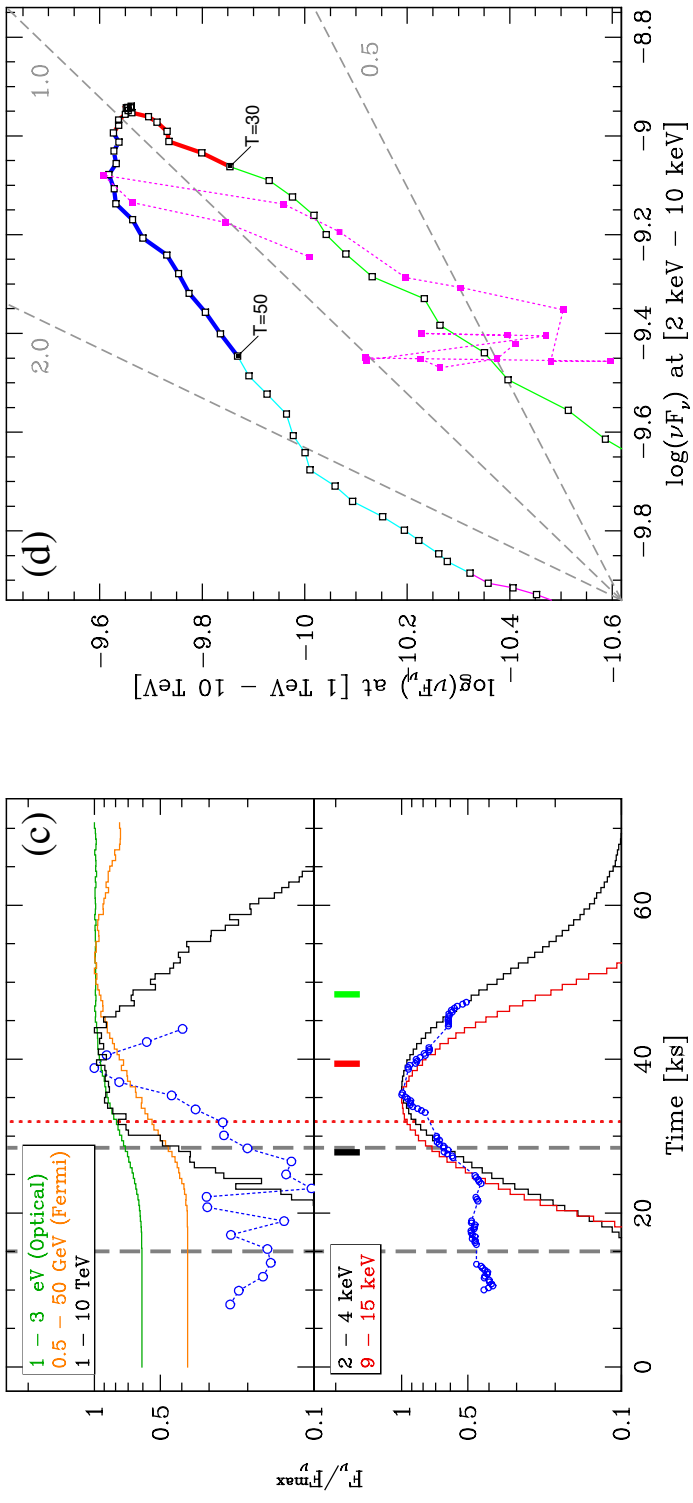

Figure 3.5 : Light curves and flux-flux correlation of the second case (empty blob, with foreground emission). All panels, colors, symbols are the same as those used in Fig. 3.2. In this case there is no preliminary phase to prepare the active region.

and no extensive statistical analysis has been performed to assess the uncertainty on the lag value.

In the framework of the observational issues outlined in Section 3.2, we note that:

1. The flare light curves are approximately symmetric for both the X-ray bands as well as for the TeV γ-rays. The GeV γ-ray light curve asymmetry reflects the relative duration of the light crossing times and of the cooling time-scales of the electrons emitting the seed photons and doing the IC scattering. For photons emitted by electrons (and seed photons) varying on a time-scale shorter than the geometric one this latter dominates the flare profile, hence making it symmetric. For bands whose emission processes are characterized by physical time-scales longer than the geometric ones, the –slower– cooling decay profile emerges.

2. The amplitude correlation between X-ray and γ-ray fluxes is quadratic, i.e. $F_\gamma/F_{\gamma,0} \sim (F_{\rm X}/F_{\rm X,0})^\eta$ with $\eta \simeq 2$, during the rise of the flare. Shortly after the peak the trend flattens, becoming linear. At this point the March 19 light curves were still showing a quadratic correlation, which lasted until the end of the TeV (Whipple) observational coverage (see magenta points in Fig. 3.2).

3. A soft lag is clearly discernible between the different X-ray bands, while a similarly short hard lag is present between the γ-ray and the softer X-ray band (see also Figures 3.3a,b). In the 2001 March 19 flare a short hard lag was observed in both cases (Fossati et al., 2008). We will discuss a possible important factor responsible for the soft intra-band X-ray lags and the role played by geometry and LTTE later, in Section 3.2.7.

4. Since the active region was previously filled by a population of electrons emitting a lower luminosity slowly varying SED this scenario easily accounts for the

modest variability in the optical band.

5. While matching the observed X-ray spectra is relatively easy, for the γ-ray spectrum we encountered the usual challenge: the observed γ-ray spectrum is harder than what predicted by simulations (Fossati et al., 2000b; Błażejowski et al., 2005).

In order to investigate these points in more details, we explored two alternative scenarios, which we discuss in turn below.

3.2.5 Case 2: injection in empty blob, with emission diluted by a separate steady component (foreground)

With a similar setup we tested a scenario in which there is no background electron population pre-existing in the blob. The steady broader band emission observed in the optical band is attributed to a component from a different region in the jet, which we will call 'foreground' component. We assume that there is no interaction between the two regions. The 'foreground' component is combined a posteriori with the radiation from the flaring blob, simply by adding it as a steady SED to the emission from the time dependent simulation. A very important difference with respect to the previous case is that photons from this component do not contribute to the IC emission by the freshly injected electron population.

The volume size, geometry and Doppler factor of the active blob are the same as for the previous case.

Because of the lack of extra local seed photons for the IC emission, in order to match the SED, in particular to boost the IC component with respect to the synchrotron one, it is necessary to decrease the magnetic field strength.

The injection of electrons begins at $t'_{\rm start,inj} = 5 \times 10^5\,{\rm s}$. The injected distribution has a spectrum with $p = 1.5$, $\gamma_{\rm min} = 50$, $\gamma_{\rm max} = 1.9 \times 10^5$, $L'_{\rm inj} = 6 \times 10^{40}\,{\rm erg/s}$.

The foreground component is simulated with the same code, run separately. For convenience, its electrons are assumed to be in similar geometric and magnetic environment to the active region. They have a broken power law distribution, with spectral indices $p_1 = 1.5$ and $p_2 = 2.5$. The break is at $\gamma_{\rm b} = 10^4$, the high-energy cut-off at $\gamma_{\rm max} = 10^5$. The electron density is $n_{\rm e} = 6\,{\rm cm}^{-3}$ (total energy content is $2.3 \times 10^{46}\,{\rm ergs}$). These parameters for the putative 'foreground' emission are such that its time evolution is modest on the time-scales in which we are interested here.

Results

The resulting SEDs, light curves, and the X-ray vs. TeV flux-flux correlation are shown in Fig. 3.4a-d, the DCFs in Fig. 3.3c,d. This scenario does not reproduce the main features of the reference observations better than the first one.

1. The flare is asymmetric in TeV γ-rays and in the softer X-ray band. It remains symmetric for harder X-rays.

   The relative length of cooling and geometric time-scales is again an important factor, cleanly shown by the X-ray bands. In TeV γ-rays however this is compounded by the effect of LTTEs. The first steeper rise (up to $t = 30\,{\rm ks}$) of TeV flux is driven by the increase of electrons as they are injected in the blob by the moving shock combined with the fact that we see a larger and larger fraction of the blob volume, modulated by external LTTE (see § 3.2.7). This is also signaled by the fact that the knee occurs at around the time when the observer would see the largest section of the blob (red dotted line in Fig. 3.5c). The slow rising, flat-top, phase ($30 - 45\,{\rm ks}$) of the TeV light curve is due to the increase

of seed photons available at each location within the blob due to diffusion from the rest of the blob, delayed by internal LTTE. It's a slow rise also because the high energy electrons responsible for most of the IC scattering to the TeV band are already cooling rapidly. At some point the radiation energy density in each location in the blob will stop increasing because enough time has passed for photons to diffuse throughout the blob. After that time the evolution is simply determined by particle cooling and external LTTE. Because the electrons emitting the bulk of the observed TeV flux have a cooling time larger than R/c, in this case the TeV flare decay shape is determined by cooling rather than LTTE.

2. As in case 1, the flux-flux amplitude correlation is reproduced only partially. The trend is almost quadratic during the rising phase of the flare, and it turns to sub-linear on the decaying phase, after a short horizontal shift corresponding to the flat top of the TeV light curve.

3. The path of the flux–flux diagram signals the presence of a time lag between the soft X-ray and the TeV γ-ray emission, which is shown in the DCF (Fig. 3.3d). The TeV γ-ray lags the 2-4 keV soft X-ray by about 2 kilo-seconds, comparable to the observation of the March 19 flare as in the first scenario. Also similar to case 1 is the soft lag between the two X-ray bands, opposite to what observed on 2001 March 19.

4. For what concerns the optical band, since we designed also this second scenario to address directly its minimal variability, it is not surprising that the light curve exhibits only a modest variation.

5. Finally, also in this scenario we have not been able to produce TeV γ-ray spectra as hard as the observations and in the end we limited ourselves to matching the

flux level at around 1 TeV.

Some of the differences with respect to the first case are ultimately due to the weaker magnetic field making synchrotron cooling time-scales $\sim 60\%$ longer: for the highest energy electrons emitting in X-ray and TeV $\tau'_{\rm cool}$ becomes longer than R/c. It is worth emphasizing that the decrease of B is dictated by observational constraints, namely the relative luminosity of the synchrotron and IC components and the need to compensate for the absence of the additional source of seed photons for IC scattering provided in case 1 by the co-located 'background' component. This is in fact a good example of how the model is globally constrained.

3.2.6 Case 3: with pre-existing electron population, adjusted to better match the TeV spectrum

As we pointed out, in the previous two cases, the simulated SED in the TeV γ-ray range is softer than the observed spectra. To try to improve the match of the TeV part of the SED, we considered a modified version of the first scenario. We increased the Lorentz factor ($\Gamma \simeq 46$) and decreased the magnetic field strength ($B = 0.035\,{\rm G}$), the goal being to move the inverse Compton peak to higher energy while leaving the synchrotron peak approximately unchanged. The parameters are: $R = 1.5 \times 10^{16}\,{\rm cm}$, $Z = 2 \times 10^{16}\,{\rm cm}$, $B = 0.035\,{\rm G}$, $\Gamma = 46$. At $t = 0$ the 'background' electrons have the same broken power law distribution as in the first case, but with lower number density, $n_{\rm e} = 1.56\,{\rm cm}^{-3}$. The volume is slightly larger yielding a total energy content of $2.9 \times 10^{46}\,{\rm ergs}$.

The injected electrons have a power law distribution with $p = 1.5$, $\gamma_{\rm min} = 50$, $\gamma_{\rm max} = 1.9 \times 10^5$, $L'_{\rm inj} = 3.2 \times 10^{40}\,{\rm erg/s}$. Injections starts in this case at $t'_{\rm start,inj} = 8 \times 10^5\,{\rm s}$.

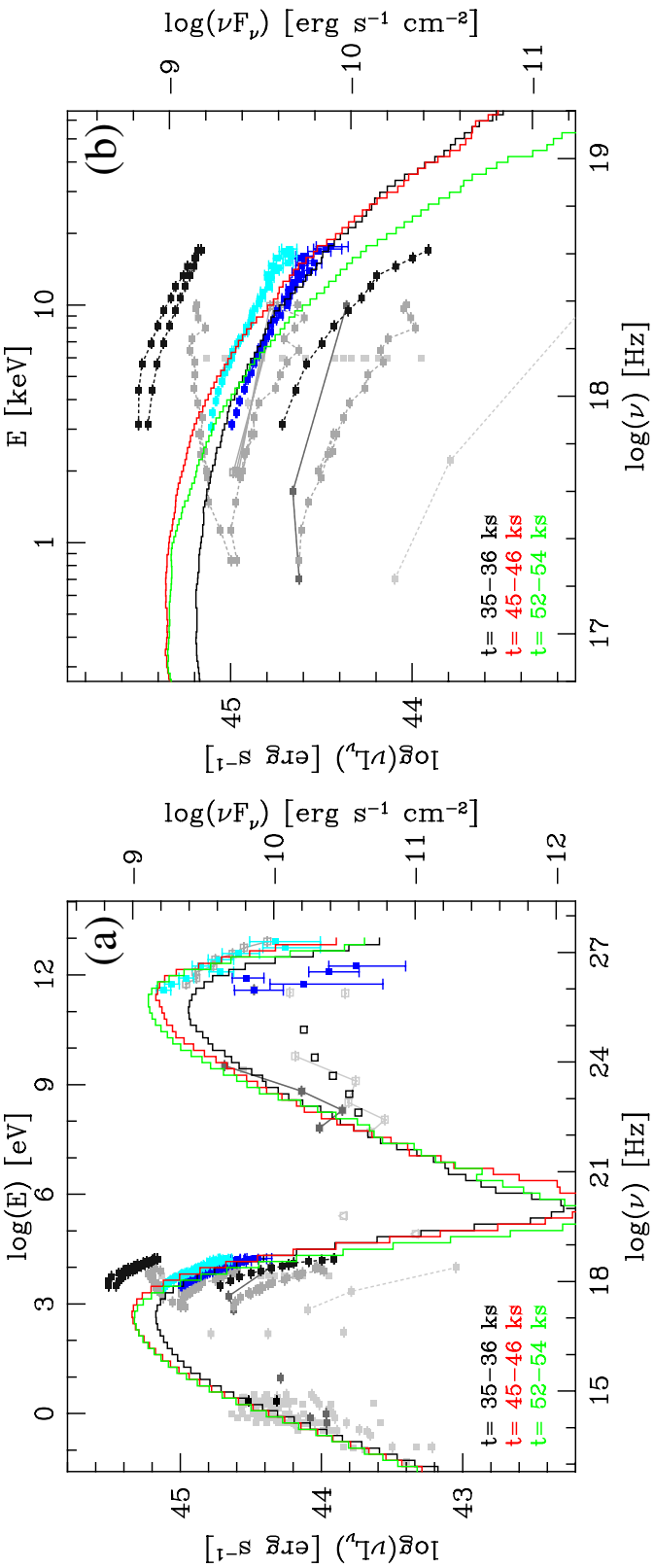

Figure 3.6 : SED of the case 3 (blob with pre-existing background electron population, with parameters adjusted to better match the TeV spectrum.) All panels, colors, symbols are the same as those used in Fig. 3.1.

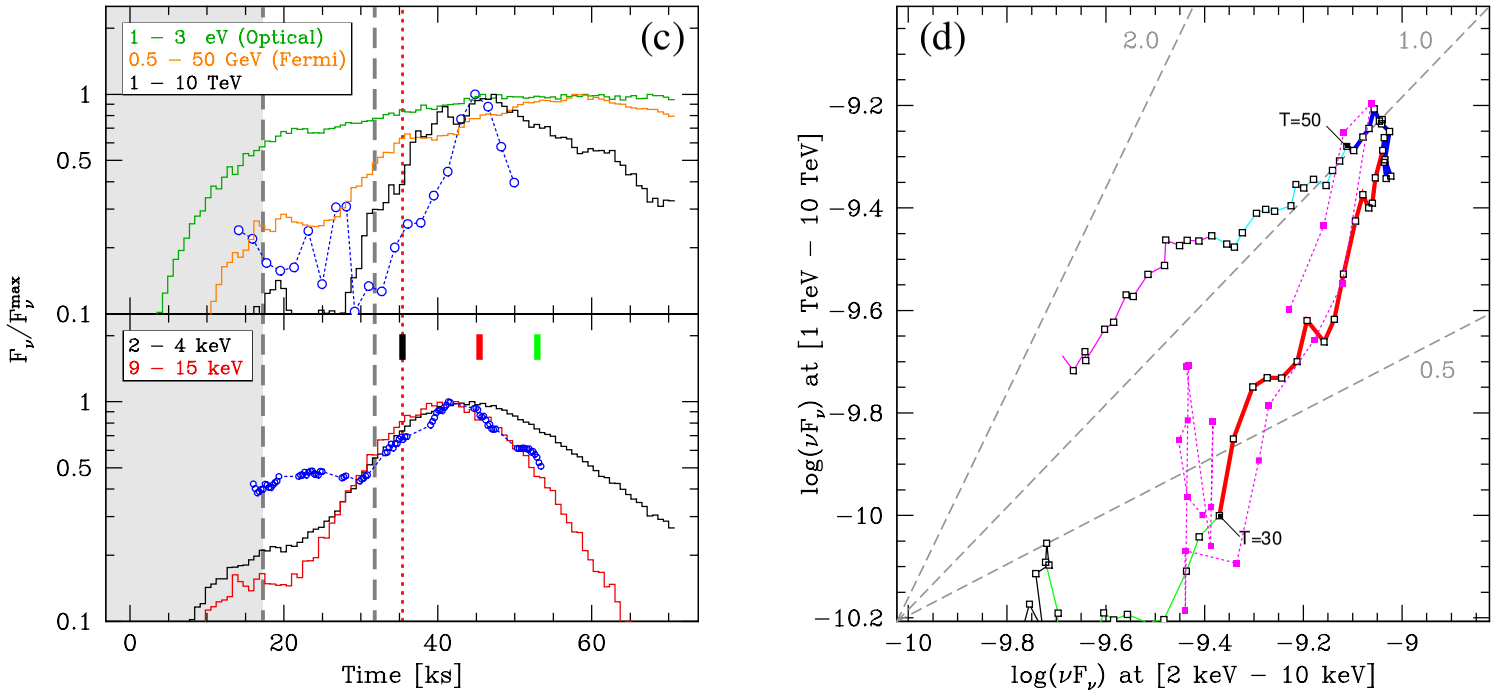

Figure 3.7 : Light curves and flux-flux correlation of the case 3 (blob with pre-existing background electron population, with parameters adjusted to better match the TeV spectrum.) All panels, colors, symbols are the same as those used in Fig. 3.1.

Results are integrated over $0.99971 < \cos(\theta) < 0.99981$, which corresponds to a Doppler factor range $37 < \delta < 57$.

Results

SEDs, light curves, and X-ray vs. TeV flux-flux correlation are shown in Fig. 3.6, and DCFs in Fig. 3.3e,f. The itemized summary of the main reference observations does not show improvements beyond the slightly higher VHE SED peak.

1. Because of the larger Doppler factor the electron emitting at the SED peaks have lower energy, which combined with a weaker magnetic field results in longer cooling time-scales (see eq. 3.3), in turn exceeding the source crossing time. This has the effect of increasing the asymmetry of the light curves in bands whose emission involves lower energy electrons and/or photons. The soft X-ray and TeV γ-ray light curves indeed have a slowly decaying tail.

2. Once again during the rising phase of the flare the γ-ray-X-ray correlation is approximately quadratic, until the peak of the X-ray light curve. After the TeV flare peak the correlation is approximately linear, as expected when the variation in both bands is driven only by the cooling of the (same) electrons, because the IC seed photons are emitted by particles with longer cooling time-scale.

3. The results concerning time-lags are equivalent to those of the other scenarios, perhaps with a hint of a smaller lag between TeV and softer X-ray. More extensive analysis would be necessary to quantify this possibility.

4. The slight shift of the IC peak to higher energy enables a better match with the observed spectra, although the actual spectral indices of the simulated SEDs

remain softer than the observed values.

Further increases of the Doppler factor can still produce good SEDs, as long as we concurrently reduce the size of the volume. However, the light crossing time would rapidly become smaller than the observed flare duration, and it would have minimal impact on the observed phenomenology. Therefore the observed flare shapes must represent the true acceleration and cooling of the electrons, and the symmetry of the light curves must be caused by similar heating (or injection) and cooling time-scales.

3.2.7 Geometric Effects on Light Curves

There are complex geometry-related effects that have an impact not only on the shape of the observed light curve (e.g. its symmetry), but can also leave an imprint on other observables such as time lags and energy-dependent flare shape. Depending on how the particle injection and acceleration processes are distributed spatially, differences in physical time-scales for particles of different energy effectively may add a further geometric effect by inducing inhomogeneities (e.g. stratification) in the source.

We would like to illustrate with an extremely simple toy-model some aspects of the role of the geometry of the emitting region, and its interplay with some of the intrinsic physical time-scales. This analysis was indeed motivated by the observation, at first surprising, that the peaks of the simulated X-ray light curves did not correspond to either the time when the shock exits the active region and injection is not present anywhere anymore, or to the time corresponding to the largest cross-section of the cylindrical volume along planes of equal observed times. In Figures 3.2(left), 3.5c, 3.7c, these two times are marked as the second dashed grey line and the red-dotted line, respectively. Moreover, the shift changes with the light curve energy band as noticeable in the case of X-ray light curves.

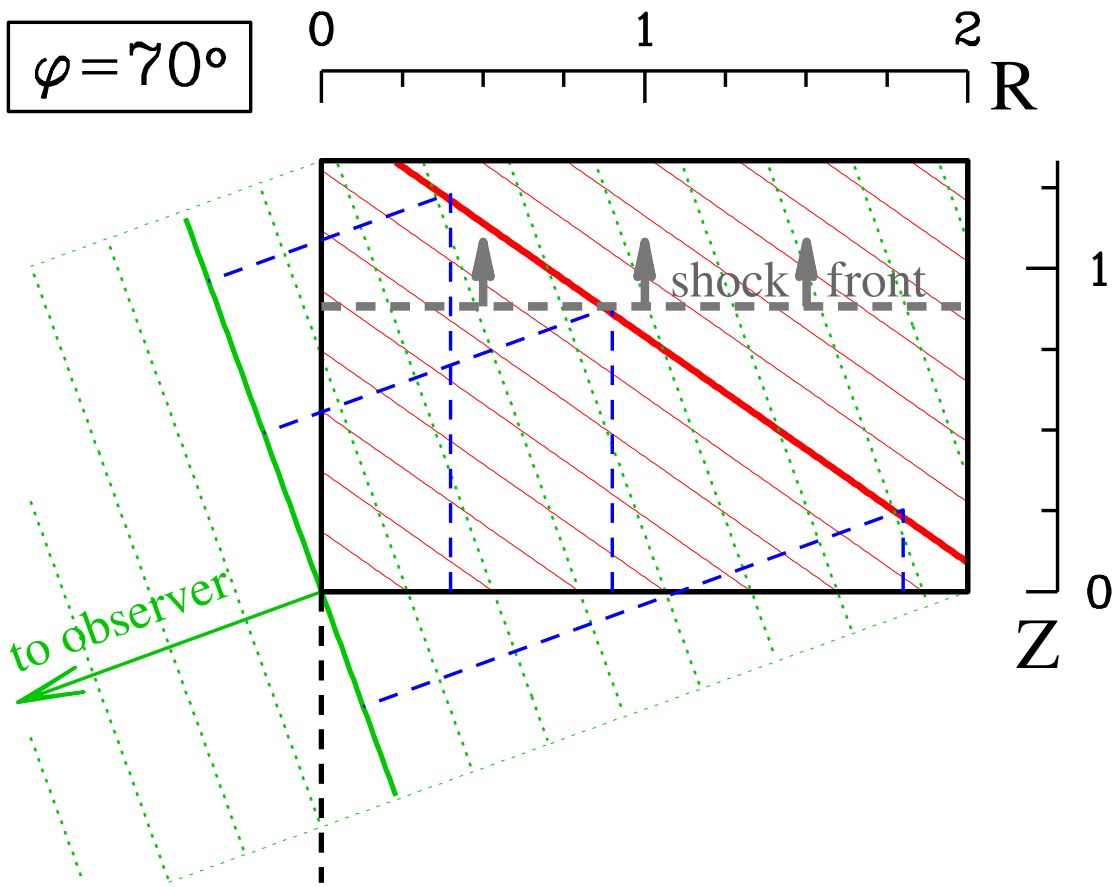

Figure 3.8 : Diagram illustrating the geometry of the toy-model (see text, § 3.2.7). The black rectangle represents a side 2D view of the cylinder, with $R = 1$ and $Z = 4/3$ (same aspect ratio of our simulations). The grey dashed line represents the 'shock front' traveling at the speed of light through the cylinder, along its axis of symmetry, in the direction marked by the arrows. The green arrow represents the direction to the observer, while the green lines (solid and dotted) are planes perpendicular to the line of sight. In this example the viewing angle is $\varphi = 70°$. The red lines represent the loci of points whose photons reach the observer simultaneously, taking into account the 'shock' travel distance/time until of their activation and the light travel time to the observer since that moment. The blue dashed lines illustrate this by showing three paths of equal length from the beginning of the 'flare'. The red loci form an angle $90° - \varphi/2$ with the line of sight or, equivalently, an angle $\varphi/2$ with the front face of the volume.

To verify the hypothesis that the time shifts are caused by the different size of the observable regions filled with electrons contributing most of the emission at those frequencies, we consider a purely geometrical model solely based on the 'appearance' of slices of different thickness through a cylinder.

Like in our real blob model, a shock is traveling along the axis of symmetry of the cylinder turning 'on' a thin local slice. Each point of this slice stays 'on' for a limited time, $\tau_{\rm on}$. We do not consider a variation of brightness with time, just an on/off state. We build light curves where 'flux' is simply the size of the volume that is seen 'on' by the observer at any given time. The 'on' volume visible at each time from the observer point of view is computed taking into account light travel times and it cuts through the cylinder along planes yielding constant arrival time to the observer. For an observer viewing the cylinder at an angle φ with respect to its axis, the loci of points whose photons he sees simultaneously are planes with an inclination $\varphi/2$ with respect to the face of the cylinder ($90^\circ - \varphi/2$ with respect to the cylinder axis). Figure 3.8 shows a 2D schematic of the geometry of the problem.

If the cylinder was moving with Lorentz factor Γ, because of relativistic aberration at a viewing angle $\theta \simeq 1/\Gamma$ we would be observing the radiation that in the comoving frame leaves the cylinder 'sideways', at 90° from its axis. The observed frequencies would be blue-shifted and times compressed, but that would be simply a scaling factor applied uniformly to them and for convenience we can chose to use observed frequencies and times. Therefore observing the toy-model at $\varphi = 90^\circ$ is equivalent to observing the relativistically moving blob at $\theta = 1/\Gamma$, and in turn this purely geometrical analysis captures some of the features of the realistic model studied in this chapter.

The results are illustrated in Figure 3.9. In the first panel, we show the general

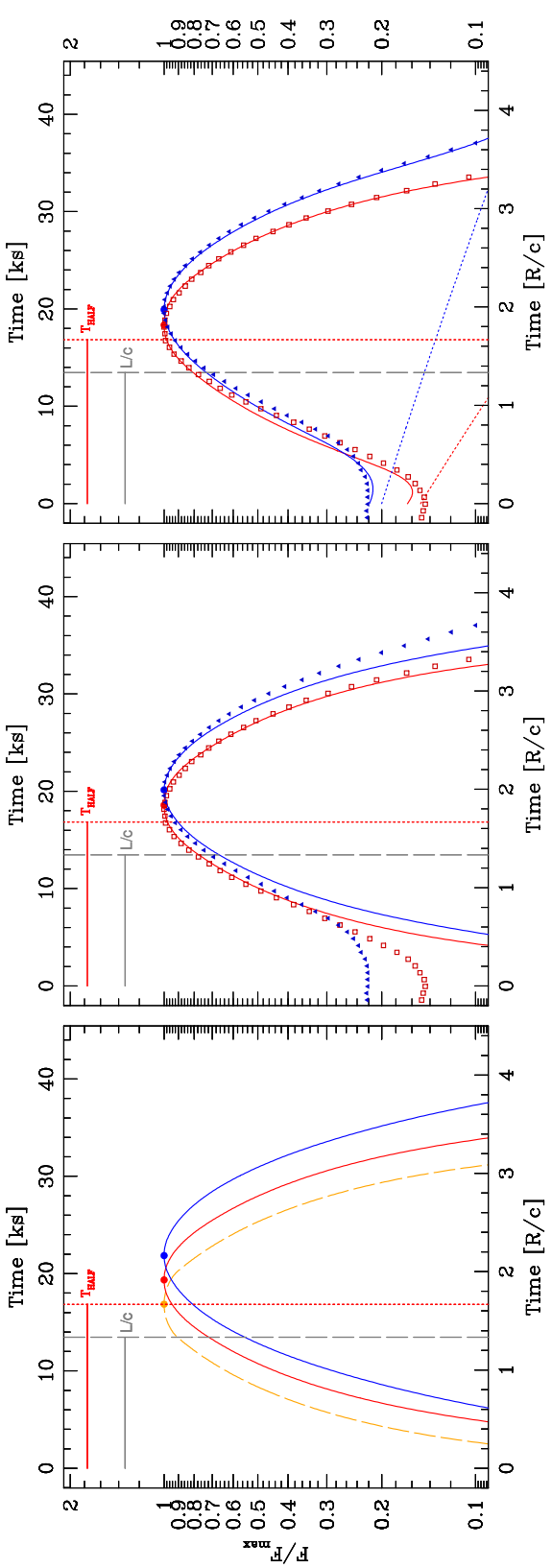

Figure 3.9 : Light curves for a purely geometrical toy-model of the observations of a cylinder seen at an angle $\varphi = 90°$ with respect to its axis. The meaning of the vertical lines is the same as in Fig. 3.2c, 3.5c, 3.7c, except that since the 'injection' begins at $t = 0$, there is no first grey dashed line. (a) Three cases illustrating the time shift caused by the simple variation of $\tau_{\rm on}$. The (light) curves are computed for $\tau_{\rm on} = 10^{-3}$ (orange), 0.5 (red), 1.0 (blue), in units of R/c. The orange case, with a $\tau_{\rm on}$ value yielding a negligible slice thickness, peaks at the expected time. (b) Attempt at matching light curves and simulation data without any baseline component contribution. The red curve is computed for $\tau_{\rm on} = 0.35$, the blue for $\tau_{\rm on} = 0.65$. The symbols are the simulated light curves of case 1, shown in Fig. 3.2c: red empty squares for 9−15 keV and blue triangles for 2−4 keV. (c) Same flare light curves combined with a slowly decaying baseline, with time-scale proportional to $\tau_{\rm on}$.

features of the light curves obtained with this model, most importantly the effect of the change in the duration $\tau_{\rm on}$. In Figure 3.9a we plot the curves for three cases, showing the shift of the flare peak to later time as $\tau_{\rm on}$ increases. For very short $\tau_{\rm on}$ the maximum is reached at the expected time, that is when size of the plane that is the locus of points simultaneously seen by the observer (red lines in Fig. 3.8) is the largest possible for the given viewing angle. In general, however, the light curve peak will be shifted by $\Delta t = \tau_{\rm on}/2$. There is also a widening of the light curve, though much less noticeable than the peak shift. It is worth noting that at this extreme level of simplification geometric effects can not produce any asymmetry in the light curves.

We tried to reproduce with this toy-model the X-ray light curves from the simulations of the first scenario presented here. The results are shown in Figure 3.9b,c. The central panel shows the curves obtained by adjusting $\tau_{\rm on}$ to match the peak time of the two X-ray light curves (plotted with symbols), yielding a very satisfactory result for values around 0.35 and 0.65 R/c. However the overall shape of the flares can not be matched well without adding a baseline component, to mimic in some way the fact that in the simulations the blob was already 'on' at a low level prior to the beginning of the injection. We therefore added to the toy-model light curves a slowly decaying component, with an initial level such that the combination of the two components would match the data. Since in the simulations the pre-existing component is left to evolve (cool) starting at the beginning of the active phase, here we let the baseline component decay too. The visual matching is not critically sensitive to the exact values of the decay slopes, and to make the model more constrained we forced them to be in a fixed ratio with respect to the chosen $\tau_{\rm on}$, by considering that the cooling times of the electrons emitting the baseline photons are also related to their energies. For the results shown in Figure 3.9c the slope is equal to five times $\tau_{\rm on}$ for both cases.

The synchrotron cooling time-scale for electrons emitting in the $2-4\,\mathrm{keV}$ and $9-15\,\mathrm{keV}$ bands, following the approximate expression of eq. 3.3 are $\tau_{\mathrm{soft}} \simeq 0.73 - 1.04\,R/c$, $\tau_{\mathrm{hard}} \simeq 0.38 - 0.5\,R/c$. Given the steepness of the X-ray spectrum the emission in each band is dominated by the lower energy electrons, hence the longer τ is probably a more appropriate estimate. On the other hand, the above cooling time-scales only consider synchrotron cooling. Including some additional loss due to IC would decrease the value of τ. In any case, the similarity between these crude estimates of cooling time-scales and the values of τ_{on} corroborates the success of the geometrical toy-model at fitting the simulation light curves.

The ability of the purely geometrical toy-model to reproduce the two X-ray light curves is indeed remarkable. For X-rays this is facilitated by the fact that the synchrotron emission is independent on the internal delays due to photon diffusion that affect the evolution of the IC emission from the blob. It is not possible to apply a similar toy-model to the γ-ray light curves.

It is worth noting that although this test shows how dominant the effect of the geometry can be in shaping the light curve, at the same time we need to highlight that some geometry parameters, such as the 'thickness' of the visible slices, are in effect determined by the physical conditions of the emission region.

In this respect it is interesting to note that, at least in the setup of the scenarios presented in this work, despite the apparent dominance of the source geometry the effect of the energy dependent physics-induced geometrical factors is detectable. Hence multiwavelength datasets and time-resolved spectroscopy have the potential to disentangle them from the source geometry.

3.3 Discussion

Using the MC/FP code, we presented three test scenarios, aimed at modeling the variability exhibited by Mrk 421 during the 2001 March 19 flare, and based on a relatively standard choice of parameters. The results of these tests are summarized in Table 3.2, side by side with the features observed in the actual multiwavelength observations (Fossati et al., 2008). There are a few fundamental issues that we wanted to address, which are common throughout the phenomenology of all well studied blue blazars.

1. The shape of the flares, often quasi-symmetric for a wide range of observational bands where the intensity variations are large (the main ones being X-ray and γ-ray).

2. The characteristics of the correlation between X-ray and γ-ray fluxes. There has been great interest in the slope of their relationship, in particular because of the observation of a quadratic, or higher order, relationship holding throughout some well sampled outbursts, challenging our understanding of the physical conditions and causes of the variability.

3. The phase of the correlation between variations in different bands, namely the existence of time lags and their duration.

None of the three test scenarios was able to reproduce all the characteristics of the 2001 March 19 flare. Two features have been particularly challenging to match: the relationship between X-ray and TeV γ-ray fluxes on the decay phase of the flare, and the intra-band X-ray time lag. Moreover, the shape (symmetry) of the flare light curves could be reproduced only by one of the three scenarios, case 1.

These aspects of phenomenology are among those more affected by the spatial extent and geometry of the source, whose influence varies with observed energy band because of the relative importance of geometrical and physical time-scales. The impact of the geometrical factor, both due to the source intrinsic structure and to the stratification of properties due to the physical processes, emphasizes the necessity of a code like the one we introduce here for modeling the variable high energy emission from blazar jets.

The difficulty of producing a quadratic relationship between the fluxes in the X-ray and γ-ray during the declining phase of the flare may indicate that pure radiative cooling cannot fully explain the electron cooling mechanism. The delayed evolution of the seed photon field due to internal LTTE compounds the problem. One alternative possibility could be a process causing energy loss over a wide range of electrons energies (such that the IC seed photons are also affected) on very similar/same time-scale, such as adiabatic cooling, which could be associated with expansion of the blob, or particle escape. They are often invoked in qualitative discussions and in the context of simpler models, treated by means of some phenomenological prescription. The addition of such mechanisms to the code in a proper astrophysical way is not immediate, but we are working on its implementation. The escape term present in the Fokker-Planck equation is actually neglected for these set of simulations. In a follow up work including particle acceleration and escape, this latter seems to be effective and we obtain a quadratic flux relationship and hard lags (see Chap. 4). About the effect of adiabatic expansion of the emitting blob, based on the simplified analysis of Katarzyński et al. (2005), Aharonian et al. (2009), argue against its viability once the implications of this expansion on the magnetic field and particle cooling are taken into account. Nevertheless, its effect should be assessed with actual time-dependent

simulations of a source of finite size.

As to the hard intra-band X-ray lags, in Section 3.2.7 by means of a toy-model we illustrated an important factor affecting observations of time-lags: source 'stratification' combined with LTTE induces a systematic soft lag. The simulations presented in this work do not include an acceleration term, hence the lack of hard lags is not a complete surprise. Nevertheless, the induced systematic geometric soft lag introduces an additional constraint on viable electron acceleration and injection scenarios. In this respect, the results of the above mentioned study focused on X-ray lags (Chap. 4) suggest that continuous acceleration, spatially extended (e.g. diffuse diffusive acceleration due to turbulence, Katarzyński et al., 2006), may be necessary, possibly accompanied by an achromatic energy loss mechanism. It is interesting that this type of scenario seems to be able to produce also a quadratic X-ray/TeV relationship throughout a flare.

One of the most interesting aspects of this analysis was the comparison between two possible hypotheses for the presence of an additional component contributing to the observed SED. The need for two components, a flaring and a quasi-steady one, to interpret some of the observations has become more evident with the improvement of multiwavelength observations (for an interesting decomposition of a Suzaku spectrum of Mrk 421 see Ushio et al., 2009). Disentangling these two components is necessary in order to understand the nature of the transient activity whose properties need to be seen more clearly. This decomposition might also yield information on the average properties of the relativistic jet, for which the less variable component might be more representative.

We considered the two simplest possibilities: i) that the secondary component is due to a population of electrons that exists in the same region that will become active,

Table 3.2 : Summary of simulations results in Chap. 3

Feature	Obs.	Case 1		Case 2		Case 3	
Flare symmetry							
soft X-ray	Y	Y	+	N	−	N	−
hard X-ray	Y	Y	+	Y	+	Y	+
TeV γ-ray	Y	Y	+	N	−	N	−
Flux-Flux Correlation							
trend up	2	2	+	2	+	2	+
trend down	2	1	−	1	−	1	−
Time Lags							
X-ray −X-ray	hard (2 ks)	soft	−	soft	−	soft	−
X-ray −γ-ray	γ-ray (2 ks)	Y	+	Y	+	Y	+

and that will be affected by the flare and evolve with it. This pre-existing component can be interpreted as due to the remnants of a previous outburst. ii) That the secondary component is completely independent from the flare, and it contributes just a steady SED diluting the transient component from the observer point of view. Our simulations offer some hints as to their viability, and they favor the first type of scenario. One fundamental difference between the two alternatives concerns the production of IC emission, i.e. the TeV band. If the observed SED consists of the sum of two independent contributions, emitted by electrons at two different locations then the only seed photons for IC scattering will be those produced by the injected electrons themselves. Starting from an empty blob, the energy density of synchrotron seed photons needs some time to build up, which naturally results in a delay in the variation of the IC scattered γ-rays. This delay is caused by internal LTTE and it turned out to be quite significant as illustrated by the TeV light curve of case 2 (Fig. 3.5c), yielding a flat-top flare not seen in observations. That TeV light curve is in fact an excellent example of LTTEs at work and of the importance of a more advanced modeling code.

Naturally, the cases presented in this chapter only represent an initial study aimed at investigating the importance of LTTE which for the first time could be fully accounted for. These results can not be considered conclusive. Nonetheless, despite their limited scope they make a strong case for a true time-dependent and multi-zone modeling.

The three scenarios discussed can be generally regarded as homogeneous blob scenarios. The magnetic field is the same throughout the simulation volume, and isotropic. For what concerns electrons, the initial setup is homogeneous and the injection is identical in all zones. It is, however, worth emphasizing that during the

evolution of the simulation electrons properties become inhomogeneous because of the different radiative cooling they experience in different zones.

These simulations represent a first order implementation of a class of scenarios for blazar flares often discussed in the literature, envisaging a shock acting on a discrete blob/shell within the jet. We adopted a volume with relatively symmetric aspect ratio, to not depart too much from the sphere 'implied' by one-zone models while making it possible to appreciate the effects of geometry, and attributed the flare to the injection of a fresh electron population.

As discussed in Sections 3.2.1, 3.2.2, and 3.2.3 the main physical parameters are fairly well constrained and the results can be regarded as meaningful for what concerns the time-varying components of the model, as well as the nature of the secondary emission component. The simulations presented in this chapter suggest that a simple injection in the radiating region of particles with a formed spectrum produced in a separate acceleration region whose emission is not significant, does not provide a satisfactory match with some basic observational facts. Moreover, the comparison of the background and foreground component scenarios, in particular with respect to the TeV γ-ray evolution, clearly favoring the first one (case 1), suggests that if a flare is caused by a change affecting the electron population it may be necessary for it to happen on a relatively hot blob, acting on the same particles, re-accelerating them. This in turn would support a scenario where flares are not fully independent of each other but rather occur in the same region.

Chapter 4

X-ray time lags in TeV blazars

4.1 Introduction

One of the defining features of blazars, variability (Ulrich et al., 1997), has been studied intensively in almost all wavelength (Tagliaferri et al., 2008; Fossati et al., 2008; Aharonian et al., 2009; Kataoka et al., 2008; Acciari et al., 2009). According to the positions of their first peaks in the spectral energy distribution(SED), blazars can be divided into blue blazars and red blazars (Fossati et al., 1998). The first peaks of the SEDs of blue blazars are usually identified at a frequency close to X-ray band, where intensive observations have been performed by satellites such as BeppoSAX (Fossati et al., 2000a,b), XMM-Newton(Brinkmann et al., 2003, 2005; Ravasio et al., 2004; Sembay et al., 2002), Suzaku (Sato et al., 2008), ASCA (Takahashi et al., 1996; Kataoka et al., 2000), RossiXTE (Falcone et al., 2004; Rebillot et al., 2006; Fossati et al., 2008; Lichti et al., 2008), and Swift (Tramacere et al., 2009). The variability in this band is very fast, meaning that much information could be obtained with relatively short observations. Additionally, the peak of the high energy SED component of blue blazars is accessible through ground based Cherenkov telescopes. The cross-correlation analysis of the X-ray and γ-ray data makes the observations more fruitful.

As turning points in the SED, the X-ray peak also represents turning points in the energy distributions of the electrons that are producing the SEDs through synchrotron

radiation. This turning point signals a balance between multiple physical processes, such as particle acceleration, cooling and escape. The timing information we obtained around the SED peaks through X-ray observations has provided us a good opportunity to study the evolution of the relativistic electrons, and hence the underlying physical processes.

4.1.1 Observation of X-ray time lags

An important aspect of the temporal analysis of the X-ray involves the correlation of the light curves between soft and hard X-ray. While the soft and hard X-ray light curves are highly correlated, there have been many cases in which a time lag is found between soft and hard bands. The more common case is the soft lag, in which the flare in hard X-ray leads the one in soft X-ray (e.g. Takahashi et al., 1996; Rebillot et al., 2006; Falcone et al., 2004; Kataoka et al., 2000). Hard lag is also not uncommon, (Fossati et al., 2000a; Sato et al., 2008), and has been observed to co-exist with soft lags on the same sources (Brinkmann et al., 2003; Ravasio et al., 2004; Lichti et al., 2008; Tramacere et al., 2009). There have also been multiple occasions in which no significant time lag is observed (Brinkmann et al., 2005; Sembay et al., 2002).

4.1.2 X-ray hard-lags and particle acceleration

The detailed modeling and analysis of the synchrotron time lags have been discussed by Kirk et al. (1998) and Moraitis & Mastichiadis (2011). Their analysis represents the models where a shock external to the emission region is constantly accelerating electrons and injecting them to the radiative region immediate downstream of the shock. In this scenario, the flare and the spectral change can be described as being caused by the change of the shock efficiency, mainly resulted from the variation in the

flow, such as the variation in the flow density, magnetic field amplitude/direction, and turbulence level. Similar argument has also been presented in Garson et al. (2010).

However, there exists another large group of models that do not fit into the scenario described above. In these models what we observe is a moving blob instead of a stationary pattern in a continous flow, and the flares are caused by shocks crossing the emitting blobs, rather than any changes on the shock that is always attached to the emitting downstream region. These models include the internal shock models (e.g. Böttcher & Dermer, 2010; Guetta et al., 2004; Spada et al., 2001; Sokolov et al., 2004) and the standing shock models (e.g. Chiaberge & Ghisellini, 1999; Katarzyński et al., 2008). In the former, two blobs with different velocities collide and the resulting shock waves accelerate particles to high energy; In the later the blob travels through a standing shock with relativistic speed. We will investigate X-ray hard-lags in the standing shock model in this paper. As we will show in §4.4, the crossing shock alone can not produce hard-lags because the blob will be left to cool after the shock leaves the blob. The energy dependence of radiative cooling will alwasy produce soft-lags. In order to understand the observed hard-lags, we will discuss possible roles played by stochastic accelerations that exist through out the blob.

First we consider second order Fermi acceleration. This process, which is caused by particle scattering off turbulence in the plasma, is usually considered to be less efficient than the first order Fermi acceleration, which is caused by particle crossing the shock front (e.g. Vainio & Schlickeiser, 1998). However, since turbulence downstream of the shock exists in much larger space, the second order Fermi process has much longer time available to accelerate the particles. Virtanen & Vainio (2005) used test particle simulation to show that second-order Fermi acceleration in the turbulent downstream may have been underestimated and should have significant effects on the

particle spectra.

Another process that can exist through out the emission region is particle acceleration at shear layers. First discussed by Berezhko (1981), this process involves particles crossing between plasma layers with different speed, and scattering with the local magnetic inhomogeneity. This is also a process that can accelerate particles at high energy (Rieger & Duffy, 2004, 2006). Its existence is independent of shock waves, thus can be much more ubiquitous in the enviroment of relativistic jets, where observationally shock waves have not been directly resolved.

Katarzyński et al. (2006) have discussed stochastic acceleration in the context of TeV blazars. They evaluated the evolution of the electron distribution under the influence of both first order and second order Fermi accelerations which they consider complex enough so that should be treated as stochastic and affecting the whole homogeneous blob. (Tramacere et al., 2011) used several methods to show that stochastic acceleration would lead to an electron distribution that can be described as log-parabolic. They argue that the observed SED of blazars is also log-parabolic, and the curvature of this log-parabolic distribution anticorrelates with the peak energy, consistent with their modeling result. These are viewed as evidence for the existence of stochastic acceleration in blazars.

In this chapter and Chap. 5, we treat all the acceleration processes that exist and work throughout the emission region, including second order Fermi acceleration and shear acceleration, together as stochastic acceleration, and parameterize it in the Fokker-Planck equation using a characteristic time t_{acc}. As for the first order Fermi acceleration, instead of treating it directly, we simply inject the accelerated high energy electrons into the zones in which the shock is located.

By taking advantage of the Monte Carlo code described in Chap. 2, we will

also take into account the Inverse Compton (IC) cooling and light travel time effects(LTTEs), which has not been fully treated in Kirk et al. (1998) or any other earlier models. These effects have been proved to be very important in analyzing the timing information of blazars (Chiaberge & Ghisellini, 1999; Katarzyński et al., 2008; Sokolov et al., 2004; Sokolov & Marscher, 2005), such as the X-ray time lags discussed here.

In §4.2 we will briefly describe the setup of our model. In §4.4 we will show that shock acceleration alone, or stochastic acceleration without particle escape can not produce hard-lags. In §4.5 we present the cases in which we successfully reproduced the multiwavelength variability. We summarize our findings in §4.6.

4.2 Simulations setup

The code we use couples the Fokker-Planck(FP) equation and Monte Carlo(MC) method in a 2 dimensional (cylindrical) geometry (see Fig. 2.2). The electron evolution is governed by the Fokker-Planck equation. Photons are produced, tracked and Compton scattered by the MC part of the code. The cylindrical volume is divided evenly into zones in the radial and vertical directions(r and z coordinates, $n_r = 9, n_z = 30$).

The shock we would frequently refer to is a simplified structure implemented as a discontinuity in electron energy distribution (but not magnetic field, as a simplification in our model) with no thickness (however, our resolution is limited by dz). It is a surface perpendicular to the z direction travelling from the bottom of a cylinder to the top. This shock injects high energy particles into the zones it currently resides in.

4.3 Particle acceleration

The approach we adopt to implement stochastic acceleration is similar to the one used by Katarzyński et al. (2006). The Fokker-Planck equation is simplified to the momentum diffusion equation , when the principle of detailed balance is considered (Blandford & Eichler, 1987).

$$\frac{\partial f(\mathbf{p},t)}{\partial t} = \frac{1}{p^2}\frac{\partial}{\partial p}\left(p^2 D \frac{\partial f(\mathbf{p},t)}{\partial p}\right) \tag{4.1}$$

When we further consider radiative cooling, particle injection and particle escape, and use particle number density $N(\gamma,t)$ for ultra-relativistic particles ($\beta \simeq 1$, i.e. $p \equiv \gamma$) to replace the homogeneous phase-space density $f(\mathbf{p},t)$,

$$N(\gamma,t) = 4\pi p^2 f(\mathbf{p},t), \tag{4.2}$$

the equation is rewritten into*

$$\begin{aligned}\frac{\partial N(\gamma,t)}{\partial t} &= -\frac{\partial}{\partial \gamma}\left[N(\gamma,t)\dot{\gamma}(\gamma,t)\right] \\ &\quad + \frac{\partial}{\partial \gamma}\left[D(\gamma,t)\frac{\partial N(\gamma,t)}{\partial \gamma}\right] + Q(\gamma,t) - \frac{N(\gamma,t)}{t_{esc}}\end{aligned} \tag{4.3}$$

with

$$\dot{\gamma}(\gamma,t) = \dot{\gamma}_{cool}(\gamma,t) + \dot{\gamma}_{acc}(\gamma,t), \tag{4.4}$$

$$\dot{\gamma}_{acc}(\gamma,t) \equiv \frac{2}{\gamma}D(\gamma) = \frac{\gamma}{t_{acc}}, \tag{4.5}$$

$$D(\gamma,t) = \frac{\gamma^2}{2t_{acc}}. \tag{4.6}$$

Here $f(\mathbf{p},t)$ is the isotropic, spatially homogeneous phase-space density, $p = \beta\gamma$ is the dimensionless particle momentum.

*(4.3) here is equivalent to (2.2) in §2.4, if we substitue all the t_{acc} here with $t_{acc}/2$ to define the acceleration and dispersion terms in the latter.

4.4 Difficulty of producing hard-lags

Usually a X-ray soft-lag is expected if we consider only the radiative cooling of relativistic electrons. The higher energy electrons will always cool faster than the lower energy electrons (however, see Georganopoulos et al., 2006), making the soft photon flux always lags the hard photon flux. This is independent of which process causes the rise of the flare. But still, if we want to reproduce the observed X-ray hard-lags, first we need to find an appropriate process that would lead to a hard lag at the rising phase of the flare. One way to achieve this is if a shock is changing its efficiency, thus injecting particles with increasingly higher γ_{max} into the emission zone.

4.4.1 Case 1: shock with increasing efficiency

In the first case, we try to inject high energy power-law electrons with a changing γ_{max}. The rise of the flare is accompanied by the increase of the injected γ_{max}. The increase of γ_{max} is presumably the cause of the X-ray hard-lags. Before the shock crosses the blob, there blob is filled with a pre-existing population of electrons, which is also subject to radiative cooling. The emission of these electrons represents the low state of the blazar SED.

The parameters used in all cases are summarized in Table 4.1. In this first case, relativistic particles are injected by the travelling shock with increasing $\gamma_{max} = \gamma_{max0} \times 10^{(t'-t'_{start,inj})\times v_{inj}/z}$.

The results produced in this case are shown in Fig. 4.1 & 4.2. The light curves show that hard X-ray raises after, but also falls before the soft X-ray, i.e. the hard X-ray light curve has faster variability compared to the soft X-ray. The DCF shows that X-ray hard-lag is not reproduced in this case.

Since the decrease of the flux level is dominated by radiative cooling, it is easy to

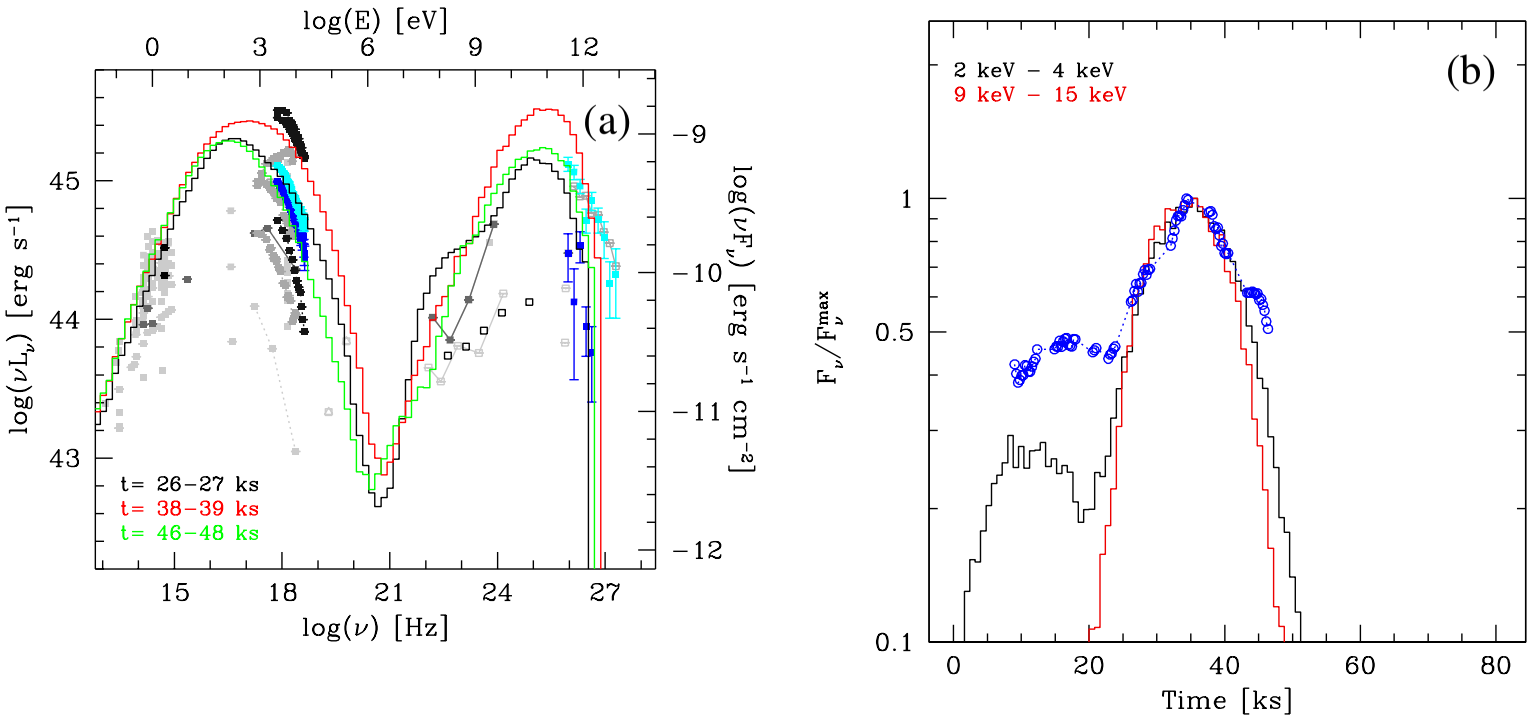

Figure 4.1 : SED and light curves of the first case, with varying injection $\gamma_{\max}$. (left) Broad band SED for three representative times (see labels) during the simulation of the flare. Observed spectra for high and low states during the 2001 March 19 flare in X-ray and TeV γ-rays are plotted in blue and cyan. Other historical data points in grey or black are the same as in Fossati et al. (2008). The black empty squares in the GeV γ-ray band are the Fermi/LAT 1-year averages in five bands. (right) light curves at 2 different energy bands, on 700 seconds bins. Light curves are normalized to their peak values. The RossiXTE/PCA 2-4 keV data are plotted in blue circles.

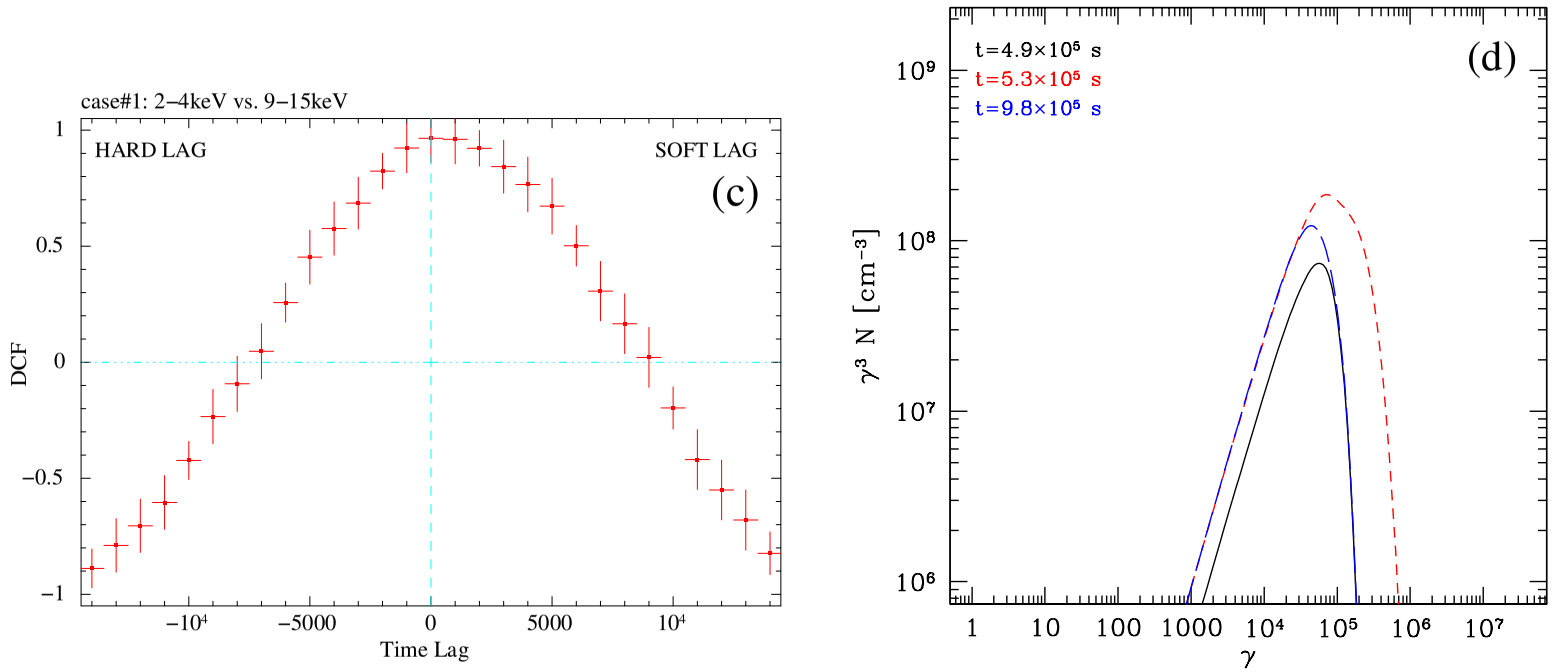

Figure 4.2 : Discrete crorrelation function (DCF) and electron distribution of the first case, with varying $\gamma_{\max}$. (left) DCF analysis. In this case the correlation peaks when there is no lag between the soft and hard X-ray. (right) Electron distribution of the electrons in the bottom center zone. They are ordered in time as black(solid line), red (short dashed line) and blue (long dashed line). The times shown are measured in the frame of the jet.

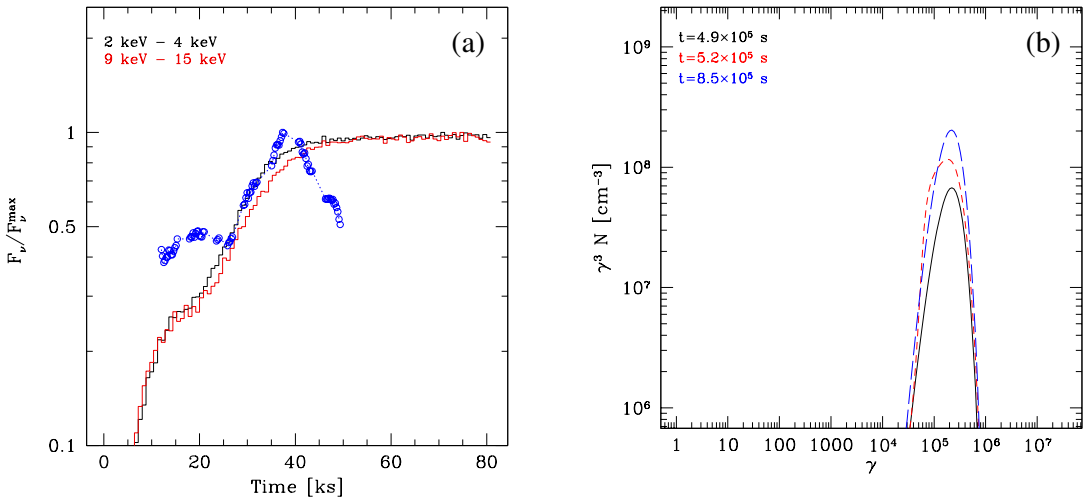

Figure 4.3 : Light curves and electron energy distribution of the second case, in which there is stochastic acceleration without particle escape. The observation data are the same as those in Fig. 4.1.

interpret the flare evolution as because higher energy electrons radiate more efficiently and cool faster. A way to balance the effect of radiative cooling is to have a slow, continous particle acceleration in the radiative zone. This slow acceleration can also contribute to move the SED peak frequency from low energy to high energy, hence produce the X-ray hard-lag.

4.4.2 Case 2: stochastic acceleration without escape

In a second case, we consider a scenario where the blob has ongoing stochastic particle acceleration, either from second order Fermi acceleration or shear acceleration. In the preliminary phase of the simulation, the electrons are under the influence of both radiative cooling and particle acceleration. This leads to a steady state electron population with ultra-relativistic quasi-maxwellian distribution. New electrons begin to be injected into the blob as the shock begins to cross the blob. In this case the energy

of these injected electrons is lower than the energy at which the radiative cooling and stochastic particle acceleration balance. So the electrons will be accelerated, which results in a X-ray hard-lag in terms of emission.

Fig. 4.3 shows a set of results for the second case. The electron distribution shows a movement to slightly higher energy after the injection. In the light curves, this appears as the hard X-ray light curve lagging the soft X-ray one. However, there are two major draw backs. First, apparently, the flux does not fall back after it increases. Second, the resulting electron distribution is an unltra-relativistic quasi-maxwellian distribution (Fig. 4.3b). This kind of particle distribution for blazars was argued against by Ushio et al. (2010).

4.5 hard-lag and soft-lag vs. shock efficiency

In the next two cases, we managed to produce both hard-lags and soft-lags under similar scenarios. The difference that control whether it is a hard-lag or soft-lag is in the efficiency of the shock that injects high energy electrons.

4.5.1 Case 3: stochastic acceleration with escape – hard-lag

From the second case, we learn that if stochastic acceleration is responsible for the X-ray hard-lag, some mechanism other than radiative cooling must be dominating the decrease of flux after the flare. In order to avoid soft lag during the decrease of flux, a good choice would be a mechanism which is energy independent. We hypothesize this achromatic mechanism to be adiabatic expansion or particle escape. Additionally, medium energy electrons($\gamma = 100$) with Gaussian distribution $\sigma_\gamma = 10$ are picked up by the blob at a constant rate $8 \times 10^{-4} cm^{-3} s^{-1}$. The origin of those medium energy electrons could be related to the interaction between the relativistic

Table 4.1 : Summary of model parameters in Chap. 4

Case	local parameters						injection parameters				
	$t_{\rm acc}$	$t_{\rm esc}$	p	$\gamma_{\rm min}$	$\gamma_{\rm max}$	$n_{\rm e}$	p	$\gamma_{\rm min}$	$\gamma_{\rm max0}$	$L_{\rm inj}$	$t'_{\rm start,inj}$
										10^{40}	
	(Z/c)	(Z/c)				(cm^{-3})				(erg/s)	(s)
1: Changing Shock Efficiency	N/A	N/A	1.5	50	8×10^4	4	1.5	50	8×10^4	6.3	5×10^5
2: Stochastic Acceleration	1.5	N/A	0	2×10^4	8×10^4	4×10^{-3}	1.5	6×10^4	7×10^4	0.31	5×10^5
3: Hard-lag	1	0.3	2.3	100	10^5	80	1	100	3×10^4	5	1.2×10^6
4: Soft-lag	1	0.3	2.3	100	10^5	80	1	100	2×10^5	1.6	1.2×10^6

For all cases, $B = 0.13G, R = 0.75\times10^{16}cm, Z = 1\times10^{16}cm, \delta = 33$.

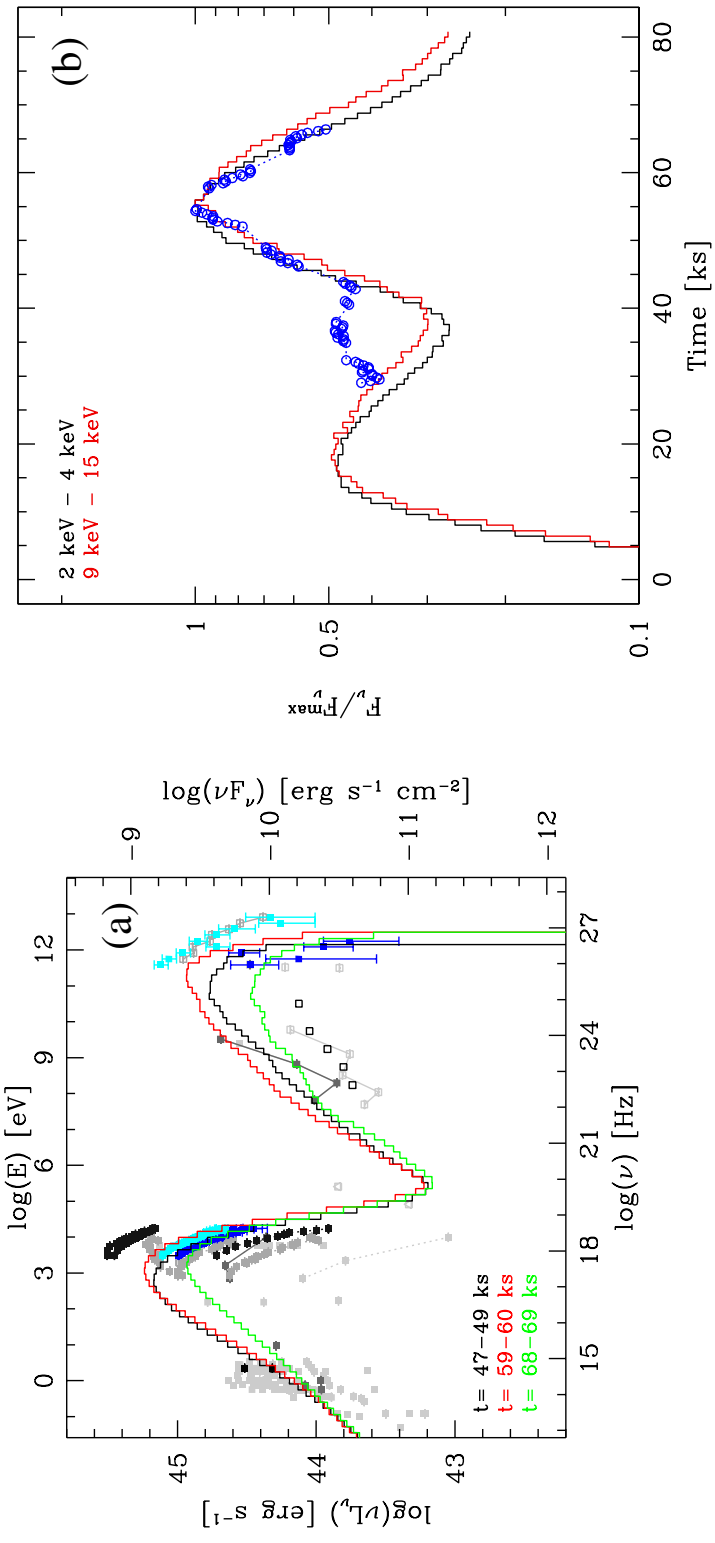

Figure 4.4 : Summary of the SED and light curves of the third case, in which stochastic acceleration is accompanied by particle escape. The observation data are the same as those in Fig. 4.1.

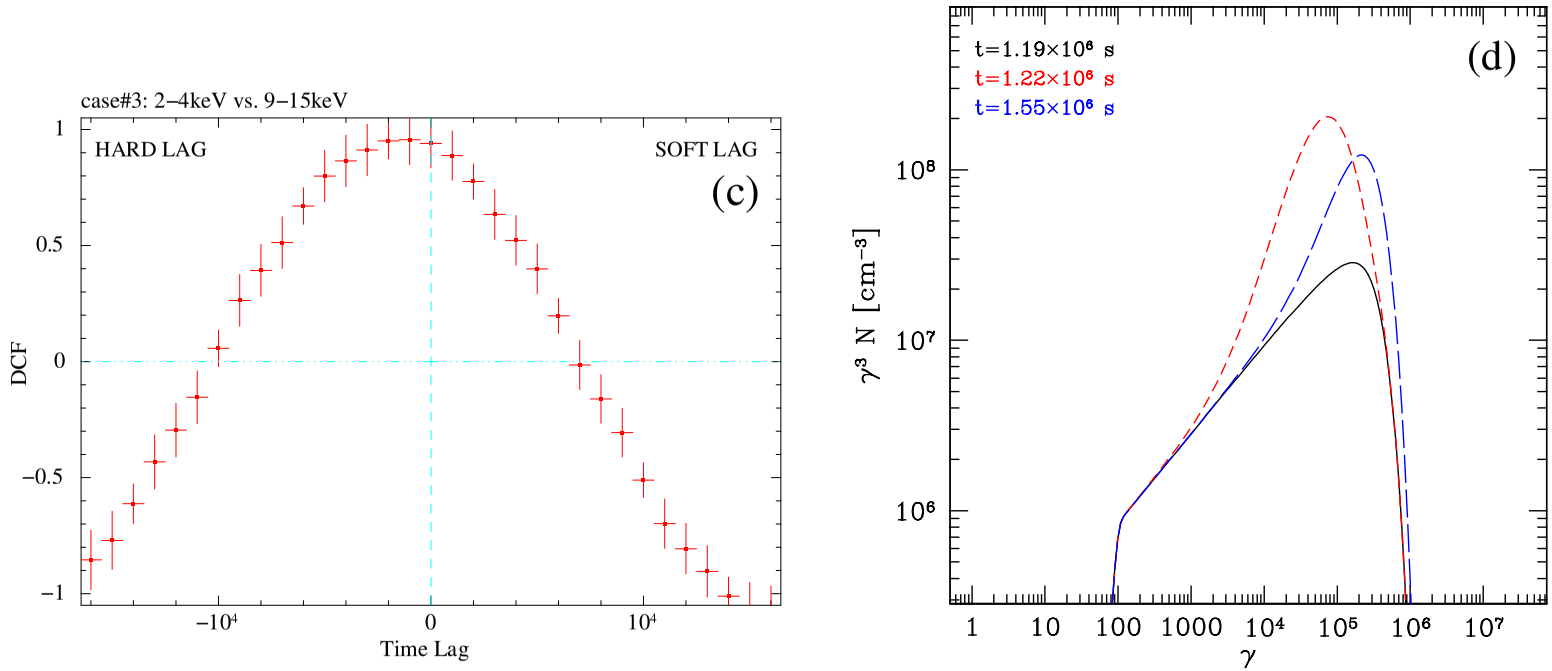

Figure 4.5 : Summary of the DCF and electron distribution of the third case, in which stochastic acceleration is accompanied by particle escape. The observation data are the same as those in Fig. 4.2.

blob and the background medium along the jet (see §2.6.2). These electrons provides a compensation for the particle loss due to 'escape'. Under these conditions, the jet is kept in a steady state, until the shock begins to cross the volume, injecting electrons that are highly relativistic, but less energetic than the electrons emitting at the peak of the quiescent SED. Notice that the blob picks up particles at constant rate, but the particle escape rate is proportional to the electron number density. Because of this, particle escape will win over particle pick up after the shock injects particles into the blob. This will last until the particle density falls back to normal.

The results of this scenario is summarized in Fig. 4.4 & 4.5. The newly injected relativistic electrons are gradually accelerated to higher energy. This case successfully reproduce the X-ray hard-lag we see in observations.

4.5.2 Case 4: stochastic acceleration with escape – soft-lag

In a scenario similar to those in the third case, we can also reproduce X-ray soft lags. If the relativistic electrons injected by the shock are more energetic than the electrons emitting at the peak of the quiescent SED, they will experience radiative cooling that is stronger than the stochastic acceleration. The gradual cooling of these high energy electrons will cause a X-ray soft lag. This is illustrated in Fig. 4.6 & 4.7 as the results of the fourth case.

The parameters used in the fourth case are almost identical to those in the third case, except that the shock injects electrons with higher γ_{max} ($= 2 \times 10^5$), and lower L'_{inj} ($= 1.6 \times 10^{40} erg/s$). In this case, a soft lag (not significant) is observed in X-ray.

This means even for individual flares on the same object, it is possible for us to observe either hard-lag, soft-lag, or no lag in X-ray, based on the efficiency of the shock that is causing that particular flare.

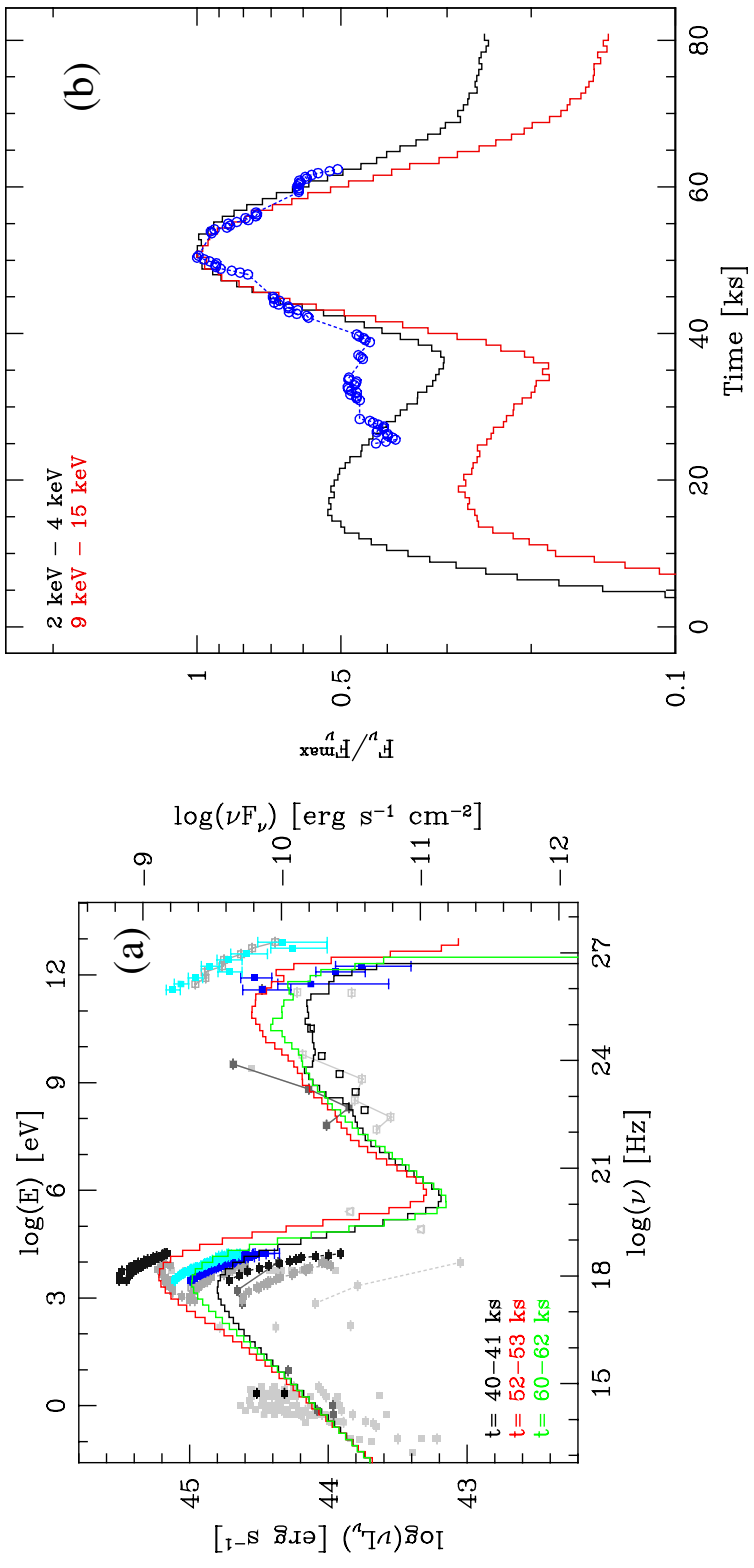

Figure 4.6 : Summary of the SED and light curves of the fourth case, in which stochastic acceleration is accompanied by particle escape. Mostly the same as the third case, except the shock injects electrons with higher γ_{max}, and lower L'_{inj}.

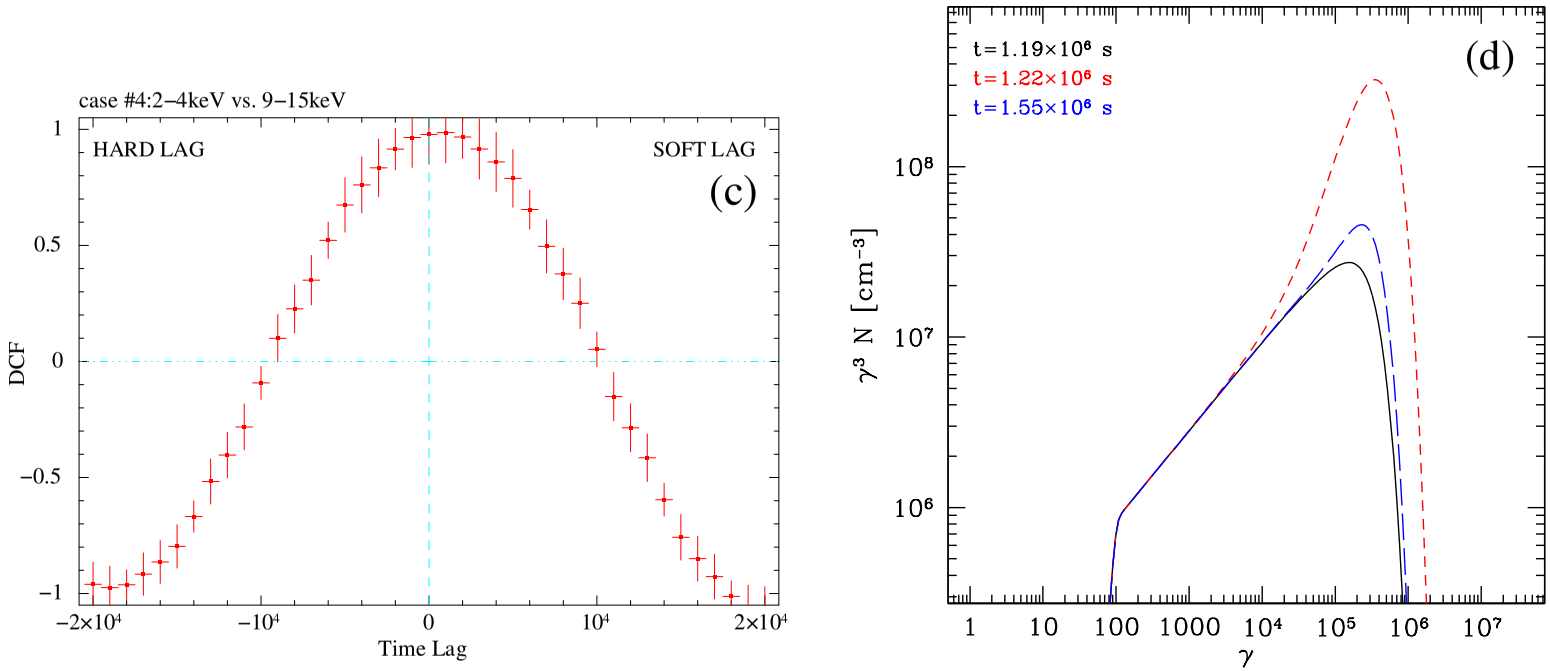

Figure 4.7 : Summary of the DCF and electron distribution of the fourth case, in which stochastic acceleration is accompanied by particle escape. Mostly the same as the third case, except the shock injects electrons with higher γ_{max}, and lower L'_{inj}.

4.5.3 X-ray/γ-ray quadratic correlation

We also notice that case 3 and 4 yield quadratic relations between γ-ray and X-ray fluxes in both the raising and decay phases of the flare (see Fig. 4.8). This is a feature frequently observed in TeV blazars that has proved to be challenging to model (Fossati et al., 2008; Aharonian et al., 2009). In our previous efforts where flare evolution is dominated by radiative cooling, we could only produce the quadratic relation in the flare raising phase (see Chap. 3). The crucial element here is the achromatic energy loss mechanism. This loss mechanism affects at the same time the medium energy electrons that emit the seed photons and the high energy electrons that scatter them to TeV energy by IC process. Hence the decrease rate of the TeV flux is the square of the decrease rate of the X-ray flux, which is emitted by the high energy electrons.

4.6 Summary

Our effort of modeling the X-ray variability of blue blazars showed that not only X-ray hard-lag is an indication that particles are being accelerated in the jet, but also it constrains on how those particles decrease their emission after the peak of the flares. If the decrease of the flare is dominated by an energy dependent cooling processes (usually higher energy particles decrease faster) such as radiative cooling, the light curves will inevitably show a soft-lag during such cooling.

The third scenario we tested has succeeded in producing the X-ray hard-lag. It also successfully produced the quadratic relation between γ-ray and X-ray flares, which has been observed for multiple times (Fossati et al., 2008; Aharonian et al., 2009). The key components of this scenario are the slow particle acceleration, which changes the energy of the newly injected electrons by competing with radiative cooling; and

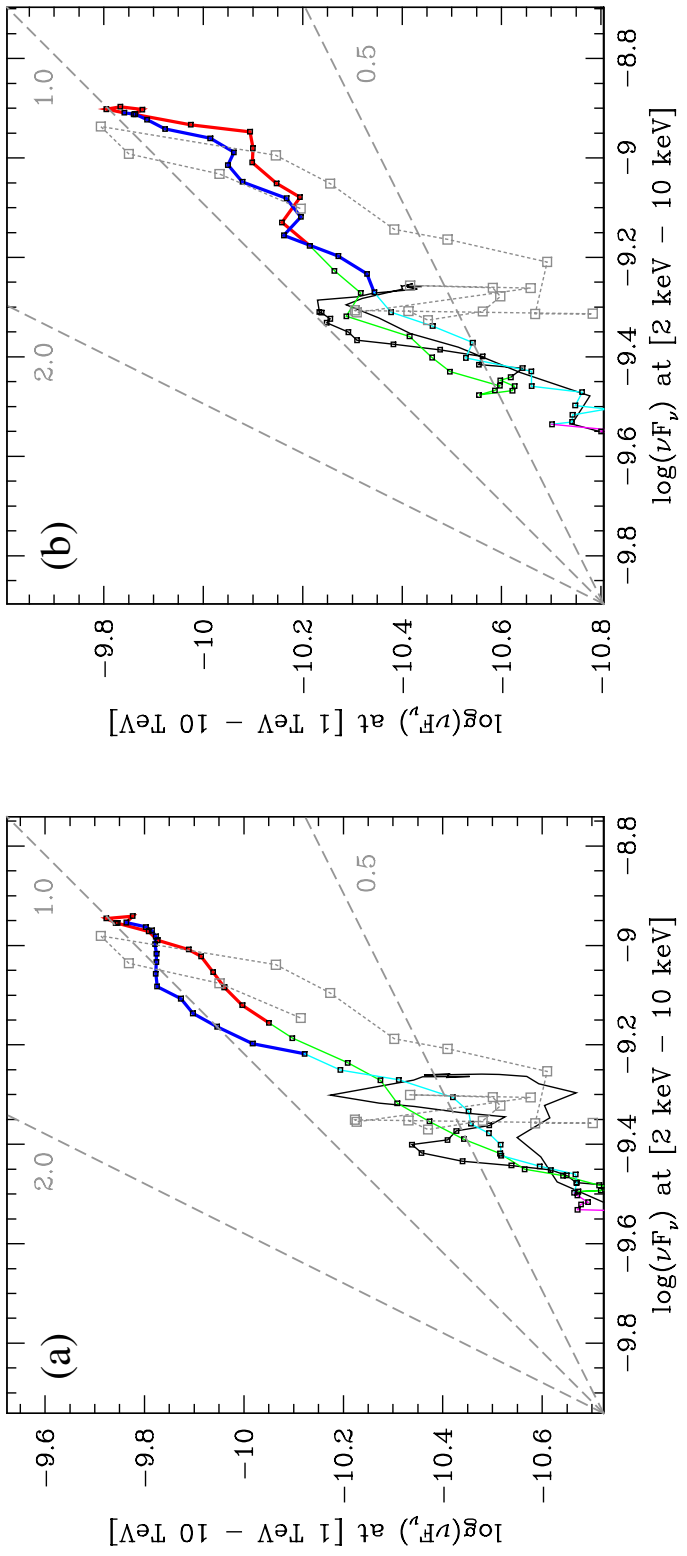

Figure 4.8 : The TeV/X-ray flux-flux correlation for the 3rd(left) and 4th(right) cases. In both those cases they show a quadratic correlation in both raising and decaying phases.

the achromatic electron energy loss, which brings the flux level back to normal after the flare.

The blazar models that depend only on particle injection and radiative cooling have problem explaining the γ-ray/X-ray quadratic relation in TeV blazars, especially during the decrease phase of the flare (see Chap. 3), because the SSC process uses UV photons as IC seed photons. Electrons emitting these photons cool more slowly than the 1keV emitting, IC scattering electrons. So the TeV flux should decrease linearly with the 1keV X-ray flux. However, if the decrease of the flare is caused by an achromatic process such as adiabatic expansion or particle escape, the situation changes. The IC scattering electrons (i.e. the X-ray emitting electrons) and seed photons will decay at similar rates. The TeV flux decay rate should be those two rates multiplied. Hence there is a quadratic relation between γ-ray and X-ray.

Two possible mechanisms that can be the achromatic processes needed here are particle escape and adiabatic expansion. In the scenario of particle escape, when the particles travel to a region with much weaker magnetic field, their synchrotron emissivity becomes negligible and they are considered 'escaped'. These particles can still IC scatter the synchrotron photons, but the chance of scattering decreases with the square of their distance to the synchrotron source. So the IC scattering of these escaped particles can also be considered unimportant. Since the Larmor radius for electrons in blazar jets are small, the magnetic field lines cannot be completely tangled if the electrons are to escape. Notice that the assumption of tangled magnetic field we made in calculating synchrotron emission is mainly a simplification on the calculation, rather than based on any physical consideration. In reality it is very likely that the magnetic field is in some degree ordered, and the electrons have chance to escape along the field lines. Particles should only escape from the outer regions, while particles

in the inner regions just propagate to outer regions. In our model we simplified this process into a uniform decrease of particle density in all zones. In this aspect, adiabatic expansion more naturally agrees with our model as a direct decrease of particle density. But it is more complicated in other ways since it is accompanied by adiabatic cooling and magnetic field strength decrease. A more detailed numerical model is needed to fully explore these effects of adiabatic expansion.

We also stress that, beside reproducing the X-ray hard-lag, the same scenario can as well produce X-ray soft-lag with similar γ-ray/X-ray quadratic relation. This is done simply by changing the energy of the electrons injected by the shock. If the shock is highly efficient, with acceleration timescale very small, it can accelerate the particles to very high energy before it escape from the shock. In this case electrons with high energy are injected into the blob. Because the electrons are under stronger radiative cooling than stochastic acceleration in the blob, we will observe soft-lag. On the other hand, if the shock is not so efficient, with relatively large acceleration timescale, the particles around the shock can only be accelerated to modest energy before it escape into the blob. In this case electrons are under stronger stochastic acceleration than radiative cooling in the blob, so we will observe hard-lag.

To conclude, our modeling effort tells us that an achromatic electron energy loss process, and a slow stochastic particle acceleration are neccesary in the SSC model of blazars, in order to explain the frequently observed X-ray spectral behavior and γ-ray/X-ray quadratic relation in TeV blazars. The hard-lag cannot be simply explained by gradual change of the $\gamma_m athrmmax$ of the electrons injected by the crossing shock.

Chapter 5

Simulation of emission from FSRQ PKS 1510-089 with External Compton Model

5.1 Introduction

The spectral energy distribution (SED) of blazars usually show two major non-thermal components. The low energy one, peaking in the IR-optical-X-ray range is identified as synchrotron radiation. The origin of the high energy one, peaking in the X-ray or γ-ray is less clear. Proposed ideas include inverse Compton (IC) scattering by the same synchrotron emitting electrons, and the so-called hadronic models, in which protons play critical roles in producing these high energy emission. (Mannheim, 1998; Rachen, 2000; Sikora & Madejski, 2001; Arbeiter et al., 2005; Levinson, 2006; Böttcher, 2007; Böttcher et al., 2009). For the IC models, the source of the seed photons is also under debate. If the seed photons are provided by the synchrotron photons at lower energy emitted by the same IC scattering electrons, it is called synchrotron self-Compton (SSC) model; otherwise, it is collectively called external Compton (EC) model. External sources of seed photons may include the photons from accretion disc, X-ray corona, Broad emission Line Region (BLR), infrared torus, the host galaxy bulge, cosmic background radiation (Ghisellini & Tavecchio, 2009), or any other sources external to the emitting blobs.

There are two major classes of blazars: BL Lac objects, which has featureless optical spectrum, and Flat Spectrum Radio Quasars (FSRQ), which has broad emission

line spectra. The emission lines in FSRQ suggest that they are in an environment with stronger external radiation field. Furthermore, these emission lines would be relativistically beamed and enhanced in the frame of the blob, making them even more dominant over the synchrotron emission. Therefore, the EC model is frequently invoked to explain the emission of FSRQs (Dermer et al., 1992; Sikora et al., 1994, 2009).

A major defining feature of blazars is their fast variability. Simultaneous multi-wavelength observation of blazars, and the correlation analysis of these multiwavelength variability can provide insight to the physics going on in the jet. The detailed observation and modeling of these variability has been performed extensively for High energy peaked BL Lacs (HBL) such as Mrk 421 (Fossati et al., 2008; Chen et al., 2011) and PKS 2155-304 (Aharonian et al., 2007; Katarzyński et al., 2008), because their low energy SED peak in X-ray is covered by multiple X-ray satellites, while their high energy SED peak in TeV γ-ray is covered by ground based Cherenkov Telescopes. The launch of Fermi has re-opened the GeV γ-ray sky with unprecedented sensitivity and daily coverage. This energy band covers a highly variable part of the SED right above the peak for several bright FSRQs, such as PKS 1510-089 (Abdo et al., 2010a) and 3C454.3 (Abdo et al., 2009). Simultaneous coverage in other wavelength such as optical and X-ray provided us a chance to obtain multi-epoch SEDs and cross-band correlations, while a deeper understanding of these time series data sets requires time-dependent modeling with all light travel time effects (LTTEs) taken into account.

We have developed a time-dependent multizone code using Monte Carlo method and Fokker-Planck equation to study HBL Mrk 421 under a pure SSC model in Chap. 3 & 4. In this chapter we will extend the model to include external source of IC seed

photons and use this model to study the multiwavelength variability of FSRQ, taking PKS 1510-089 as an example.

5.2 Basic setup

Some details of the Monte Carlo/Fokker-Planck code is described in Chap. 2. The code uses Monte Carlo method to track the production, traveling, and Compton scattering of photons, while it uses Fokker-Planck equation to follow the evolution of electrons. The major strength of this code is that it takes into account all the LTTE. Our model represents a cylindrical jet blob crossing a standing shock as illustrated in Fig.2.2. We treat stochastic acceleration in the whole emission blob as a diffusive term in the Fokker-Planck equation, while first order Fermi acceleration at the shock front is simplified as directly injecting high energy particles into the emission zones where shock is present. This approach is already used and discussed in Chap. 4. The parameters in the model are listed in table 5.1. They represent:

- R and Z are the radius and height of the cylinder,
- B is the magnetic field strength,
- Γ is the bulk Lorentz factor of the jet,
- $n_{\rm e}$ is the electron number density,
- $R_{\rm BLR/IR}$ and $f_{\rm BLR/IR}$ are the radius and covering factor of the BLR or infrared torus (see §5.4),
- $L'_{\rm inj}$ is the luminosity of the relativistic electrons injected by the shock;
- $p_{\rm inj}, \gamma_{\rm min,inj}$ and $\gamma_{\rm max,inj}$ are the spectral index, minimum Lorentz factor and maximum Lorentz factor of the injected electrons,

- $p, \gamma_{\rm min}$ and $\gamma_{\rm max}$ are similar parameters for the electron population existing in the blob when the simulation begins,

- $t'_{\rm start,inj}$ is the time when the shock begins to cross the blob, measured in the frame of the blob,

- $t_{\rm acc}$ and $t_{\rm esc}$ are acceleration and escape time scales,

- $Q_{\rm pick}$ is the rate at which the blob constantly pick up pre-accelerated mildly relativistic electrons (with Gaussian distribution centering at $\gamma_{\rm min}$ in most cases, except in the SSC case, where it centers at $\gamma = 1.2 \times 10^3$).

5.3 PKS 1510-089

PKS 1510-089 is an FSRQ at redshift z=0.361 (Thompson et al., 1990). It is one of the brightest and most variable sources detected by Fermi/LAT. A feature that can be interpreted as disk emission (big blue bump, BBB) is clearly visible in its optical/UV spectrum. VLBI observations of its jet show superluminal motion with apparent speed up to 45c (Jorstad et al., 2005). There is also clear misalignment between the parsec and kiloparsec scale radio jets (Wardle et al., 2005).

Several well collaborated multiwavelength campaigns targeting PKS 1510-089 have been very successful (Abdo et al., 2010b,a; D'Ammando et al., 2011; Marscher et al., 2010; Kataoka et al., 2008; Pucella et al., 2008).

We choose to use the data set observed in 2008-2009 and analyzed in (Abdo et al., 2010a) as the reference data for our simulation (see Fig. 5.1). One particular flare in March 2009 is chosen as the focus of the study of multiwavelength variability.

We aim to reproduce several observational features by matching both the simulated light curves and SED with the observed ones. These features include:

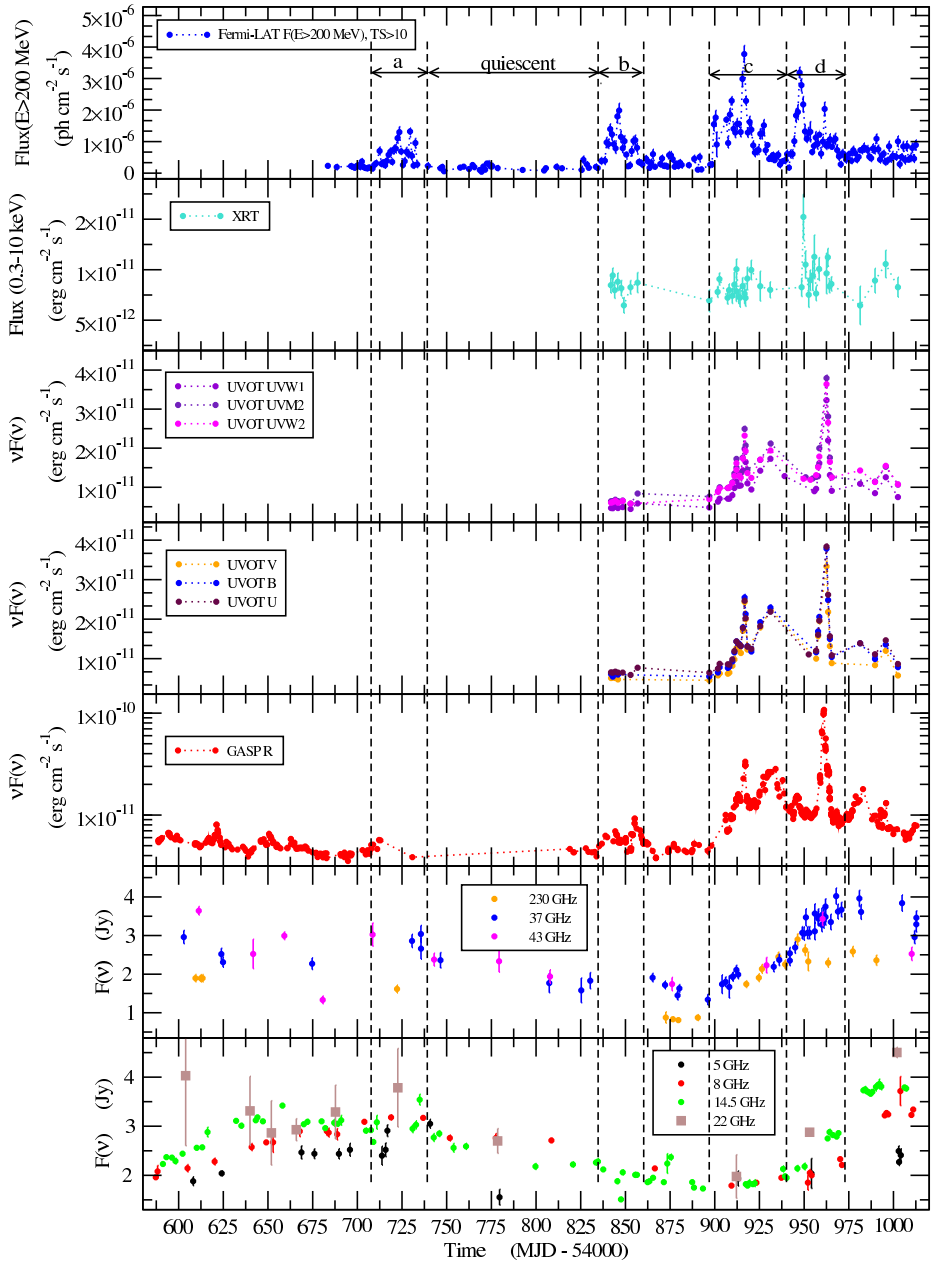

Figure 5.1 : Adopted from Abdo et al. (2010a). Multiwavelength light curves of PKS 1510-089 from April 2008 to June 2009. The vertical dashed lines show the four flaring episodes and the quiescent state. Flare (c) in March 2009 is the one that we fit our simulation to.

- the general two components shape of the SED, and the BBB. These includes both the high states and low states.
- the timescale of the flares, which are typically about 300ks (4 days).
- Both infrared and γ-ray show strong variation with similar amplitude, up to a factor of 10.
- In the March 2009 flare, the infrared and γ-ray flux were strongly correlated, with no significant lags.
- The variation in Swift-UVOT band was less prominent than those in infrared-optical bands. In other words, the optical/UV spectral index became softer during the flare. However, the BBB was still prominent even in the high states.
- The variation in radio bands, and more importantly, in X-ray is modest, within a factor of 2.

We will test the viability of several IC models through time-dependent modeling. Their capability of reproducing the emission characteristics listed above will be the main criterion.

5.4 External Radiation

The relativistic jets in Active Galactic Nucleus (AGN) are possible to reside in environments rich in external radiation. Several of the proposed source of external radiation that are under intense discussion include the radiation from the BLR (Tavecchio & Ghisellini, 2008; Poutanen & Stern, 2010) and the radiation from the infrared torus (Malmrose et al., 2011). The dominance of different external radiation is connected to the location of the γ-ray emitting jets. The radiation from BLR can be dominant

only when the emission region is located at sub-parsec distance from the central engine of the AGN. Beyond that distance, the radiation from infrared torus is likely to dominate on parsecs scale (See Fig.5.2 adopted from Ghisellini & Tavecchio, 2009). Poutanen & Stern (2010) argue that the GeV spectral breaks of FSRQs observed by Fermi is a sign of γ-ray absorption inside the BLR; Meanwhile, Marscher et al. (2010) used the correlation between radio knot appearance and γ-ray flares to put the location of the emission region at parsecs from the central engine. We will test the viability of both these two sources of external photons, and see if they can produce the SEDs and light curves observed.

We treat the big blue bump in the SED of PKS 1510-089 as unbeamed thermal emission from the accretion disc, and matched the data with a luminosity of 4×10^{45} ergs/s and a temperature of $3 \times 10^4 K$. The disc emission is added to the SEDs as a non-varying component after the simulation is completed.

This disc emission is used to estimated the energy density within the radius of BLR $R_{\rm BLR}$, with the formula given by Ghisellini & Madau (1996):

$$U'_{\rm BLR} \sim \frac{17}{12} \frac{f_{\rm BLR} L_{\rm d} \Gamma^2}{4\pi R^2_{\rm BLR} c}. \tag{5.1}$$

Here $f_{\rm BLR}$ is the fraction of the disc emission that is reprocessed by the BLR, $L_{\rm d}$ is the luminosity of the disc emission.

Similarly, the energy density within the radius of the infrared torus R_{IR} can be estimated as (Ghisellini & Tavecchio, 2009):

$$U'_{\rm IR} \sim \frac{f_{\rm IR} L_{\rm d} \Gamma^2}{4\pi R^2_{\rm IR} c} \tag{5.2}$$

With $f_{\rm IR}$ being the covering factor of the torus.

For the spectrum of BLR emission, we either use a blackbody approximation peaked at $1.5\Gamma\nu_{Ly\alpha}$ or take the unbeamed BLR spectrum in Fig.4 of Tavecchio &

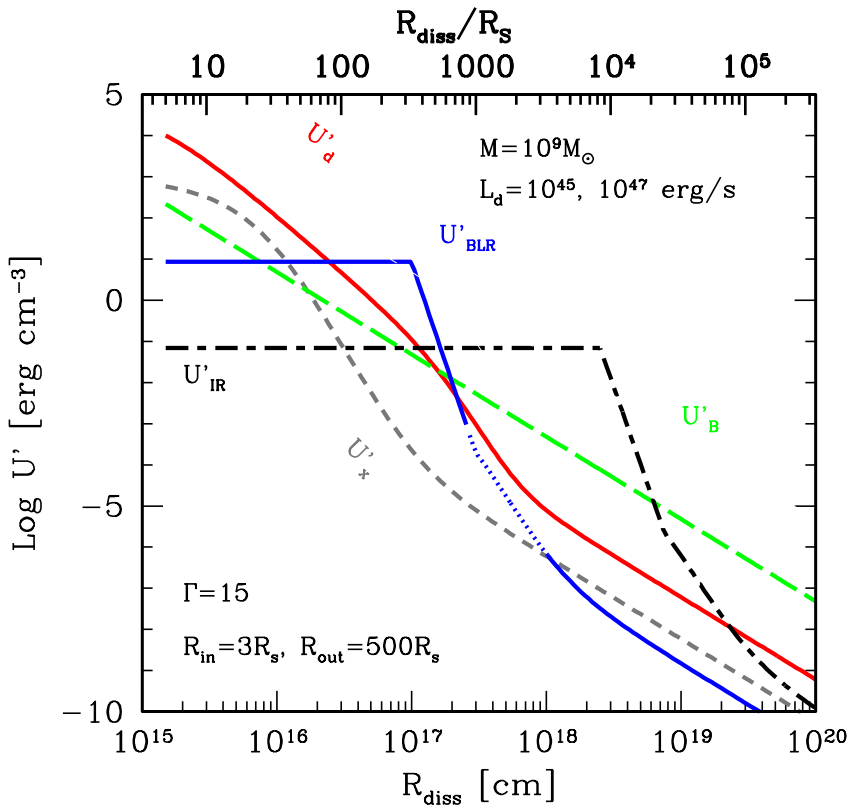

Figure 5.2 : Adopted from Ghisellini & Tavecchio (2009). Comparison of different energy densities as measured in the comoving frame. The moving blob is assumed to have a bulk Lorentz factor of $\Gamma = 15$. The black hole has a mass $M = 10^9 M_\odot$. The disc emits as a blackbody, and extends from 3 to 500 Schwarzschild radii. The X-ray corona is assumed to be homogeneous, to extend up to 30 Schwarzschild radii and to emit 10 percent of the disc luminosity. The contribution of the BLR between 1 and $3R_{\rm BLR}$ depends on the unknown width of the BLR itself (dotted line).

Ghisellini (2008) and beam it according to the equation:

$$U'(\nu') = \frac{2\pi}{\Gamma\beta c}\nu'^2 \int_{\nu_1}^{\nu_2} \frac{I(\nu)}{\nu^3} \mathrm{d}\nu, \tag{5.3}$$

here $\nu_1 = \nu'/[\Gamma(1+\beta)]$, $\nu_2 = \nu'/\Gamma$, $I(\nu)$ is the unbeamed intensity spectrum, $\beta = \sqrt{1-\frac{1}{\gamma^2}}$ is the velocity of the blob in units of c, ν and ν' are the frequency in the observer's frame and blob frame respectively. We compare the difference when using these two spectra for the BLR radiation.

For the infrared torus, we use a blackbody spectrum with temperature (Ghisellini & Tavecchio, 2009):

$$T'_{IR} = 370bK \sim 370\Gamma K, \tag{5.4}$$

where $b \equiv \Gamma(1-\beta\mu)$, $\mu = cos\alpha$. α is the angle between the jet axis and the line connecting the source and the jet, so $\alpha \sim \pi/2$ for the torus.

We simplify the model by assuming that all the external photons are travelling in the upward direction in the frame of the bolb, in the geometry shown in Fig. 2.2. So the external flux is just the energy density times c. All the external photons enter the blob through the lower boundary.

5.5 Results

We want to reproduce the quiescent and flaring states of PKS 1510-089. First we use the BLR emission as the source of external photons. Then we test the model in which emission from the infrared torus dominates, as well as a pure SSC model, to see if these models can reproduce the SEDs and light curves of PKS1510-089 as well.

Table 5.1 : Summary of model parameters in Chap. 5

Case	local parameters							injection parameters				
	R	Z	B	Γ	$n_{\rm e}$	$f_{\rm BLR/IR}$	$Q_{\rm pick}$	$L'_{\rm inj}$	$p_{\rm inj}$	$\gamma_{\rm min,inj}$	$\gamma_{\rm max,inj}$	$t'_{\rm start,inj}$
	10^{16}	10^{16}						10^{44}				
	(Z/c)	(Z/c)	(G)		(cm^{-3})	%	$(cm^{-3}s^{-1})$	(erg/s)				(s)
1: Quiescent State	6	8	0.3	15	2.66×10^4	1.3	0.1	N/A	N/A	N/A	N/A	N/A
2: Shock Crossing	6	8	0.3	15	2.66×10^4	1.3	0.1	3.5	3.2	30	2×10^4	7×10^6
3: Larger δ	10	13.3	0.16	25	1.4×10^3	0.15	0.0032	2.8	3.2	6	4×10^3	1.2×10^7
4. IR torus model	6	8	0.2	15	7.37×10^2	50	0.019	5	3.2	300	2×10^5	7×10^6
5: Pure SSC	3.75	5	0.1	10	100	N/A	0.002	8	3.2	2×10^3	1×10^5	5×10^6

For the first 3 cases, the existing electrons have $p=3.2, \gamma_{\rm min}=5, \gamma_{\rm max}=2\times10^3, t_{\rm acc}=0.55Z/c, t_{\rm esc}=0.1Z/c$.

For the IR torus model, these parameters are $p=3.2, \gamma_{\rm min}=50, \gamma_{\rm max}=2\times10^4, t_{\rm acc}=0.09Z/c, t_{\rm esc}=0.015Z/c$.

For the SSC model, these parameters are $p=3.3, \gamma_{\rm min}=1\times10^3, \gamma_{\rm max}=1\times10^5, t_{\rm acc}=0.19Z/c, t_{\rm esc}=0.03Z/c$.

Additionally, $R_{\rm BLR}=8\times10^{17}cm, R_{\rm IR}=7.8\times10^{18}cm$.

5.5.1 Quiescent State: No shock

First we try to reproduce the quiescent state SED of PKS 1510-089. We begin with using the blackbody approximation for the spectrum of the BLR emission. We show the results of this simulation in Fig. 5.3, with the parameters used listed in Table 5.1.

Because there is no flaring activity, the flux level in every wavelength reaches the steady state after the initial setup, and the light curves remain almost flat except for some statistical fluctuations. It is interesting to note that the R-band light curve reaches a flux level higher than the quiescent level before it reaches steady state. This is because the external photons need some time (one light crossing time) to diffuse through the whole blob. During that time some zones which have not yet received the external photons will experience significant less IC cooling (which is dominant over synchrotron cooling in this case). Hence these electrons will remain at a relatively high energy and produce relatively high level of synchrotron radiation during this phase. This is an example of how the light travel time effect can affect the actual physics in the jet, not only just the way we perceive the emission.

The SEDs at several epochs almost overlapped, as expected. They matched the low state data points (cyan) in optical and γ-ray pretty well. The radio data points do not match because it is likely that the radio emission comes from additional emission regions rather than just the one producing optical and γ-ray emission. The simulated spectrum in the X-ray is much harder than the observed one. This is improved if we use the more detailed description of the BLR spectrum as those used in Tavecchio & Ghisellini (2008). The resulted SEDs are shown in Fig. 5.4. This confirms their conclusion: this treatment of the BLR spectrum is important in producing the soft X-ray flux, but not very much for other bands.

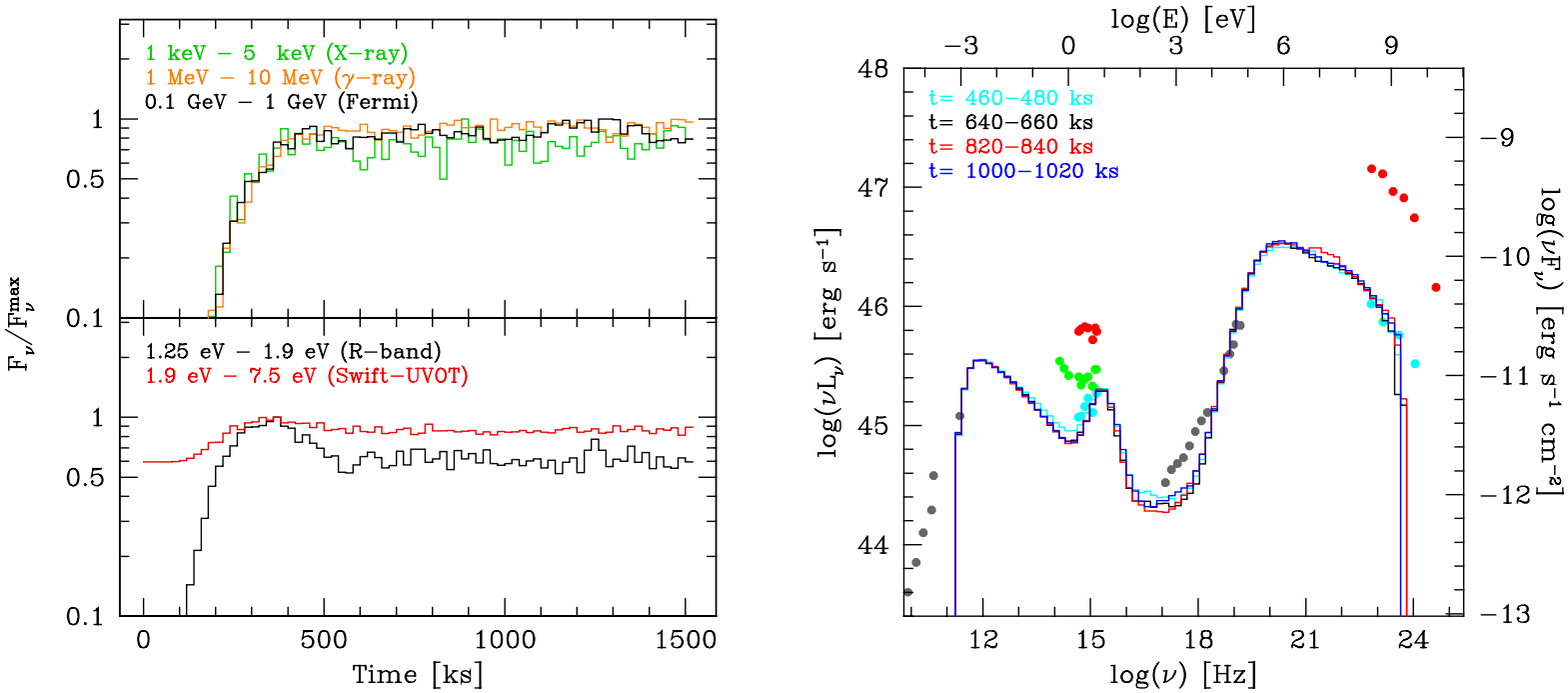

Figure 5.3 : The light curves (left) and SEDs (right) for the quiescent state of the BLR model, using a blackbody approximation for the BLR spectrum. The histograms in both figures are the results of simulation, with the energy band chosen shown in the legend of the left figure, and the snapshot time bins shown in legend of the right figure. The data points in the right figure are multiwavelength SEDs of PKS1510-089 mostly in 2009 from Abdo et al. (2010a). The red/cyan points in optical and γ-ray represent the high/low state of the flare in March 2009. But the optical and γ-ray points are not strictly simultaneous. The green optical points are intermediate state before the flare reaches the maximum. The points in radio band are GASP data in March 2009. The X-ray data include the XRT data averaged during the March 2009 flare, and five year integrated BAT data in hard X-ray.

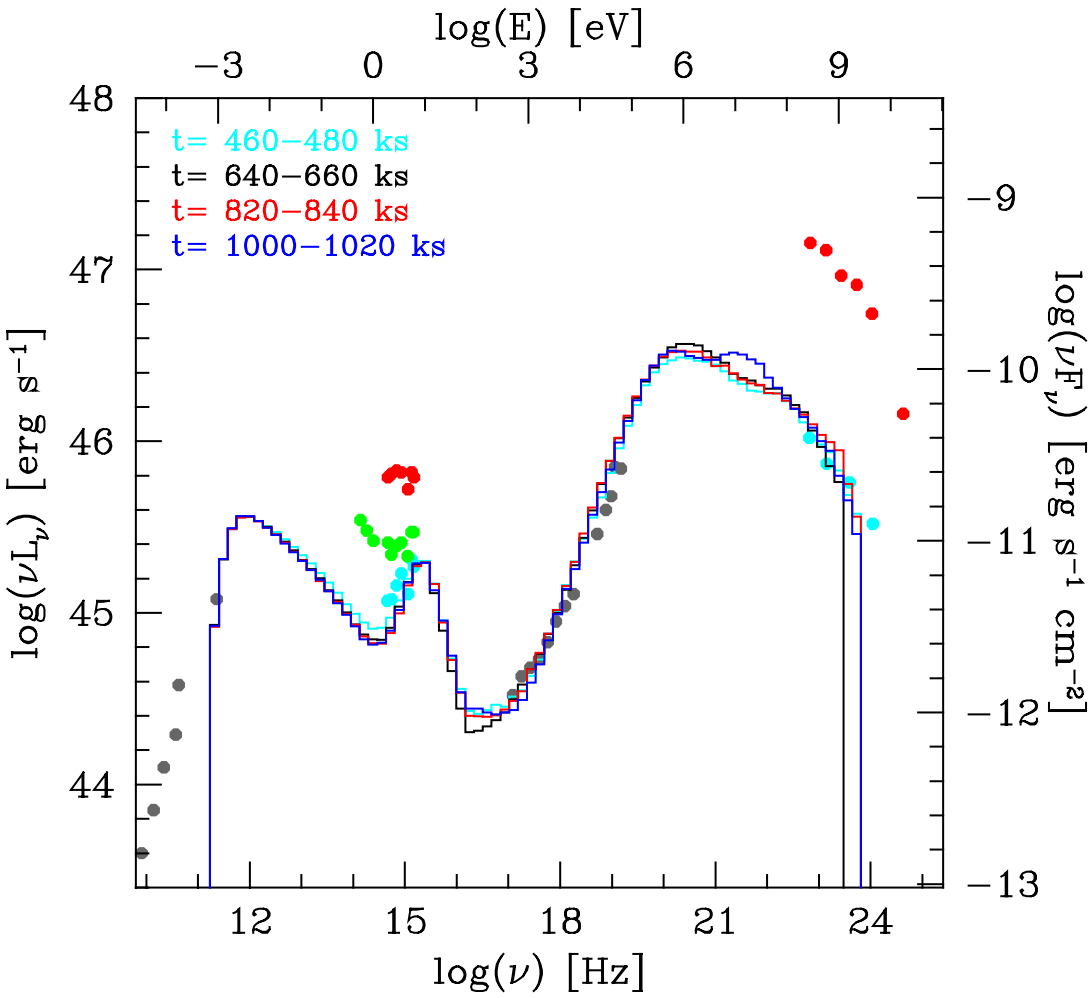

Figure 5.4 : The SEDs for the quiescent state of the BLR model using the Tavecchio & Ghisellini (2008) BLR spectrum.

5.5.2 Flare: Shock Crossing

On the basis of the quiescent state case, we model the flares as the standing shock injects relativistic electrons into the blob when it travels through the blob in the blob frame, as shown in Fig. 2.2. These newly injected electrons emit through both synchrotron and IC, producing correlated optical and γ-ray flares. The results are shown in Fig. 5.5.

The light curves show that the variability in the R-band is smaller than that of the Swift-UVOT band, due to the contribution by the not varying big blue bump emission. This is consistent with observations. The high energy light curves also show that the X-ray light curve lags the γ-ray light curve by about 20ks. Producing this kind of lag shows the capability of our numerical code. However, these lags have not been clearly detected in the observation. Since the large variation in X-ray produced in the simulation should not exist, the lags should probably not be detectible either, when the variation is somehow surpressed or diluted.

By looking at the X-ray light curve, or the SEDs, it is easy to notice that there is large variation in X-ray in the simulation results. This is at odds with the observation in which only modest variation (less than a factor of 2) is seen in X-ray. This excessive X-ray variation is likely the result of SSC emission. Although our model does not directly discriminate EC photons and SSC photons, the parameters we use indicate that the SSC emission is not negligible in X-ray during the quiescent state. So when there is a flare caused by injection of high energy electrons, the variation of the SSC emission should be even larger than that of the synchrotron emission. This SSC variation makes this model and parameter set not consistent with the observed feature of PKS 1510-089. This example also tells us how important it is to model the way the blazar emission evolves, rather than simply model the high state and low state

SED with unrelated different parameter sets.

5.5.3 Flare: Shock Crossing, with high Doppler Factor

In order to decrease the level of SSC emission, while keeping the same level of synchrotron emission, we need to decrease the ratio between the synchrotron (SSC seed photon) energy density and the magnetic energy density (see §1.5). We can achieve this by increasing the Doppler factor through which we observe the jet, because in that case the synchrotron energy density in the blob frame needs to decrease accordingly to match the optical data. There are also change of other parameters. They are shown in table 5.1. The results are shown in Fig. 5.6.

In this case, the flux in X-ray is weaker, but there is still significant level of variation. However, since the quiescent X-ray flux is lower than the observed one, it is possible to explain the X-ray as having contribution from additional relatively cooled blobs, which can dilute part of the large variation. Taking that into account, there will still be modest level of variation remaining, consistent with the observation.

Similar to the last case, the X-ray light curve also slightly lags the γ-ray light curve.

5.5.4 EC dominated by IR emission from the torus

We also test if the emission from infrared torus can be a viable source of external photon and produce adequate light curves and SEDs. This scenario is motivated by the observation of the coincidence of γ-ray flares with the appearance of new knots in radio images of PKS 1510-089 (Marscher et al., 2010). These observation hints that the location of γ-ray flares are on parsec-scales, which is beyond the usually inferred radius of the BLR (Kaspi et al., 2007; Bentz et al., 2006, 2009). At this distance, the

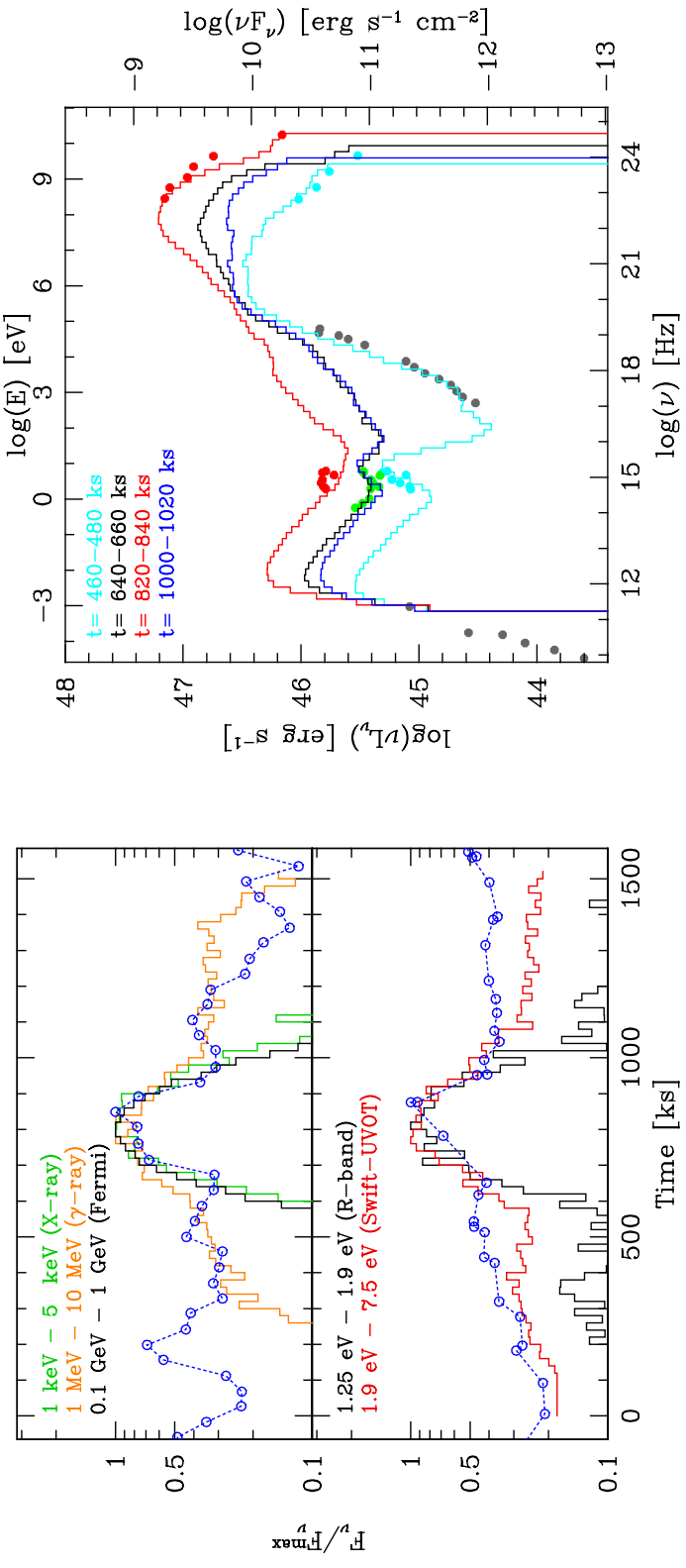

Figure 5.5 : The light curves (left) and SEDs (right) for the shock crossing case of the BLR model, using the detailed BLR spectrum. The blue circles in the lower panel of the left figure is the observed R-band light curve in March 2009 from the GLAST-AGILE Support Program (GASP). The blue circles in the upper panel of the left figure is the Fermi light curve above 0.2GeV in March 2009, simultaneous with the R-band data. The SED data points are the same as those in Fig. 5.3.

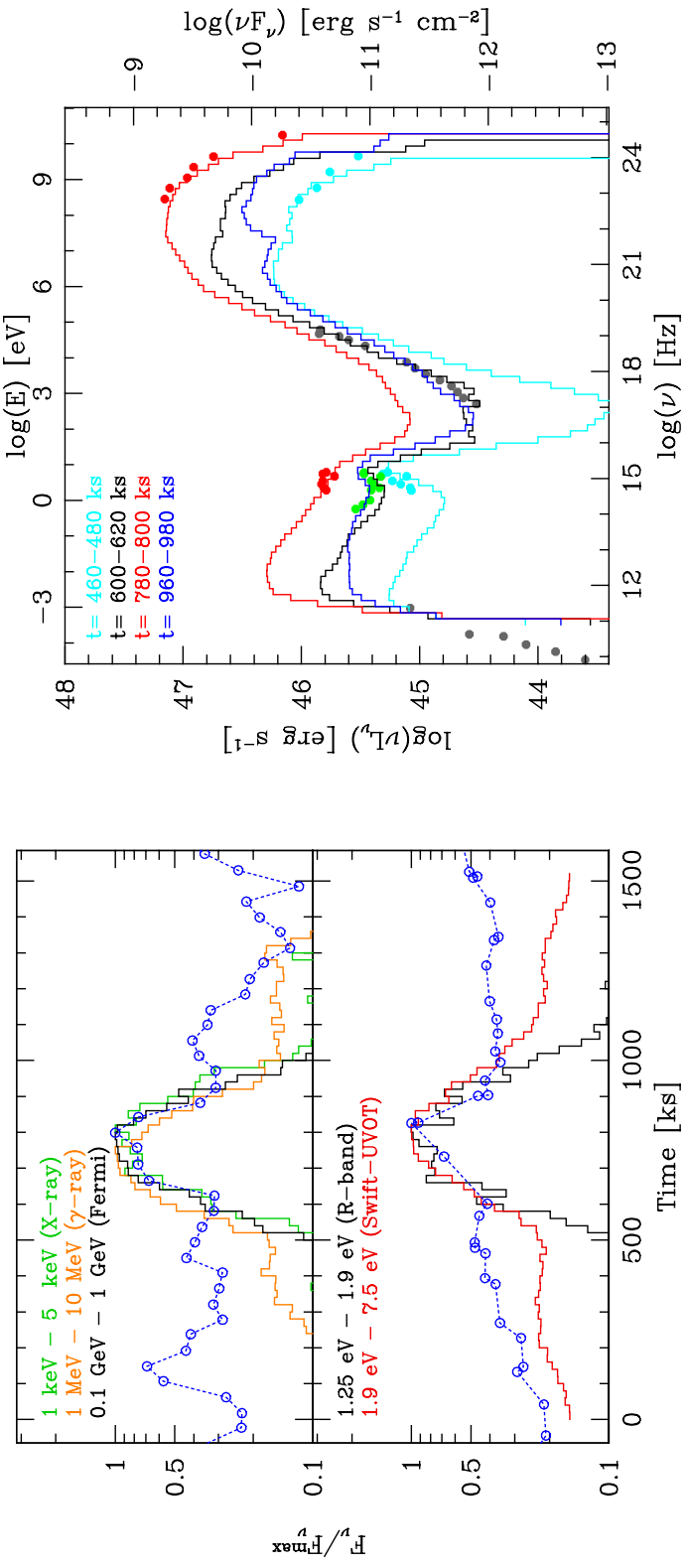

Figure 5.6 : The light curves (left) and SEDs (right) for the case with larger Doppler factor. There is a shock crossing the blob, and we use the detailed BLR spectrum for the external source of photons. The data points are the same as those in Fig. 5.5.

IR torus (Pier & Krolik, 1992b,a) becomes a major candidate as the source of EC seed photons.

We calculate the energy density and temperature of the torus emission according to (5.2) and (5.4). By adjusting the parameters, especially R, B, $n_{\rm e}$, $f_{\rm BLR/IR}$, $\gamma_{\rm min}$ and p, we obtained a set of parameters (see table 5.1) that can produce reasonable light curves and SEDs (Fig. 5.7).

One of the main difference between the torus emission and the BLR emission when they are considered as source of EC seed photons is that, the torus radiates at lower frequency compared to the BLR. This means to scatter these seed photons to γ-ray, the energy of the electrons need to be higher than those needed in a BLR scenario. In other words, more efficient particle acceleration is needed to sustain the high energy electrons. This also means faster particle escape is to be expected in the torus scenario, otherwise the accelerated particles will not form a power-law distribution that can produce emission with the observed spectral index. It turns out that the particle escape time scale needed in this case is too fast too be realistic ($t_{\rm esc} = 0.015Z/c$).

The issue of X-ray variability in this case is similar to the one in the BLR case. So it is likely that in a similar way, a higher doppler factor could lower the X-ray produced by SSC.

Otherwise, this case produced the observed phenomena well. The broadband SED is reproduced; the light curves vary on a timescale consistent with the data; the optical and γ-ray light curves are well correlated with no significant lags; the variations in optical and γ-ray have similar amplitude; the variation in UV band is less prominent than those in optical.

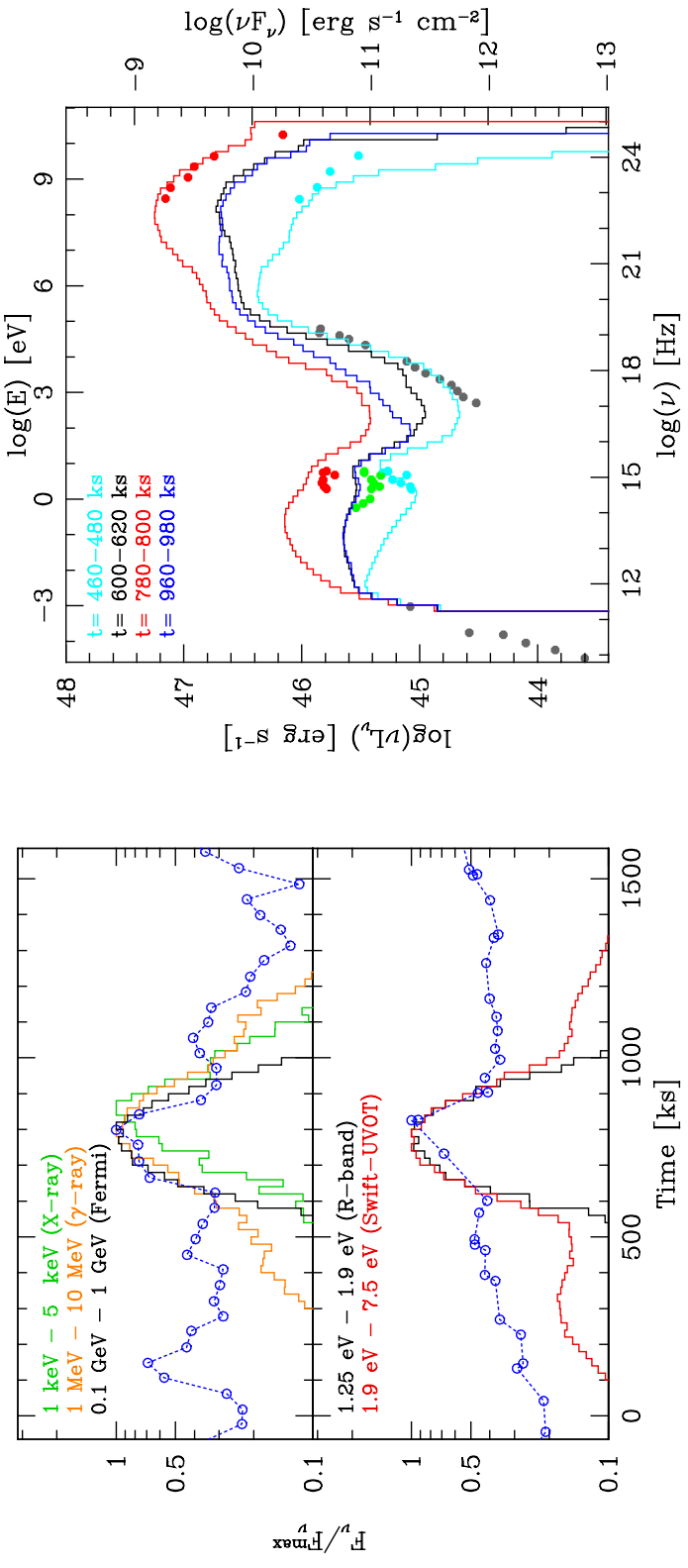

Figure 5.7 : The light curves (left) and SEDs (right) for the case with the emission of the infrared torus as the source of external photons. The data points are the same as those in Fig. 5.5.

5.5.5 Pure SSC Model

We also test if pure SSC model can produce the observed light curves and SEDs. The results are shown in Fig. 5.8.

Generally, the SSC model can reproduce the observation really well. The light curves show that the variability in X-ray is small, within a factor of 2; The R-band varies less than the Swift-UVOT band. These are all consistent with the observation. However, the simulation produces an X-ray spectrum that is harder than the one observed. Similarly, the simulated infrared spectrum is also harder than the observed intermediate state spectrum. Overally the frequency at which synchrotron spectrum peaks seems too high to match the observed SED. Since there is essentially fewer free parameters in the SSC model (no $f_{\rm BLR/IR}$), the parameters are more constrained than those in the EC models. So there is not much we can do to resolve the problem.

5.6 Summary

We have modeled the jet of PKS1510-089, mainly with EC model using external radiation from BLR or infrared torus. The BLR model can produce satisfactory result if the bulk Lorentz factor of the jet is at least 25. We confirmed that blackbody approximation of the BLR spectrum is enough in modeling blazars except at soft X-ray (Tavecchio & Ghisellini, 2008). If we use emission from the infrared torus as the source of external photons, we need very fast particle acceleration and escape to maintain the balance between acceleration and cooling at high energy. Pure SSC model is also not excluded by the observed light curves and SEDs. The simulated SEDs are harder than the observed ones in infrared and soft X-ray. But the issue in X-ray can be relaxed if the SEDs in this band have contribution from other regions.

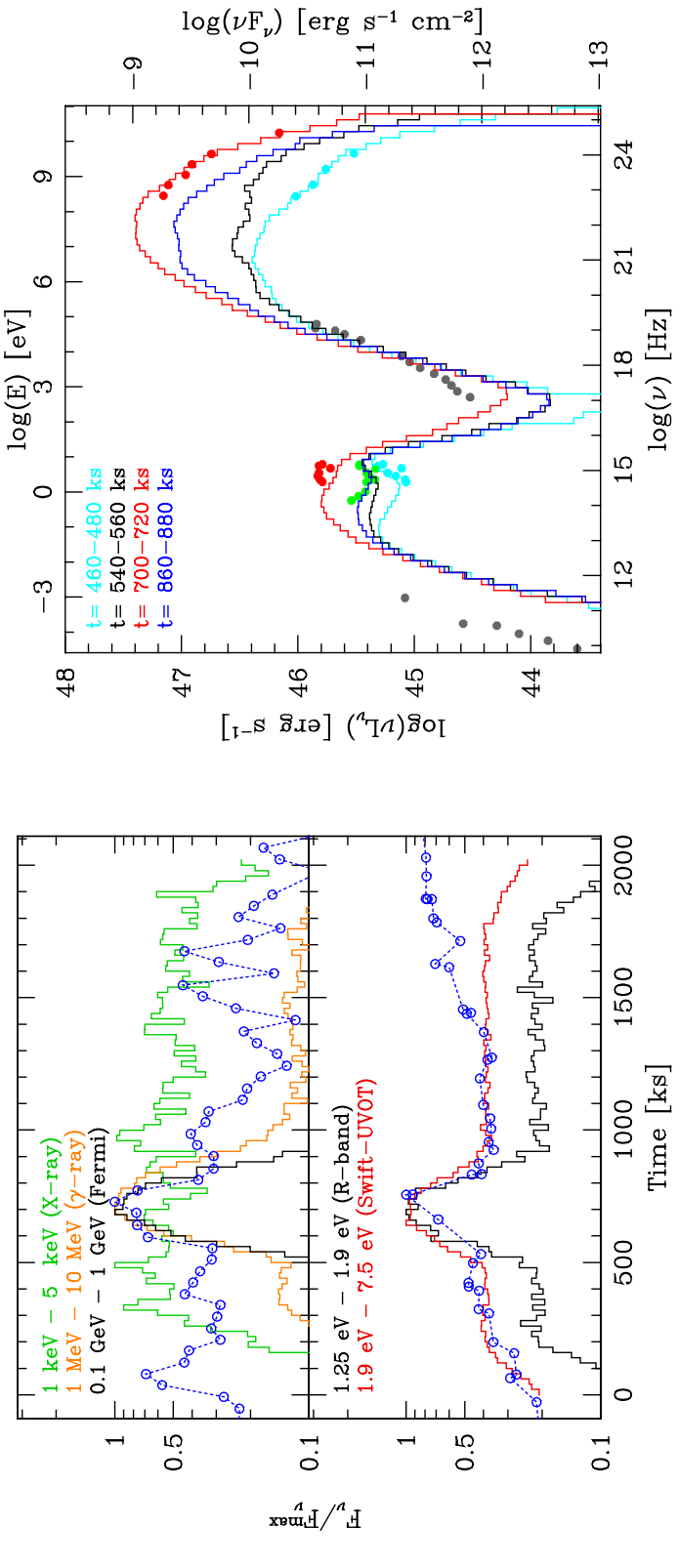

Figure 5.8 : The light curves (left) and SEDs (right) for the SSC case. The data points are the same as those in Fig. 5.5.

Our modeling work does not give conclusive answer about which models can be excluded. However it does favor the BLR EC model with Lorentz factor of at least 25, based on the arguments on X-ray variability, particle acceleration and escape rate, and infrared spectrum.

We also noticed some timing features in our simulation that have not yet been well assessed by observations, such as the short time scale lags between different bands. If future well sampled observations can detected these kinds of timing features, our code will be the ideal tool to explain them and further differentiate models.

In the EC models, we have 5 basic observables (variability time scale $\tau_{\rm var}$, synchrotron luminosity $L_{\rm sy}$, estimated IC peak frequency $\nu_{\rm ic,p}$, IC luminosity $L_{\rm ic}$, and γ-ray spectral index s_γ) to constrain 6 free parameters (R, B, $n_{\rm e}$, $f_{\rm BLR/IR}$,$\gamma_{\rm min}$ and p). However, there are additional constraints, e.g. the SSC can not be too strong, which requires the B to be large enough; the stochastic acceleration and hence the cooling can not be too fast, which requires the B not to be too large. These additional constraints put the model in a limited space of parameters. p and $\gamma_{\rm max}$ in the quiescent state are not direct input parameters. They are the results of the combination of $t_{\rm acc}$ and $t_{\rm esc}$. The synchrotron peak frequency $\nu_{\rm sy,p}$ is not used because it is not a result of the electron distribution, but it is largely affected by synchrotron self-absorption for the parameters used in our model. And at the same time, its position in the SED is largely uncertain from currently available data. Some parameters, such as the bulk Lorentz factor of the jet, the radius of the BLR or torus, have estimates from other independent studies, therefore are not considered as free parameters in this study. Certain observables, such as the IC peak frequency, are only roughly estimated. So in the end the parameters are not tightly constrained.

We have used a simplified model of energy independent particle acceleration in this

work. In order to maintain a power-law electron distribution with certain slope, the particle escape time scale is tied to the acceleration time scale. So the fast radiative cooling in our model requires fast particle acceleration and hence fast particle escape. This required escape time scale has turned out to be smaller than the limit of Z/c, which happens if all particles travel freely at the speed of light. However, the actual particle acceleration process should be more complicated than just energy independent. A more realistic energy dependency of the particle acceleration process may change the required acceleration and escape time scales. Therefore, the acceleration and escape time scales derived here are only for instructive purposes.

Chapter 6

Conclusion

We live in an era when time dependent observation of high energy, especially γ-ray, sources are just beginning to take shape. This offered us the opportunity to carry out simultaneous multiwavelength observation of the variability of these γ-ray sources, which happen to be highly variable sources in a lot of cases. Blazars are among the most studied γ-rays sources because of their important role in the unification of AGN. We think there is an urgent need for a time dependent blazar model to bridge these observation with our understanding of the underlying physics.

We have built on the MC/FP numerical code the time-dependent blazar model that can fully account for all LTTEs. With the help of this model, the various timing features of blazar emission begin to reveal what is going on in blazar jets.

The first piece of information on the time axis that can be utilized is the variability time scale. With this constraint added to the constraints from the broadband SED, the SSC model is reasonably constrained. For Mrk 421, because we have included internal LTTE, the observed delay between the IC and synchrotron light curves and the symmetry of X-ray and γ-ray light curves are reproduced. This signals the initial success of the model. The time lags between hard and soft X-rays, and the quadratic relation between X-ray and γ-ray, on the other hand, call for particle acceleration and escape in the model.

One of the main results from the modeling of PKS 1510-089 is that the low level of observed X-ray variability requires minimal contribution from SSC. This further

requires a high Doppler factor and a strong magnetic field. But a strong magnetic field also indicates strong radiative cooling. In order to accelerate particles to ultra-relativistic energies with a power-law distribution, un-reasonablely fast acceleration and escape are then required. So a high Doppler factor seems necessary.

However, currently the modeling work can not pinpoint which IC model is the one that produces the emission of FSRQ, since each model has its own issue. The model with BLR emission requires relatively large Doppler factor and additional emission component to dilute the X-ray variability. The model with IR torus emission has this same problem, and in addition, the particle escape timescale required in this case is extremely small. The pure SSC model is less troubled by the X-ray variability. However, the particle escape timescale required is also very small. There is also the problem that the spectral indices produced in optical and X-ray do not agree with the observation, although this may be eased by contribution from additional emission components.

6.1 Outlook

There can be a few directions of expansion of the current work.

Further areas of study concern inhomogeneities and different geometries, which can be easily studied with this code. We can introduce a spatial structure to the magnetic field, either static or changing according to some prescription, which could be motivated as caused by compression and amplification of the tangled field by a shock, and we can also expand the code to deal with anisotropic magnetic field.

It is also expected that the blobs of blazar jets will go through adiabatic expansion as they travel. Further expanding the code for this capability is desirable. It is possible that expansion can take some of the roles played by particle escape and

radiative cooling.

The physics of the shock and its upstream/downstream are largely simplified in the current work, with only change of electron distribution across the shock. A more realistic treatment should include the changes of magnetic field, electron number density, and flow velocity. The geometry of the shock should be more complicated than just a flat surface perpendicular to the velocity of the jet.

6.1.1 Future of the MC/FP code

Besides dealing with blazar jets, this code can also be used to model jets at larger scale when the variability becomes a topic of concern. The capability of this code is most useful in the situations where the source is optical thick, hence multiple Compton scattering becomes important (e.g. Finke & Böttcher, 2007); or where even though the source is optical thin, the variability of the source is comparable to the light crossing time, so that LTTE becomes important.

6.1.2 Future of blazar modeling

The leptonic model for blazars is relatively mature with the LTTE now considered. However, the large uncertainty lies in the theory of particle acceleration, and the nature of the external radiation.

Most blazar models (e.g. Krawczynski et al., 2002; Katarzyński et al., 2008), including the one in this thesis, rely on the unspecified particle injection process by the shock. The particle energy, distribution, injection rate, and how the injection varies as the shock travels, are all free parameters in the model. Although the theories of shock acceleration themselves are not complete yet, incorporating the existing ones could further strengthen the blazar models (see Kirk et al., 1998, for an example).

The uncertainty in the external radiation field can be understood as a weak spot of blazar models. But more importantly, it is a major issue that EC blazar models want to help resolving. However, if we do obtain more knowledge of the components and structure of the AGN, like the distribution of BLR blobs, the size and structure of the IR torus, through independent technics such as reverberation mapping, the blazar models will of course benefit, and contribute directly to identify the actuall emission site of the γ-ray flares in blazars.

Appendix A

Technical information

The code was originally written in Fortran77. Newer sections make use of certain Fortran90 features and syntax, such as recursive subroutines. MPI is used for parallelization of the code, in both the F-P and MC sections. There are approximately 34,000 lines in the code. The main program is in the `'compton2d.f'` file. After reading input files (`'reader.f'`) and setting up the simulation (`'setup2d.f'`), the main loops are managed in `'xec2d.f'`. Within the loop there are major subroutines such as `'imcgen2d'`, `'imcfield2d'`, `'imcvol2d'`, `'imcsurf2d'`, `'imcredist'`, `'update'`. `'update'` takes care of the F-P calculation. The other subroutines handle the MC part of the code as following:

- `'imcgen2d'`, generic preparation;
- `'imcfield2d'`, tracks previously stored field photons;
- `'imcvol2d'`, creates and tracks photons from internal emission, moslty synchrotron radiation in our cases;
- `'imcsurf2d'`, creates and tracks external photons at the surface zones;
- `'imcredist'`, re-distributes some of the newly created MC particles among processors so that the number of MC particles in each processor is almost the same.

The tracking of individual MC particles is done in `'imctrk2d.f'`. It is a recursive subroutine that calls itself when it is handling the splitting of MC particles. The actual IC scattering of MC particles is done in `'compb_2d.f'`. Files like `'fp_mpi.f'`, `'surf_mpi.f'` and `'vol_mpi.f'` each contains a set of subroutines that deal with tasks related to the parallelization, such as sending and receiving information among processors.

A typical run in Chap. 3 & 4 takes around 24 hours on eight 2.83 GHz CPU cores, using up to 16 GB of memory. For those runs we have not implemented the redistribution of the MC particle, so the code did not scale well with the number of CPUs, only gaining a factor of three in speed by going to 96 CPUs. The runs in Chap. 5 made use of the redistribution feature so that the speed increases almost linearly with the number of CPUs, at least when the number of CPUs is less than 100. In these cases a typical run takes 2 hours on 96 2.83 GHz CPU cores, with up to 384 GB of memory available.

A.1 Input files

There are 3 sets of input files, with `'input.dat'` being the most general one. Besides `'input.dat'`, each zone has its own input file, e.g. the input file for the 2nd zone in the z direction and 3rd zone in the r direction is `'input_02_03.dat'`. Zone specific parameters like magnetic field strength and electron densities are in these input files. The 3rd set of input files are the external radiation field. Their file names are specified in `'input.dat'`.

A.2 Output files

The names of the main output files are also specified in `'input.dat'`. The most important output files are the 'event files' that are lists of the escaped MC particles, with one file for each computing node. These lists contain the time the photons escaped in units of seconds, energy of the photons in the units of keV, the energy weight of the photons in units of ergs, the position of the photon escape (r, z) in units of cm, the direction of the photon escape (the cosine of the inclination angle $cos\theta$ and the azimuth angle ϕ. Remember the code is azimuthally symmetric, and this azimuth angle is the azimuth angle between the escape direction and the radial direction at the escape point). Another important set of output files are the electron distribution files. Currently these are recorded every time step for some of the zones. They are stored in the folder 'output'. The job log is kept in `'log.txt'`. Files such as `'p002_census.dat'` and `'p002_misc.dat'` are lists of photons in the volume, and current values of other variables in the processors (002 for processor number 2) that are stored so that it is possible to resume the unfinished jobs later.

A.3 Postprocessing program

The postprocessing programs are written in C. There are two postprocessing routines. One of them reduces the photon lists to tables with flux as a function of time (light curves), at multiple frequency intervals specified by the user; The other reduces the photons lists to a sequence of SED, i.e. flux vs. frequency. The relativistic beaming of the photons is performed first, then light curves and SED are produced by binning in time, frequency, and angle.

The beaming of the photons includes the following transformations

$$\nu = \delta\nu', \quad E_{\rm k} = \delta E'_{\rm k}, \quad cos\theta = \frac{\beta + cos\theta'}{1 + \beta cos\theta'}.$$

Because of the LTTE and the Lorentz transformation, photons escaped from different positions of the cylinder simultaneously in the blob frame will arrive at the observer at different time. Compared to the ones escaped from $z = 0, r = r_{\rm max}$, changeat angle $\phi = 0$, changethe time is delayed by

$$\Delta t = \frac{z cos\theta}{\Gamma c} + \frac{(r_{\rm max} - r cos\phi) sin\theta}{c} - \frac{\beta z}{\delta c}. \tag{A.1}$$

The first two terms are the results of the extra light travel time caused by the position and direction of the photon escape. The last term is a result of the Lorentz transformation of the escape time

$$t = \Gamma(t' - \frac{\beta z}{c}).$$

An extra $(1 - \beta cos\theta)$ comes from the fact the the blob is moving so these photons have moved closer to the observers when they escape.

Bibliography

Abbott, D. C., & Lucy, L. B. 1985, ApJ, 288, 679

Abdo, A. A. et al. 2010a, ApJ, 721, 1425

—. 2010b, ApJ, 716, 835

—. 2009, ApJ, 699, 817

Acciari, V. A. et al. 2011, ApJ, 738, 25

—. 2009, ApJ, 707, 612

Aharonian, F. et al. 2009, A&A, 502, 749

—. 2007, ApJ, 664, L71

Ambrosiano, J., Matthaeus, W. H., Goldstein, M. L., & Plante, D. 1988, J. Geophys. Res., 931, 14383

Antonucci, R. 1993, ARA&A, 31, 473

Arbeiter, C., Pohl, M., & Schlickeiser, R. 2005, ApJ, 627, 62

Baring, M. G., Ellison, D. C., & Jones, F. C. 1994, ApJS, 90, 547

Bednarek, W., & Protheroe, R. J. 1997, MNRAS, 292, 646

—. 1999, MNRAS, 310, 577

Begelman, M. C., & Sikora, M. 1987, ApJ, 322, 650

Bennert, N., Jungwiert, B., Komossa, S., Haas, M., & Chini, R. 2006, A&A, 459, 55

Bentz, M. C., Peterson, B. M., Netzer, H., Pogge, R. W., & Vestergaard, M. 2009, ApJ, 697, 160

Bentz, M. C., Peterson, B. M., Pogge, R. W., Vestergaard, M., & Onken, C. A. 2006, ApJ, 644, 133

Berezhko, E. G. 1981, Soviet Journal of Experimental and Theoretical Physics Letters, 33, 399

Blandford, R., & Eichler, D. 1987, Phys. Rep., 154, 1

Blandford, R. D., & McKee, C. F. 1982, ApJ, 255, 419

Blandford, R. D., & Payne, D. G. 1982, MNRAS, 199, 883

Blandford, R. D., & Znajek, R. L. 1977, MNRAS, 179, 433

Błażejowski, M. et al. 2005, ApJ, 630, 130

Błażejowski, M., Sikora, M., Moderski, R., & Madejski, G. M. 2000, ApJ, 545, 107

Blumenthal, G. R., & Mathews, W. G. 1975, ApJ, 198, 517

Borovsky, J. E., & Eilek, J. A. 1986, ApJ, 308, 929

Böttcher, M. 2007, Ap&SS, 309, 95

Böttcher, M., & Chiang, J. 2002, ApJ, 581, 127

Böttcher, M., & Dermer, C. D. 2010, ApJ, 711, 445

Böttcher, M., Jackson, D. R., & Liang, E. P. 2003, ApJ, 586, 389

Böttcher, M., & Liang, E. P. 2001, ApJ, 552, 248

Böttcher, M., Reimer, A., & Marscher, A. P. 2009, ApJ, 703, 1168

Brinkmann, W., Papadakis, I. E., den Herder, J. W. A., & Haberl, F. 2003, A&A, 402, 929

Brinkmann, W., Papadakis, I. E., Raeth, C., Mimica, P., & Haberl, F. 2005, A&A, 443, 397

Bujarrabal, V., Castro-Carrizo, A., Alcolea, J., & Sánchez Contreras, C. 2001, A&A, 377, 868

Canfield, E., Howard, W. M., & Liang, E. P. 1987, ApJ, 323, 565

Chang, J. S., & Cooper, G. 1970, Journal of Computational Physics, 6, 1

Chen, X., Fossati, G., Liang, E., & Böttcher, M. 2011, MNRAS, in press

Chiaberge, M., & Ghisellini, G. 1999, MNRAS, 306, 551

Cohen, M. H., Lister, M. L., Homan, D. C., Kadler, M., Kellermann, K. I., Kovalev, Y. Y., & Vermeulen, R. C. 2007, ApJ, 658, 232

Coppi, P., Blandford, R. D., & Rees, M. J. 1993, MNRAS, 262, 603

Coppi, P. S. 1992, MNRAS, 258, 657

Coppi, P. S., & Blandford, R. D. 1990, MNRAS, 245, 453

Costamante, L. et al. 2001, A&A, 371, 512

Crusius, A., & Schlickeiser, R. 1986, A&A, 164, L16

D'Ammando, F. et al. 2011, A&A, 529, A145

Dermer, C. D. 1998, ApJ, 501, L157

Dermer, C. D., Schlickeiser, R., & Mastichiadis, A. 1992, A&A, 256, L27

Donnarumma, I. et al. 2009, ApJ, 691, L13

Drury, L. O. 1983, Reports on Progress in Physics, 46, 973

Edelson, R. A., & Krolik, J. H. 1988, ApJ, 333, 646

Fabian, A. C., Celotti, A., Iwasawa, K., & Ghisellini, G. 2001a, MNRAS, 324, 628

Fabian, A. C., Celotti, A., Iwasawa, K., McMahon, R. G., Carilli, C. L., Brandt, W. N., Ghisellini, G., & Hook, I. M. 2001b, MNRAS, 323, 373

Fabian, A. C., Guilbert, P. W., Blandford, R. D., Phinney, E. S., & Cuellar, L. 1986, MNRAS, 221, 931

Falcone, A. D., Cui, W., & Finley, J. P. 2004, ApJ, 601, 165

Fanaroff, B. L., & Riley, J. M. 1974, MNRAS, 167, 31

Fermi, E. 1949, Physical Review, 75, 1169

Finke, J. D. 2007, PhD thesis, Ohio University

Finke, J. D., & Böttcher, M. 2007, ApJ, 667, 395

Fossati, G. et al. 2008, ApJ, 677, 906

—. 2000a, ApJ, 541, 153

—. 2000b, ApJ, 541, 166

Fossati, G., Celotti, A., Ghisellini, G., Maraschi, L., & Comastri, A. 1998, MNRAS, 299, 433

Gaisser, T. K. 1991, Cosmic Rays and Particle Physics (Cambridge: Cambridge University Press)

Garson, III, A. B., Baring, M. G., & Krawczynski, H. 2010, ApJ, 722, 358

Georganopoulos, M., Perlman, E. S., Kazanas, D., & Wingert, B. 2006, in Astronomical Society of the Pacific Conference Series, Vol. 350, Blazar Variability Workshop II: Entering the GLAST Era, ed. H. R. Miller, K. Marshall, J. R. Webb, & M. F. Aller, 178

Ghisellini, G., Celotti, A., Fossati, G., Maraschi, L., & Comastri, A. 1998, MNRAS, 301, 451

Ghisellini, G., Guilbert, P. W., & Svensson, R. 1988, ApJ, 334, L5

Ghisellini, G., & Madau, P. 1996, MNRAS, 280, 67

Ghisellini, G., & Tavecchio, F. 2009, MNRAS, 397, 985

Ghisellini, G., Tavecchio, F., Foschini, L., Ghirlanda, G., Maraschi, L., & Celotti, A. 2010, MNRAS, 402, 497

Giebels, B., Dubus, G., & Khélifi, B. 2007, A&A, 462, 29

Giommi, P., & Padovani, P. 1994, MNRAS, 268, L51

Graff, P. B., Georganopoulos, M., Perlman, E. S., & Kazanas, D. 2008, ApJ, 689, 68

Guetta, D., Ghisellini, G., Lazzati, D., & Celotti, A. 2004, A&A, 421, 877

Jorstad, S. G. et al. 2005, AJ, 130, 1418

Kaspi, S., Brandt, W. N., Maoz, D., Netzer, H., Schneider, D. P., & Shemmer, O. 2007, ApJ, 659, 997

Kataoka, J. 2000, PhD thesis, Univ. of Tokyo

Kataoka, J. et al. 2008, ApJ, 672, 787

Kataoka, J., Takahashi, T., Makino, F., Inoue, S., Madejski, G. M., Tashiro, M., Urry, C. M., & Kubo, H. 2000, ApJ, 528, 243

Katarzyński, K., Ghisellini, G., Mastichiadis, A., Tavecchio, F., & Maraschi, L. 2006, A&A, 453, 47

Katarzyński, K., Ghisellini, G., Tavecchio, F., Maraschi, L., Fossati, G., & Mastichiadis, A. 2005, A&A, 433, 479

Katarzyński, K., Lenain, J., Zech, A., Boisson, C., & Sol, H. 2008, MNRAS, 390, 371

Kellermann, K. I. et al. 2004, ApJ, 609, 539

Kellermann, K. I., & Pauliny-Toth, I. I. K. 1981, ARA&A, 19, 373

Kellermann, K. I., Vermeulen, R. C., Zensus, J. A., & Cohen, M. H. 1998, AJ, 115, 1295

Kirk, J. G., Guthmann, A. W., Gallant, Y. A., & Achterberg, A. 2000, ApJ, 542, 235

Kirk, J. G., Melrose, D. B., Priest, E. R., Benz, A. O., & Courvoisier, T. J.-L., eds. 1994, Plasma Astrophysics

Kirk, J. G., Rieger, F. M., & Mastichiadis, A. 1998, A&A, 333, 452

Krawczynski, H., Coppi, P. S., & Aharonian, F. 2002, MNRAS, 336, 721

Krawczynski, H. et al. 2004, ApJ, 601, 151

—. 2001, ApJ, 559, 187

Krolik, J. H., & Begelman, M. C. 1988, ApJ, 329, 702

Levinson, A. 2006, International Journal of Modern Physics A, 21, 6015

Li, H., & Kusunose, M. 2000, ApJ, 536, 729

Lichti, G. G. et al. 2008, A&A, 486, 721

Lind, K. R., & Blandford, R. D. 1985, ApJ, 295, 358

Mücke, A., & Protheroe, R. J. 2001, Astroparticle Physics, 15, 121

Makino, F. 1999, in Astronomical Society of the Pacific Conference Series, Vol. 159, BL Lac Phenomenon, ed. L. O. Takalo & A. Sillanpää, 190

Malmrose, M. P., Marscher, A. P., Jorstad, S. G., Nikutta, R., & Elitzur, M. 2011, ApJ, 732, 116

Mannheim, K. 1998, Science, 279, 684

Mannheim, K., & Biermann, P. L. 1992, A&A, 253, L21

Maraschi, L. et al. 1999, ApJ, 526, L81

Maraschi, L., Ghisellini, G., & Celotti, A. 1992, ApJ, 397, L5

Marscher, A. P. et al. 2010, ApJ, 710, L126

Marscher, A. P., & Travis, J. P. 1996, A&AS, 120, 537

Mastichiadis, A., & Kirk, J. G. 1997, A&A, 320, 19

McHardy, I., Lawson, A., Newsam, A., Marscher, A. P., Sokolov, A. S., Urry, C. M., & Wehrle, A. E. 2007, MNRAS, 375, 1521

Meyer, E. T., Fossati, G., Georganopoulos, M., & Lister, M. L. 2011, ApJ, 740, 98

Mirabel, I. F., & Rodríguez, L. F. 1999, ARA&A, 37, 409

Moraitis, K., & Mastichiadis, A. 2011, A&A, 525, A40+

Nayakshin, S., & Melia, F. 1998, ApJS, 114, 269

Padovani, P., & Giommi, P. 1995, ApJ, 444, 567

Parker, E. N. 1958, Physical Review, 109, 1328

Pier, E. A., & Krolik, J. H. 1992a, ApJ, 401, 99

—. 1992b, ApJ, 399, L23

Poutanen, J., & Stern, B. 2010, ApJ, 717, L118

Press, W., Teukolsky, S., Vetterling, W., & Flannery, B. 1992, Numerical Recipes, the art of scientific computing second edition (Cambridge University Press)

Protheroe, R. J. 1996, in Towards the Millennium in Astrophysics: Problems and Prospects, Erice 1996, eds. M.M. Shapiro and J.P. Wefel (World Scientific: Singapore)

Protheroe, R. J. 2002, PASA, 19, 486

Pucella, G. et al. 2008, A&A, 491, L21

Punch, M. et al. 1992, Nature, 358, 477

Rachen, J. P. 2000, in Proc. of GeV-TeV Gamma Ray Astrophysics Workshop: Towards a Major Atmospheric Cherenkov Detector VI, Snowbird, eds. B.L. Dingus, M.H. Salamon, D.B. Kieda, AIP Conf. Proc. 515 (New York: AIP)., 41

Ravasio, M. et al. 2002, A&A, 383, 763

Ravasio, M., Tagliaferri, G., Ghisellini, G., & Tavecchio, F. 2004, A&A, 424, 841

Rebillot, P. F. et al. 2006, ApJ, 641, 740

Reipurth, B., & Bally, J. 2001, ARA&A, 39, 403

Rieger, F. M., & Duffy, P. 2004, ApJ, 617, 155

—. 2006, ApJ, 652, 1044

Robinson, A. et al. 1994, A&A, 291, 351

Rybicki, G. B., & Lightman, A. P. 1979, Radiative Processes in Astrophysics, John Wiley & Sons ((New York): John Wiley & Sons)

Sambruna, R. M. et al. 2000, ApJ, 538, 127

Sato, R., Kataoka, J., Takahashi, T., Madejski, G. M., Rügamer, S., & Wagner, S. J. 2008, ApJ, 680, L9

Savolainen, T., Homan, D. C., Hovatta, T., Kadler, M., Kovalev, Y. Y., Lister, M. L., Ros, E., & Zensus, J. A. 2010, A&A, 512, A24

Sembay, S., Edelson, R., Markowitz, A., Griffiths, R. G., & Turner, M. J. L. 2002, ApJ, 574, 634

Shakura, N. I., & Sunyaev, R. A. 1973, A&A, 24, 337

Sikora, M., Begelman, M. C., & Rees, M. J. 1994, ApJ, 421, 153

Sikora, M., Błażejowski, M., Begelman, M. C., & Moderski, R. 2001, ApJ, 554, 1

Sikora, M., & Madejski, G. 2001, in American Institute of Physics Conference Series, Vol. 558, American Institute of Physics Conference Series, ed. F. A. Aharonian & H. J. Völk, 275–288, booktitle was: American Institute of Physics Conference Series

Sikora, M., Stawarz, Ł., Moderski, R., Nalewajko, K., & Madejski, G. M. 2009, ApJ, 704, 38

Sokolov, A., & Marscher, A. P. 2005, ApJ, 629, 52

Sokolov, A., Marscher, A. P., & McHardy, I. M. 2004, ApJ, 613, 725

Spada, M., Ghisellini, G., Lazzati, D., & Celotti, A. 2001, MNRAS, 325, 1559

Spitkovsky, A. 2008, ApJ, 682, L5

Stawarz, Ł., & Ostrowski, M. 2002, ApJ, 578, 763

Stern, B. E., Begelman, M. C., Sikora, M., & Svensson, R. 1995, MNRAS, 272, 291

Tagliaferri, G. et al. 2008, ApJ, 679, 1029

Takahashi, T. et al. 2000, ApJ, 542, L105

—. 1996, ApJ, 470, L89

Tanihata, C., Kataoka, J., Takahashi, T., & Madejski, G. M. 2004, ApJ, 601, 759

Tavecchio, F., & Ghisellini, G. 2008, MNRAS, 386, 945

Tavecchio, F., Maraschi, L., & Ghisellini, G. 1998, ApJ, 509, 608

Tavecchio, F. et al. 2001, ApJ, 554, 725

Thompson, D. J., Djorgovski, S., & de Carvalho, R. 1990, PASP, 102, 1235

Tramacere, A., Giommi, P., Perri, M., Verrecchia, F., & Tosti, G. 2009, A&A, 501, 879

Tramacere, A., Massaro, E., & Taylor, A. M. 2011, ApJ, 739, 66

Tramacere, A., Massaro, F., & Cavaliere, A. 2007, A&A, 466, 521

Ulrich, M.-H., Maraschi, L., & Urry, C. M. 1997, ARA&A, 35, 445

Urry, C. M., & Padovani, P. 1995, PASP, 107, 803

Ushio, M. et al. 2010, ApJ, 724, 1509

—. 2009, ApJ, 699, 1964

Vainio, R., & Schlickeiser, R. 1998, A&A, 331, 793

Virtanen, J. J. P., & Vainio, R. 2005, A&A, 439, 461

Wardle, J. F. C., Homan, D. C., Cheung, C. C., & Roberts, D. H. 2005, in Astronomical Society of the Pacific Conference Series, Vol. 340, Future Directions in High Resolution Astronomy, ed. J. Romney & M. Reid, 67